Turbulence and pattern formation in continuum models for active matter

Martin James

Turbulence and pattern formation in continuum models for active matter

Dissertation

for the award of the degree
“Doctor of Philosophy” Ph.D.
Division of Mathematics and Natural Sciences
of the Georg-August-Universität Göttingen

within the doctoral degree program

Physics of Biological and Complex Systems
of the Göttingen Graduate Center for Neurosciences, Biophysics and Molecular Biosciences (GGNB)
of the Georg-August University School of Sciences (GAUSS)

submitted by

Martin James
from Nilambur, India
Göttingen, 2019

THESIS COMMITTEE:

Dr. Michael Wilczek

MPRG Turbulence, Complex Flows and Active Matter
Max Planck Institute for Dynamics and Self-Organization

Prof. Dr. Marcus Müller

Institute for Theoretical Physics
University of Göttingen

Prof. Dr. Stephan Herminghaus

Department for Dynamics of Complex Fluids
Max Planck Institute for Dynamics and Self-Organization

MEMBERS OF THE EXAMINATION BOARD:

Dr. Michael Wilczek (Reviewer)

MPRG Turbulence, Complex Flows and Active Matter
Max Planck Institute for Dynamics and Self-Organization

Prof. Dr. Marcus Müller (Second reviewer)

Institute for Theoretical Physics
University of Göttingen

FURTHER MEMBERS OF THE EXAMINATION BOARD:

Prof. Dr. Stephan Herminghaus

Department for Dynamics of Complex Fluids
Max Planck Institute for Dynamics and Self-Organization

Prof. Dr. Stefan Klumpp

Institute for Dynamics of Complex Systems
University of Göttingen

Prof. Dr. Annette Zippelius

Institute for Theoretical Physics
University of Göttingen

Dr. David Zwicker

MPRG Theory of Biological Fluids
Max Planck Institute for Dynamics and Self-Organization

Date of oral examination: January 17, 2020

Preface

When I started working on my thesis with Michael, it was planned as a comprehensive statistical characterization of the turbulent phase in active matter, in two as well as three dimensions. But as is the case with most dissertations, more exciting ideas came in the way. Michael accidentally came across an interesting vortex crystal solution to the active matter model that we were looking at. It was about a year later that we started looking closely at these crystal phases and it proved to be a rich arena with close connections to solid-state physics. Now, as it stands, the present work is divided roughly into two halves; one concerned with the active turbulence phase and the other with active vortex crystals. Put together, this work addresses two of the arguably most important phases, after the well studied flocking phase, in active matter.

Active matter is an evolving field of physics. Thus it comes with a lot of exciting opportunities; several new phenomena to study, understand and predict. But there are also vices associated with a vastly expanding field. Fragmentation and conflicting approaches to describe the same phenomenon as well as disconnect between theory and experiments among others. While the present work is not, and cannot be, immune to these problems, I have tried to explain and address these problems whenever possible. Perhaps the biggest shortcoming of this work, like in many theoretical works in active matter, is its lack of direct connection to experiments. But I have discussed about possible experimental proposals which can prove or disprove the results presented here. Active vortex crystals, in particular, is a fabulous playground for a rich range of experiments whose results will be remarkable considering how exciting the field of two-dimensional crystals is.

This dissertation is styled in the form of a cumulative thesis; with two published manuscripts and one manuscript prepared for publication forming the bulk of the results. The first chapter provides a comprehensive introduction to all the results and also introduces our primary model. The dissertation ends with a discussion, putting the results from the manuscripts in a wider context.

I would like to express my gratitude to the many people who have made this dissertation possible. I am deeply indebted to Michael for his excellent guidance throughout this project. It was a great pleasure to work with him and his advice, and discus-

sions with him, have contributed significantly to this work. Comments and suggestions from the other members of my Thesis Advisory Committee, Stephan Herminghaus and Marcus Müller, have helped in the timely progress of this work and are gratefully acknowledged. I would also like to thank Stefan Klumpp, Annette Zippelius and David Zwicker for agreeing to be part of my doctoral examination board.

I am very grateful to the collaborators involved with this study. The work on closure models for active turbulence was done in collaboration with Wouter Bos and the vortex crystal project involves collaboration with Jörn Dunkel. I have also had the pleasure of working with Dominik during his Bachelors thesis, the results of which form part of the third manuscript. I would like to thank Samriddhi for having introduced me to the field of turbulence.

Many scientific members at the Institute have contributed to the improvement of this work and have helped make my stay in Göttingen memorable. I especially thank the past and current members of the Wilczek group as well as the LFPB department. I am very grateful to Chichi, Colin, Gerrit, Tobias and Venecia for proofreading this dissertation. I thank Dario for the wonderful discussions during his many visits to Göttingen. I express my sincere gratitude to the administrative staff at the Institute for their invaluable help. I thank Angela for going over and beyond her job requirements to help me during the initial days of my stay in Göttingen, and also Barbara for her generous help with the administrative matters. The help from the IT staff at the Institute is gratefully acknowledged.

I thank Antje, Frauke and Judith from IMPRS-PBCS, and the staff at GGNB and the international office of the University of Göttingen for their help over the years. Financial (through IMPRS-PBCS fellowship), infrastructural and computational (MPCDF and MPI DS computational facilities) support from the Max Planck Society is gratefully acknowledged.

I thank my family for their constant support throughout the duration of this work.

Göttingen, November 21, 2019 Martin James

Contents

Abstract

Living and nonliving active matter, ranging from flocks of birds to active colloids, exhibit a fascinating range of physical phenomena such as order-disorder transitions and density waves in flocking phases, chaotic states and pattern formation. While the properties of flocking phases have received considerable attention, other active matter phases are relatively less explored. In this dissertation, we theoretically and computationally investigate turbulence and crystalline patterns, as well as transitions between these phases, in two-dimensional active matter.

In the first half, we study turbulence in active fluids. Important statistical quantities such as probability density functions of velocity and vorticity as well as velocity correlations and energy spectra are analyzed. We show that active turbulence, in contrast to hydrodynamic turbulence, is characterized by a strong length-scale selection. We develop a statistical closure theory for velocity correlations based on the eddy-damped quasi-normal Markovian approximation from hydrodynamic turbulence theory. This theory captures the statistical features of active turbulence across a range of activity values, suggesting the applicability of classical hydrodynamic theory in investigating the properties of active fluids.

In the second half of this dissertation, we investigate the properties of a spontaneously emerging crystalline phase. We show that this nonequilibrium crystal preserves some of the properties of their equilibrium counterparts. The melting of such active vortex crystals may proceed with a hysteretic transition region, or through an intermediate hexatic phase, depending on the values of the control parameters. Interestingly, we observe that the duration of crystallization increases with the domain size. As we approach the thermodynamic limit, superstructures of vortex crystal domains emerge leading to a supertransient phase. These superstructures form domains of vortex crystals of opposite polarity spins, demarcated by a turbulent active fluid. We also discuss generalizations to the continuum equations used in this work. Advected Swift-Hohenberg equations form a wider class of models that can qualitatively describe active fluids.

Taken together, the results in this dissertations present an analysis of crystallization and turbulent dynamics in active matter within one uniform framework.

1 Introduction

Active matter refers to nonequilibrium collective systems where the constituent particles continuously convert internal (or external) energy into mechanical energy [1–4]. There is an abundance of such phenomena in nature ranging from flocks of birds, schools of fish and herds of animals to swarms of microorganisms and even intra-cellular structures (Fig. 1.1 (a)-(d)). These phenomena cover length scales spanning a few micrometers to several kilometers. Apart from such living matter, there are also carefully constructed nonliving active systems (Fig. 1.1 (e), (f)): for example, rods propelled on a vibrating membrane, though forced externally, display dynamics qualitatively similar to the living systems [5]. Another example is an active system of self-propelled colloids of Janus particles (Fig. 1.1 (f)). These active matter systems form the physical basis for this study. Before stating the questions addressed in this dissertation, it is instructive to explain why it is worthwhile to investigate these systems and more importantly, what role can physicists play in unraveling the questions related to them.

Let us start by looking at the important features exhibited by biological active matter. Perhaps the most startling observation is the most common one too: flocking. There exist several examples of flocking in nature: flocks of birds to herds of animals showing long-range global order. These are surprising since such a global order is prohibited in two-dimensional equilibrium systems with a finite range of interactions and continuous symmetry (continuous orientational symmetry of the active agents) [6–8]. To put it differently, if we prevent all the animals in a herd from moving and force them to order only by "looking" at the orientation of their neighbors, it would be impossible for them to do so [9]. This is essentially the two-dimensional XY model of spins on a lattice, which does not show long-range order. But the addition of a simple nonequilibrium feature (activity) leads to the emergence of global order. Arguably, the evidence that a nonequilibrium XY model can exhibit a global order at finite noise constitutes the starting point of active matter research [10]. A considerable amount of research on active matter has since been devoted to explain the different properties of this flocking phase [3, 11].

Apart from flocking states, there are several other phases of active matter (Fig. 1.1 (b)-(f)). For example, spermatozoa suspensions form regular hexagonal lattices of active

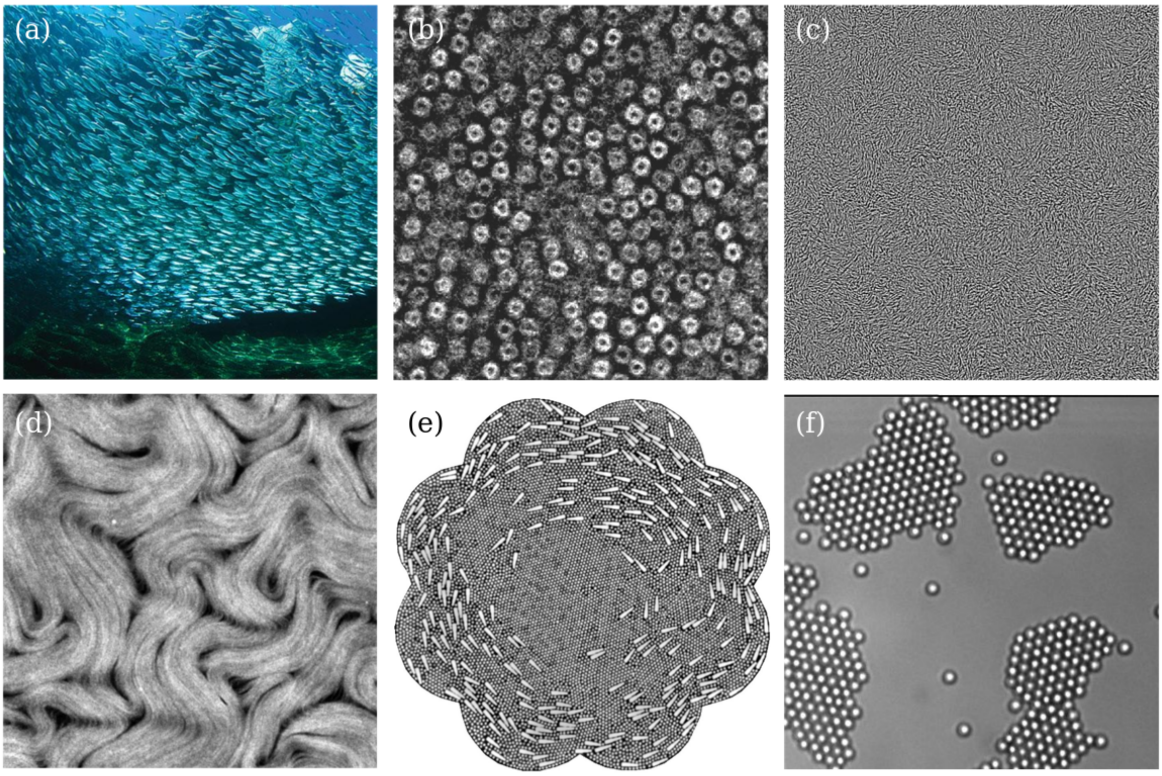

Figure 1.1: Some examples of living and non-living active matter systems. (a) A large sardine school exhibiting polar order. (b) Self-organized vortex array formed by spermatozoa of sea urchins. An example of pattern formation in active fluids. (c) Turbulent dynamics in active fluids as exhibited by a quasi two-dimensional dense suspension of *B. Subtilis*. (d) Active turbulence in a nematic system formed by a microtubule-kinesin mixture. (e) Ordering in active granular matter: asymmetric copper rods in a background of aluminum beads. (f) Another example of inanimate active matter: light activated active colloids. Panel (a) is from *Jon Bertsch photography (jonbertsch.com)* and the other figures are adapted from references [5, 12–15]. All figures are reproduced with permission.

vortices [12] whereas microtubule systems have been shown to form irregular lattices [16]. There are also many other examples of pattern formation and crystal-like phases in a variety of active matter systems [15, 17]. These raise many interesting questions: How general is the pattern formation phenomenon? How can the length scale and the type of pattern be explained? Can the methods and techniques developed in classical pattern formation phenomena, like convection, be used to explain pattern formation in active matter? How does the transition to the crystalline phases contrast with the transition to the flocking phases? Does it share any properties with equilibrium phase transitions?

Another phase with intriguing features is what is referred to as active turbulence or turbulent active fluid (Fig. 1.1 (c), (d)). Active turbulence has been observed in dense bacterial suspensions as well as in several other microswimmer systems [13, 18–20]. Such turbulent flow in active fluids is characterized by the spontaneous formation of vortices and jets and irregular, "chaotic" dynamics. These phenomena are termed active turbulence by virtue of their similarity to hydrodynamic turbulence. But active turbulence differs from hydrodynamic turbulence in several crucial ways. The instability and transition to turbulence in Newtonian fluids occur at a high value of the non-dimensional Reynolds number [13]. The Reynolds number characterizes the relative strength between the inertial forces and the viscous forces. For a pipe flow, for example, the transition to turbulence occurs at a Reynolds number of the order of 10^3 [21]. In contrast, the Reynolds number associated with the swimming microorganisms is usually less than 10^{-2} [22]. Also, in this low Reynolds number turbulence, unlike hydrodynamic turbulence, there is a clear length-scale selection characterized by uniformly sized vortices.

A comprehensive investigation of active matter systems would thus involve combining techniques from statistical mechanics, pattern formation as well as hydrodynamics. This dissertation presents such an investigation of these intriguing phases in active matter systems. In particular, we numerically investigate the pattern formation and crystallization as well as turbulence-like dynamics. Our objective is to show, given the insensitivity of these observations to many of the microscopic details of the physical system, whether these properties can be understood and analyzed through universal, phenomenological considerations. Such studies have been successfully undertaken for the flocking phase of active matter [11, 23]. What we present here is a natural extension of these results, applied to more diverse phenomena.

We can now write down the defining properties of active matter: (a) The basic dynamics in these systems occur at the scale of the constituent particles. To put it differently, there is constant energy injection at the length scale of the active agents, driving the system out of equilibrium. (b) The individual particles may interact with the neighbors within a finite distance. This interaction may be of hydrodynamic, steric, or physiological nature. (c) There is inherent noise in the system which prevents perfect alignment with neighbors. Put together, the three properties described above would not only provide a starting point for a theoretical understanding of active matter systems but also contrast its properties with that of equilibrium systems. It is, of course, property (a) which distinguishes active matter from its equilibrium counterparts.

Active system	**Definition**	**Example**
Polar	Active agents have a preferred orientation and direction of motion	Bird flocks
Nematic	Active agents have no preferred orientation or direction of motion	Microtubule-kinesin mixture
Dry active matter	Interactions with the solvent flow neglected, no momentum conservation in the equations of motion	Toner-Tu model [23]
Wet active matter	Takes into account hydrodynamic interactions, equations of motion conserve momentum	Simha-Ramaswami equations of motion [24]

Table 1.1: Different types of active matter systems and models. See ref. [17] for more details.

Before we delve into more details, let us classify the different types of active matter systems and models [17]. A continuum theory can capture the large-scale features of a system at a coarse-grained level and such a physical system may be called an active fluid. We note that there are conflicting definitions in literature for the term “active fluid” [3, 13, 25], so we use the following convention. The term active fluid does not refer to another class of system within active matter, but merely signifies the scale separation between the scales of interest and length scale associated with the individual constituents. In terms of the type of interaction between these constituent agents, active fluids are classified into polar and nematic. Polar active fluids are the ones where the constituents are asymmetric with a preferential alignment along one direction. Examples include bacterial suspensions and asymmetric vibrated granular media. Nematic active fluids, on the other hand, have head-tail symmetry and have no preferred orientation. Microtubule-kinesin mixture is an example of such systems. Since such systems have orientational properties similar to that of liquid crystals, they are also called active liquid crystals. There are also polar active fluids, i.e., with head-tail asymmetry, but with nematic interactions and vice versa. Also, depending on the model used, a system can be categorized as wet or dry. A wet model preserves momentum conservation by taking into account the hydrodynamic interactions with the solvent. A dry model, on the other hand, does not explicitly take this hydrodynamic coupling into account. Our focus in this dissertation is on the dynamics of polar active fluids with polar interaction based on a dry model.

The rest of this introduction is organized as follows. We start with a brief historical overview of active matter research and review the current research questions in the field.

Since the phenomenon of active turbulence and its connection to hydrodynamic turbulence occupies a central part of this dissertation, we will then provide a summary of the important statistical results from hydrodynamic turbulence relevant to our results. This is followed by a discussion about crystals in two dimensions since we focus on vortex crystals in active fluids in the latter part of the dissertation. We then introduce the continuum model for active matter, which is adapted from a theory of active turbulence [13, 26]. We end the introduction with an outline of the rest of the dissertation.

1.1 Active matter

Active matter is a relatively novel branch of physics: the origin of the field, as the term 'active matter' is understood today, can be traced back to the work by Tamaz Vicsek in 1995 on the statistical mechanics of flocking [10]. Today the research on active matter attempts to explain the collective motion of self-propelled agents over a wide range of length scales; from microswimmers to animal flocks. The actual mechanism of self-propulsion varies significantly across this spectrum. We start this overview with a brief description of a few types of microswimmers and their propulsion mechanisms. The research into the dynamics of microswimmers has a long and rich history, which we summarize. We then trace the historical development of the field of active matter starting with Vicsek's seminal work and the associated theoretical and experimental developments in the study of flocking phases. We conclude our overview describing the recent experimental observations of several novel phases ranging from low Reynolds number turbulence to crystalline phases in active matter systems.

1.1.1 Microswimmers

Swimming of microswimmers is a fascinating topic, not least because of the low Reynolds number, viscosity-dominated regime they inhabit [27]. While the length scales we investigate in this dissertation allow us to coarse-grain the dynamics and thus disregard the locomotion of an individual microswimmer, it is still instructive to discuss the topic as a starting point. Collective dynamics in bacterial suspensions, as well as spermatozoa and microtubule systems, form the main motivation for this study. Thus we start by describing their structures and propulsion mechanisms. (See ref. [28] for a review.)

In bacteria such as *E. Coli* and *B. Subtilis*, the primary method of propulsion is by using a flagellum - a helical organelle attached to the cell wall. The organism moves by rotating the flagellum (usually in a bundle of multiple flagella) by using a motor protein embedded in its cell wall, thus creating a pushing (pusher-type such as *E. Coli*) or pulling (example *C. reinhardtii*) force [29]. In a free solution, such bacteria follow what is referred to as a run-and-tumble motion [30]. The cell, aided by the flagella, moves (run) along its long axis until it abruptly stops and reorients in a random direction (tumble). Tuning the duration of the run and tumble phases allows the organism to follow environmental cues such as chemical gradients. As opposed to the free motion in a fluid, the swarming motility of bacteria on a surface involves more complicated dynamics [31]. It is in this swarming state, at very high concentrations, that we observe the two-dimensional active turbulence phase. Spermatozoa suspension is another microswimmer system that shows turbulent dynamics [20]. Sperm cells have a spherical head attached to a eukaryotic flagellum. As opposed to the bacterial flagella which rotate, the eukaryotic flagellum creates helical waves by a bending motion which provides the necessary propulsion [29]. The mechanism of this bending may vary depending on the type of sperm cell and the environment.

One important active matter system which has been extensively studied in the past few years is the microtubule-motor protein mixture which acts as a model active nematic fluid [19]. Microtubules, a polymer of globular proteins, are tubular filaments which form part of the cytoskeleton. When mixed with motor proteins such as kinesin, microtubules result in a highly dynamic active gel [32]. The motor protein aligns the filaments together and drives the dynamics based on adenosine triphosphate (ATP) concentration. While the filaments themselves are neither motile nor microswimmers, the resulting mixture follows the properties of an active matter system. This system exhibits a nematic active turbulence phase which has been investigated experimentally and theoretically in the recent past [19], as we review in the sections below.

There also exists a wide class of synthetic microswimmers. One common example, in the context of collective motion, is an active colloid system. These are usually prepared with Janus colloids which can show propulsion in a preferred direction due to their asymmetry. They are driven by, e.g., chemical gradients [28] or phototaxis [15]. There are also active systems of colloidal rollers driven by an electric field [33]. Apart from active colloids, some examples of synthetic microswimmers include active bubble jets [28] or ferromagnetic helices driven by magnetic fields [34].

In the case of the dynamics of microswimmers, the incompressible Navier-Stokes equation describing the fluid flow (discussed in detail in the next section) can be considerably simplified. The length scales of interest allows us to neglect the inertial effects and if the viscous time scales are less than the characteristic time scale of the motion, we are left with a linear Stokes flow approximation for the fluid

$$\nabla p - \eta \nabla^2 \boldsymbol{u} = \boldsymbol{f}.$$

Here $\boldsymbol{u}$, p and η are the fluid velocity, pressure and viscosity, respectively, and $\boldsymbol{f}$ is the force exerted by the microswimmer. By virtue of the linearity of the above equation, it can be solved analytically by using a Green's function - the Oseen tensor. This can be obtained from the solution to a point-force field $\boldsymbol{f}(\boldsymbol{r}) = \delta(\boldsymbol{r})\hat{\boldsymbol{e}}$, which in three dimensions is given by

$$\boldsymbol{u}(\boldsymbol{r}) = \frac{1}{8\pi\eta r}\left[\hat{\boldsymbol{e}} + \frac{(\boldsymbol{r}\cdot\hat{\boldsymbol{e}})\boldsymbol{r}}{r^2}\right].$$

Perhaps the simplest approximation for a microswimmer, based on the discussion above, is a force dipole, which is a good model for certain organisms [35]. Under this assumption, the velocity field decays quadratically with distance. More sophisticated point-force models can be built to take into account anisotropy, flagellar motion and other effects [28]. Other common theoretical models for microswimmers include squirmers which are hard spheres with a prescribed tangential surface velocity [36].

Extending the above approach to multiple swimmers will allow us to model collective motion emerging from hydrodynamic interactions. But as we have already noted, irrespective of whether the interaction is hydrodynamic, steric or physiological, and irrespective of the inhabiting environment, there are several collective states which recur across a wide spectrum of active agents. This points to simpler and general approximations for such interactions being able to describe collective phenomena. In the next section, we discuss such a statistical mechanical theory of active matter and related developments.

1.1.2 Flocking and statistical mechanics of active matter

As we discussed at the beginning of this chapter, one of the significant results in active matter is the ferromagnetic order characterized by the long-range correlation of the orientation of the spins observed in the Vicsek model [10]. To appreciate this, let us start with a brief reminder about an important result in statistical mechanics, the Mermin-Wagner-Hohenberg theorem. As originally proven by Mermin and Wagner, it states that in dimensions $d \leq 2$, in the XY model, the continuous orientational symmetry cannot be spontaneously broken [6–8]. This means that in the two-dimensional XY model, at any non-zero temperature, the thermal fluctuations destroy the long-range order.

The Vicsek model is a dynamic XY model that shares some properties with the flocking phases of active matter. The Vicsek model explores this flocking phase by using a simple nonequilibrium extension of the XY model [10]. Compared to the fixed spins in the XY model, the spins in the Vicsek model move in the direction they point to. A noise parameter, which acts like a temperature, randomly changes the direction of the particles while a short-range interaction parameter aligns them. Thus $\boldsymbol{x}_i(t+1) = \boldsymbol{x}_i(t) + v\hat{\boldsymbol{e}}_{\theta_i}$ where $\boldsymbol{x}_i$ is the position of the particles, v is the self-propulsion speed and θ_i is the orientation. The time evolution of the orientation angle θ of particle i is given by

$$\theta_i(t+1) = \langle\theta_i(t)\rangle_R + \eta_i(t),$$

where the average is over all particles in radius R and the random vector $\eta_i(t)$ is the noise

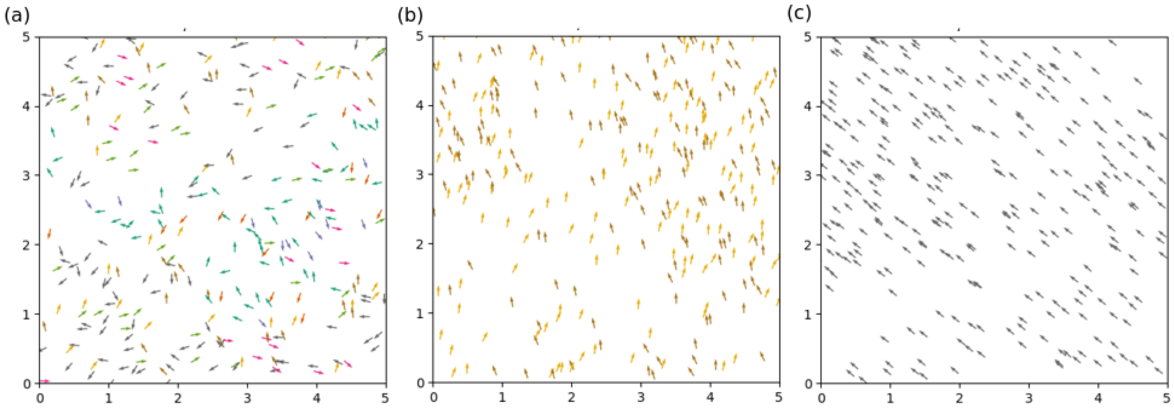

Figure 1.2: Transition to a flocking phase in the Vicsek model: Snapshots of the statistically steady states in the Vicsek model as the magnitude of the noise parameter is decreased. (a) For a large magnitude for the noise parameter, the system remains in an isotropic phase. The different colors denote the different orientations of the self-propelled particles. (b), (c) As the magnitude of the noise is reduced, we observe a transition to a flocking phase. (Here the particle density $\rho = 12$, the self-propulsion speed $v = 0.03$ and the magnitudes of the noise parameter η are $5, 1$ and 0.1 for (a), (b) and (c) respectively.)

parameter drawn from a uniform distribution. As the magnitude of the noise parameter is reduced, Vicsek et al. [10] noted that the system undergoes a transition from an isotropic phase to an ordered phase (Fig. 1.2). Although this is a nonequilibrium system, one can still classify the nature of this transition. In the original work, the transition was classified as continuous. However, later investigations have shown that the phase transition in the Vicsek model is discontinuous [37, 38]. Another important feature of the Vicsek system is that it exhibits the so-called giant number fluctuations [39]. In an equilibrium system the fluctuations in the number of particles, in the grand canonical ensemble for instance, usually grow as $\sqrt{\langle N^2\rangle - \langle N\rangle^2} \sim \sqrt{N}$. However, the Vicsek system shows anomalous scaling of the fluctuations where it grows faster than $\sqrt{N}$, a property observed in other active matter systems too [17, 38].

Several generalizations to the Vicsek model have been explored. For instance, the Vicsek model can be modified to account for nematic interactions [40]. Surprisingly the properties of the nematic system contrast with that of the polar-ordered Vicsek model since it does not form a phase with long-range order [38, 40]. Another example is a continuous version of the Vicsek model which takes the form $\dot{\boldsymbol{x}}_i = \hat{\boldsymbol{e}}_{\theta_i}$ [41]. The orientations evolve according to

$$\frac{\mathrm{d}\theta_i}{\mathrm{d}t} = \sum_j \sin\left[m\left(\theta_i - \theta_j\right)\right] + \omega_i\left(t\right).$$

The summation is over all neighbors within a fixed distance. The noise ω_i can be white noise similar to the original Vicsek model, or a stochastic process with memory such as an Ornstein-Uhlenbeck process [41]. The parameter m can take values to enforce polar or nematic ordering. More realistic models can be constructed by taking into account the effect of the solvent flow and hydrodynamic interactions [42–44].

So why does the Vicsek model show long-range order? The starting point for such a theoretical analysis of polar ordering in the dry active matter is the Toner-Tu equations of motion [9, 11, 23, 45]. It is a continuum model that describes the coarse-grained velocity field and the density of the active spins. These equations were originally derived phenomenologically based on symmetry considerations. This implies writing down all the terms in the evolution equation for the velocity field permitted by the symmetries and the conservation laws, keeping only the lowest-order terms in the gradients and the time derivatives. So what are the symmetries of the system? The active spin system is rotationally and translationally invariant, but it is important to note that it lacks Galilean invariance. This is because the spins move in a restive medium with a self-propulsion velocity with respect to a unique frame of reference. So shifting to another co-moving frame of reference need not render the equations unchanged. With these details in mind, the Toner-Tu model for polar dry active matter is given by [11, 23, 45]

$$\begin{aligned}&\frac{\partial \boldsymbol{u}}{\partial t} + \lambda_1(\boldsymbol{u}\cdot\nabla)\boldsymbol{u} + \lambda_2(\nabla\cdot\boldsymbol{u})\boldsymbol{u} + \lambda_3\nabla(|\boldsymbol{u}|)^2 = \\ &U\boldsymbol{u} - \nabla P + D_B\nabla(\nabla\cdot\boldsymbol{u}) + D_T\nabla^2\boldsymbol{u} + D_2(\boldsymbol{u}\cdot\nabla)^2\boldsymbol{u} + \boldsymbol{f}.\end{aligned} \tag{1.1}$$

Here U is the local alignment function and $\boldsymbol{f}$ is a stochastic noise. All the parameters are functions of ρ and $|\boldsymbol{u}|$. The above equation can be closed with a state function for the pressure P and a continuity equation for the density. The system is made active by an appropriate choice for U, for instance $U = \alpha - \beta|\boldsymbol{u}|^2$. The dynamic effect of this choice is to make the absolute value of the velocity, $|\boldsymbol{u}|$, evolve towards the stationary value $\sqrt{\alpha/\beta}$. To make this clear, note that the term $U\boldsymbol{u}$ can be written as the derivative of a functional $U\boldsymbol{u} = -\delta V[\boldsymbol{u}]/\delta\boldsymbol{u}$, where

$$V[\boldsymbol{u}] = \int_\Omega \left[-\frac{1}{2}\alpha|\boldsymbol{u}|^2 + \frac{1}{4}\beta|\boldsymbol{u}|^4\right]\mathrm{d}\boldsymbol{r} = \int_\Omega \left[\left(\frac{\sqrt{\beta}}{2}|\boldsymbol{u}|^2 - \frac{\alpha}{2\sqrt{\beta}}\right)^2 + \frac{\alpha^2}{4\beta}\right]\mathrm{d}\boldsymbol{r}.$$

Since V has a minimum at $|\boldsymbol{u}| = \sqrt{\alpha/\beta}$, $|\boldsymbol{u}|$ evolves towards this stationary value. Thus this term enforces a self-propulsion speed without picking the direction of the velocity.

In the system of equations described above, the long-range ordered phase does indeed remain stable. This can be proved by using a dynamical Renormalization Group analysis [9, 23]. The stability of the flocking phase is due to the advective nonlinearities which generate long-range interactions [17]. A qualitative argument for the long-range order in the active spin system, due to Ramaswamy, is as follows [3]: If $u_{||}$ denotes the velocity field in the direction of the flock, then long-wavelength fluctuations $\delta u_\perp$

perpendicular to $u_{||}$ can be excited easily (since it is only the magnitude of the velocity which is fixed by a self-propulsion speed). Given that $\delta u_\perp$ is a velocity, this allows the orienting influence to spread to a distance $\delta u_\perp t$ in time t. This enhances the range of orienting influence compared to the equilibrium system, thus suppressing orientational fluctuations and preserving long-range order.

1.1.3 New phases: turbulence and patterns

The past two decades of active matter research has revealed the existence of several novel phases other than the flocking state, as we briefly noted at the beginning of this chapter. Here we review experimental results about two such phases: turbulent active fluids and vortex array systems. We choose these since they form an important motivation for the present work.

Turbulent active fluid phases have been reported on a variety of systems such as bacterial fluids (Fig. 1.1 (c)) [13, 18, 46, 47], microtubule-kinesin mixtures (Fig. 1.1 (d)) [32, 48] and sperm cell suspensions [20]. The velocity field in these different systems appears qualitatively similar and is characterized by an irregular flow. But why do we not observe polar-ordered phases in these systems? The reason is, as shown by Simha and Ramaswamy, that the hydrodynamic fluctuations make polar-ordered phases unstable in such low-Reynolds number systems [24, 49].

An active turbulence state was first realized in a quasi-2D suspension of *E. coli*, as reported by Wu and Libchaber [46]. The experimental setup consisted of a thin film of the bacterial suspension at moderate density supplemented with polystyrene beads for tracking. Surprisingly, this led to a large-scale coherent motion characterized by swirls and jets much larger than the individual bacterium. In contrast to bioconvection, which results from the response of the microorganisms to some taxes, this bacterial turbulence occurs in the absence of a gradient [22]. Furthermore, the mean-square-displacement, evaluated by tracking the polystyrene beads, shows superdiffusive motion for short times. This arises due to the large-scale coherent motion of the bacterial system. These observations were reproduced with *B. subtilis* by Dombrowski et al. [18] and Wensink et al. [13]. Detailed measurements of velocity correlations and energy spectra of bacterial turbulence have shown that these statistical properties vary considerably from hydrodynamic turbulence [13]. It is also important to note that the phenomenon of bacterial turbulence is not confined to two-dimensional systems; three-dimensional *B. subtilis* system also shows spatio-temporal collective motion similar to turbulence [47]. Apart from bacterial systems, active turbulence has also been reported in spermatozoa suspensions and microtubule-kinesin mixtures. In spermatozoa suspensions, the scaling of the energy spectrum was found to be similar to hydrodynamic turbulence, in contrast to bacterial turbulence [20]. Nevertheless, the observation of turbulent dynamics in such varying settings suggests that the phenomenon is generic to a wide range of stratified active matter systems. Turbulent dynamics in a microtubule system is different from the other examples since microtubule suspensions are nematic active fluids [19, 50, 51] (See section 1.1.4).

Surprisingly, spermatozoa suspensions and microtubule systems also self-organize into well-ordered patterns of coherent vortex arrays [12, 16, 52] (Fig. 1.1 (b)). Active vortex arrays in the spermatozoa system were first reported by Riedel et al. [12]. This experiment involved spermatozoa of sea urchins which self-organize into an array of vortices. However, the vortex centers themselves were found to be dynamic, with a diffusion coefficient larger than expected from thermal fluctuations. Notably, their calculations revealed that the vortex array, although well-structured, does not show crystalline order. Another example of vortex lattice formation in active matter is microtubules propelled by surface-bound dyneins [16]. Most of the theoretical attempts at understanding these patterns have been based on self-propelled-particle models [41, 53]. A field-theoretic treatment of these phases is currently lacking and forms the subject matter of the second half of this dissertation (Chapter 4).

1.1.4 Active liquid crystals as a model for nematic active matter

Structures formed by stabilized microtubules-kinesin motor protein mixtures were first realized to study intracellular self-organization [50, 51]. Later experiments have modified these systems to obtain highly active nematic gels (see Fig. 1.1 (d)) [32]. These systems are characterized by irregular defect dynamics and form a nonequilibrium analog of liquid crystals. As we have discussed already, this is another example of active turbulence, active nematic turbulence. A considerable amount of theoretical and numerical work on active nematics has been conducted based on active extensions of the classical liquid crystal theory [19, 54–57]. Though the physical system as well as the model studied in this dissertation is different, for completeness, here we provide a brief overview of the important results from the liquid crystal based theory of active nematics.

We follow the description of active liquid crystals as given in refs. [19, 54]. The equations of motion for the active liquid crystal theory describes two coarse-grained order parameter fields, an orientational field $\boldsymbol{Q}$ and a velocity field $\boldsymbol{u}$, and is a straightforward extension of the equations of motion for the classical liquid crystal theory. The orientational field is a traceless tensor that describes the alignment of the liquid crystal system; traceless since the system has head-tail symmetry. It can be obtained from the polar orientational vector field (the director field) $\boldsymbol{n}$ by $Q_{ij} = S(n_i n_j - \delta_{ij}/2)$ (in two dimensions). Here S is the magnitude of the order. Then the coupled equations of motion for both the order parameters is given by

Figure 1.3: Particle alignments around defects (shown as red dots) in a liquid crystal system. The image on the left shows a +1/2 defect and the right one shows a $-1/2$ defect.

$$\begin{aligned}\rho(\partial_t u_i + u_k \partial_k u_i) &= \eta \Delta u_i - \partial_i p + \partial_k \sigma_{ik}, \\ \partial_t Q_{ij} + u_k \partial_k Q_{ij} &= \lambda S e_{ij} + Q_{ik}\omega_{kj} - \omega_{ik} Q_{kj} + \gamma^{-1} H_{ij}.\end{aligned}$$

Here p is the pressure term which can be closed by an equation of state or an incompressibility condition, η is the shear viscosity, λ is the flow alignment parameter and γ is the rotational diffusivity. $\boldsymbol{e}$ and $\boldsymbol{w}$ are the rate-of-strain and vorticity tensors respectively and $\boldsymbol{\sigma}$ is the stress tensor which contains the effect of activity. It is given by the sum of elastic and active stresses $\sigma_{ij} = \sigma^e_{ij} + \sigma^a_{ij}$ where

$$\begin{aligned}\sigma^e_{ij} &= -\lambda H_{ij} + Q_{ik} H_{kj} - H_{ik} Q_{kj}, \\ \sigma^a_{ij} &= \alpha Q_{ij}.\end{aligned}$$

Here $\boldsymbol{H}$, which appears both in the expression for the stress tensor and the evolution equation for $\boldsymbol{Q}$, is the molecular tensor that determines the relaxation dynamics of the orientational field. It is given by the derivative of the Landau-de Gennes free energy functional [54]

$$F = \frac{1}{2} \int \mathrm{d}^2 r \left[K |\nabla \boldsymbol{Q}|^2 + C \mathrm{tr} \boldsymbol{Q}^2 (\mathrm{tr} \boldsymbol{Q}^2 - 1) \right],$$

where K and C are material constants.

The sole difference which the model described above has with the classical liquid crystal model is the active stress term given by αQ_{ij} [19]. The presence of activity leads to dynamical features that are otherwise absent; for instance, the active liquid crystal equations result in a turbulent phase at high activity, similar to the turbulent phase observed in microtubule-kinesin mixtures. The major distinction between the passive and the active liquid crystal is that the activity leads to a self-propulsion velocity for the $+1/2$ defects (see Fig. 1.3 for a schematic of the defects in liquid crystal systems) [19]. It is the dynamics of these defects which result in this chaotic turbulence phase. Apart from active turbulence, more ordered phases of active liquid crystals have also been investigated using the active liquid crystal theory. For instance, it has been shown that the active liquid crystal model, confined to a channel flow, can result in a vortex array phase which transitions to turbulence at high activity [56].

1.2 Statistical features of hydrodynamic turbulence

Turbulent phases are exhibited by a variety of active systems ranging from bacterial fluids to microtubule and spermatozoa suspensions. In the first half of this dissertation, we characterize this turbulent dynamics in active fluids. Though qualitatively similar to hydrodynamic turbulence, the properties of active turbulence differ significantly from it. In this section, we provide a brief review of the important statistical features of hydrodynamic turbulence. We focus solely on results relevant to our discussion on active turbulence as presented later in this dissertation (for detailed reviews on the subject, see refs. [58–60]). Henceforth in this section, the term turbulence refers to turbulent dynamics in Newtonian fluids unless specified otherwise.

What distinguishes a turbulent flow from a laminar flow is its irregular and chaotic dynamics. As we noted before, the nature of a fluid flow changes from laminar to turbulent as the nondimensional Reynolds number is increased [21]. The Reynolds number, named in the honor of the first physicist to carefully characterize this transition, is the relative strength of the inertial to the viscous forces, at a particular length scale. It is defined as

$$Re = \frac{UL}{\nu}$$

where L is the length scale of interest, U is the velocity at that scale and ν is the kinematic viscosity.

Given the irregular nature of the flow, it is clear that any theory aimed at studying turbulence should be statistical in nature. As we review below, the multipoint velocity statistics in turbulence are strongly non-Gaussian and lack self-similarity. What makes turbulence both an interesting and difficult field of physics is this nontrivial statistical nature. The starting point for theoretical and numerical analysis of hydrodynamic turbulence is the Navier-Stokes equation which describes the evolution of the fluid velocity field,

$$
\begin{aligned}
\partial_t \boldsymbol{u} + \boldsymbol{u} \cdot \nabla \boldsymbol{u} &= -\nabla \frac{p}{\rho} + \nu \Delta \boldsymbol{u} + \boldsymbol{f}, \\
\nabla \cdot \boldsymbol{u} &= 0.
\end{aligned} \tag{1.2}
$$

Here $\boldsymbol{u}$ is the velocity field, p the pressure, ν the kinematic viscosity and $\boldsymbol{f}$ the forcing term. The second equation enforces the incompressibility condition on the velocity field $\boldsymbol{u}$, which we assume throughout this section. In this section, we provide a summary of experimental and numerical results about the statistical features of turbulence, as well as a description of the turbulence closure model which we make use of in our discussion of active turbulence. All the discussions in this section concern solely with homogeneous and isotropic turbulence: turbulence sufficiently far away from the boundaries so that the effects of the boundary and the anisotropy of the forcing can be ignored.

1.2.1 Velocity statistics and correlations in turbulence

To appreciate the statistical complexity of turbulence, one can look at the scale-dependent features of velocity and vorticity statistics, structure functions, correlations and energy spectra. To illuminate these features, we present here numerical (obtained through direct numerical simulations of Eq. (1.2)) results concerning some of these quantities.

The probability density function (PDF) of the velocity at a single point is close to Gaussian in both two [64] and three dimensions (Fig. 1.4 (a)). However, deviations appear when we start probing quantities such as two-point velocity PDFs. The longitudinal velocity increments, given by $\delta u^E = [\boldsymbol{u}(\boldsymbol{x} + \delta r \hat{\boldsymbol{e}}_i) - \boldsymbol{u}(\boldsymbol{x})] \cdot \hat{\boldsymbol{e}}_i$, show strong non-Gaussian statistical features for small separations δr (Fig 1.4 (d)). The PDF of the vorticity field ($\boldsymbol{\omega} = \nabla \times \boldsymbol{u}$) also shows strong non-Gaussian features (Fig. 1.4 (b)). The statistical features can also be analyzed within the framework of following a tracer particle in the fluid, i.e. the so called Lagrangian frame of reference. The Lagrangian velocity increments are given by $\delta u^L = [\boldsymbol{u}(\boldsymbol{X}(\boldsymbol{x}_0, t_0 + \tau), t_0 + \tau) - \boldsymbol{u}(\boldsymbol{x}_0, t_0)] \cdot \hat{\boldsymbol{e}}_i$, where $\boldsymbol{X}$ denotes the position of the tracer particle. The Lagrangian velocity increment PDFs deviates from Gaussian for small values of τ (Fig 1.4 (e)). Mean-squared-displacement of the tracer particles is another interesting statistical quantity [65]. For short times, the tracers follow a ballistic trajectory. The mean-square-displacement becomes diffusive for longer times. Given this brief overview of the important statistical results from hydrodynamic turbulence, the question before us is how they compare in the context of active turbulence. This forms the subject matter of Chapter 2.

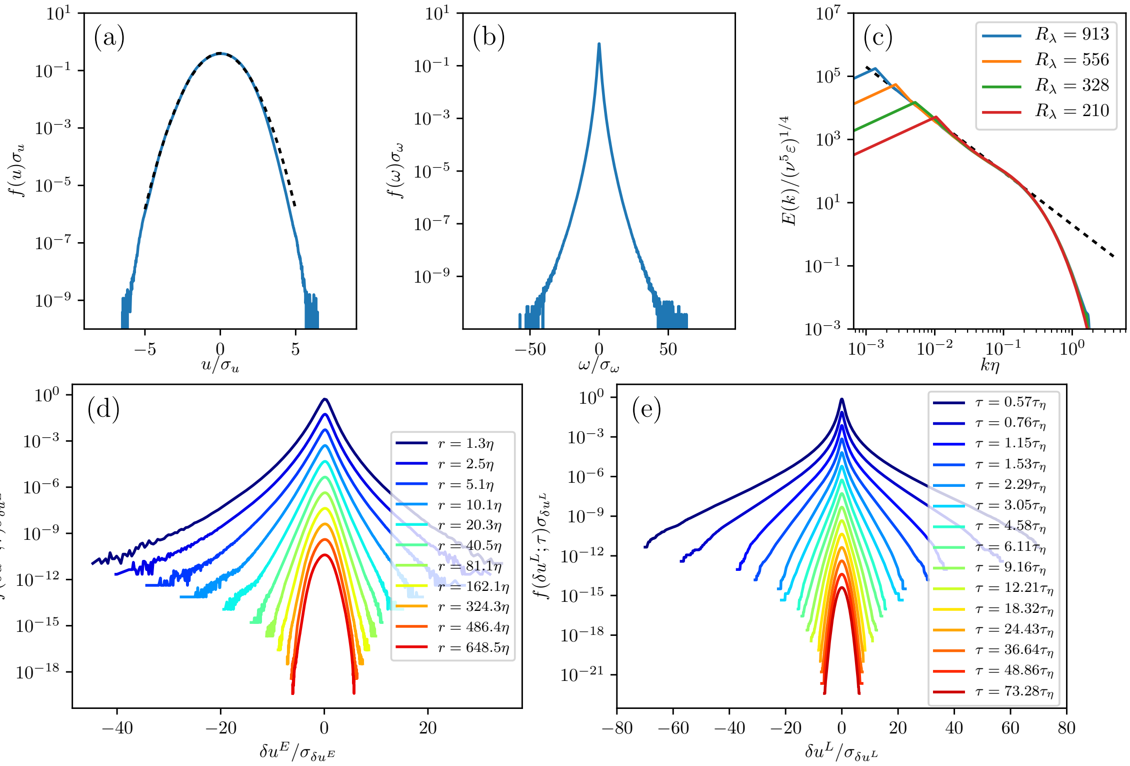

Figure 1.4: Some important statistical quantities in three-dimensional hydrodynamic turbulence obtained through direct numerical simulations of the Navier Stokes equation. Single-point velocity and vorticity distributions are shown in panels (a) and (b), respectively; σ_u and σ_ω are the standard deviations of the respective PDFs. The Taylor microscale Reynolds number (see ref. [61] for definition) $R_\lambda = 330$. (c) Energy spectra for different values of R_λ. ν and ϵ are kinematic viscosity and energy dissipation rates respectively. The wavenumbers are normalized with η, the Kolmogorov scale, which denotes the length scale where viscosity becomes dominant [61]. (d) Eulerian longitudinal velocity increment PDFs ($R_\lambda = 316$). (e) Lagrangian velocity increment PDFs ($R_\lambda = 316$). The temporal increments τ are normalized with τ_η, the Kolmogorov time scale.
Data provided by Cristian Lalescu (MPI DS). Panels (a), (b) and (c) are based on the data analysed in ref. [62] and panels (d) and (e) are based on the data analysed in ref. [63].

1.2.2 Kolmogorov's phenomenological theory of turbulence

Here we present a short review of perhaps the most well-known result in turbulence: Kolmogorov's theory of 1941 (K41) [58, 66]. K41 is a phenomenological theory of turbulence which enumerates several important statistical results about isotropic turbulence. Here we focus on the energy spectrum $E(k)$, the energy density at wavenumber k. In principle, we can write down the evolution equation for $E(k)$ from the Navier-Stokes equation, but we run into a closure problem as we explore in Section 1.2.3. K41 is instead a phenomenological theory that makes no connection to the underlying equations of motion. The starting point is a cascade picture for the energy transfer across scales, due to Richardson [58]. According to this Richardson cascade, energy is transferred across scales in turbulence, from the largest to the smallest, by a breakup of large eddies into smaller ones. Thus, the energy injected at the largest scale gets cascaded to smaller scales, eventually getting dissipated at the smallest scale. K41 assumes that in the intermediate scales between the scales of energy injection and dissipation, the energy spectrum depends only on the energy dissipation rate and the wavenumber. With this assumption, by using dimensional analysis, it follows that $E(k) \propto k^{-5/3}$. The results from experiments as well as numerical simulations (Fig. 1.4 (c)) show that this scaling relation holds surprisingly well [61].

However, we note that many of the assumptions from K41 need not, and do not, hold true for active turbulence. An alternate method to study the energy spectrum and related quantities is by making use of the equations of motion for the fluid, as we explore in the section below.

1.2.3 Closure models

In Chapter 3, we derive a closure model for the active fluids model inspired by the eddy-damped quasi-normal Markovian (EDQNM) closure scheme from the hydrodynamic turbulence theory. In this section, we provide an overview of the results from the turbulence theory leading to this closure scheme. For detailed reviews on the topic, see refs. [67–72]. Below, we mostly follow the discussion given in ref. [67].

Our goal is to derive an evolution equation for the energy spectrum density $E(k)$ in three dimensions in the closed form. This is difficult to achieve due to the nonlinear terms in the Navier Stokes equation which couples $E(k)$ to higher-order terms. To see this, let us start by defining $E(k)$ [73]

$$E(k) = \left(\frac{L}{2\pi}\right)^3 2\pi k^2 \left\langle \hat{\boldsymbol{u}}(\boldsymbol{k}) \cdot \hat{\boldsymbol{u}}(-\boldsymbol{k}) \right\rangle .$$

where $\hat{u}_i(\boldsymbol{k})$ are the coefficients of the Fourier series expansion of the velocity field given by

$$u_i(\boldsymbol{x}) = \sum_{\boldsymbol{k}} \hat{u}_i(\boldsymbol{k}) e^{i\boldsymbol{k}\cdot\boldsymbol{x}}.$$

The coefficients $\hat{u}_i(\boldsymbol{k})$ can be evaluated as

$$\hat{u}_i(\boldsymbol{k}) = \frac{1}{L^3} \int u_i(\boldsymbol{x}) e^{-i\boldsymbol{k}\cdot\boldsymbol{x}} \mathrm{d}\boldsymbol{x}.$$

where the integration is over the domain dimensions $[0, L]$.

The Navier Stokes equation, in Fourier space, takes the form

$$\partial_t \hat{u}_i(\boldsymbol{k}) + \nu k^2 \hat{u}_i(\boldsymbol{k}) = -ik_i \hat{p}(\boldsymbol{k}) - ik_j (\widehat{u_j u_i})(\boldsymbol{k}),$$

where $\hat{f}$ denotes the Fourier transform of f.

Multiplying the above equation by $\hat{u}_i(-\boldsymbol{k})$, and using the corresponding equation for $\hat{u}_i(-\boldsymbol{k})$ the evolution equation for the energy spectrum can be obtained:

$$\partial_t E(k) + 2\nu k^2 E(k) = -2\pi \mathrm{i} k^2 k_j \left\langle (\widehat{u_j u_i})(\boldsymbol{k}) u_i(-\boldsymbol{k}) \right\rangle - 2\pi \mathrm{i} k^2 k_j \left\langle (\widehat{u_j u_i})(-\boldsymbol{k}) u_j(\boldsymbol{k}) \right\rangle . \quad (1.3)$$

Here the pressure term vanishes due to isotropy [74]. The above equation shows that the evolution equation for $E(k)$ couples to the third-order terms. An equation for the third-order term would similarly couple to higher-order terms, illustrating the closure problem. Thus to arrive at a closed set of equations, we need a closure approximation at some level.

One of the simplest closure schemes is the quasi-normal (QN) approximation proposed by Millionshtchikov [68, 71, 75]. To start with, let us recall a property of the moments of Gaussian random functions with zero mean; any odd-order moment of the random function is zero and any even-order moment can be expanded in terms of second-order moments. To put it differently, the cumulant, which is the difference between the actual moment and the corresponding Gaussian factorization, is zero. Assuming that the velocity field follows a Gaussian distribution, at the level of Eq. (1.3), would disregard the nonlinear advection term entirely and is unphysical. The QN approximation instead factorizes the fourth-order moments without any approximation on the third-order moments. To this end, we write down the evolution equation for the third-order moments and factorize the fourth-order moments assuming Gaussianity.

$$(\partial_t + \nu(k^2 + p^2 + q^2)) \left\langle \hat{u}_i(\boldsymbol{k}) \hat{u}_j(\boldsymbol{p}) \hat{u}_l(\boldsymbol{q}) \right\rangle = \left\langle \hat{u}\hat{u}\hat{u}\hat{u} \right\rangle = \sum \left\langle \hat{u}\hat{u} \right\rangle \left\langle \hat{u}\hat{u} \right\rangle .$$

Here $\langle \hat{u}\hat{u}\hat{u}\hat{u} \rangle$ denotes the fourth-order moments arising from the advective term and $\sum \langle \hat{u}\hat{u} \rangle \langle \hat{u}\hat{u} \rangle$ the corresponding factorization [59]. The above equation and Eq. (1.3) form a closed set of equations which can be numerically solved to obtain the energy spectrum.

However, the evaluation of the energy spectrum following this QN approximation leads to negative energy spectra [69, 70]. This is unphysical since the energy spectrum is positive by definition. The reason for the energy spectrum becoming negative is the excessive build-up of the third-order moments in QN approximation [76]. Thus the discarding of the fourth-order cumulants leads to excessive transfer of energy to smaller scales.

How do we compensate for the excessive energy transfer? One solution is to add a damping term to the equations of motion, which accounts for the discarded fourth-order cumulants. Then the equation for the third-order moment takes the form

$$(\partial_t + \nu(k^2 + p^2 + q^2) + \mu_{kpq}) \langle \hat{u}_i(\boldsymbol{k})\hat{u}_j(\boldsymbol{p})\hat{u}_l(\boldsymbol{q})\rangle = \sum \langle \hat{u}\hat{u}\rangle \langle \hat{u}\hat{u}\rangle .$$

Here $\mu_{kpq} = \mu_k + \mu_p + \mu_q$ is the damping term discussed above. A dimensionally consistent form of this damping term is $\mu_k = \gamma \left(\int_0^k s^2 E(s,t) ds\right)^{1/2}$, where γ is a free parameter [67]. The physical effect which this term models is the deformation rate of the eddies of size k^{-1} by the larger eddies, and consequently can be thought of as an eddy damping term [67]. Thus this scheme is called the eddy-damped quasi-normal (EDQN) approximation [76, 77].

The above equation is integrated and substituted in Eq. (1.3) resulting in a closed expression for the energy spectrum which, in symbolic terms, is given below.

$$\begin{aligned}&(\partial_t + 2\nu k^2)E(k) = \\ &\int_0^t \mathrm{d}\tau \int_{\boldsymbol{p}+\boldsymbol{q}+\boldsymbol{k}=0} \exp[-[\nu(k^2 + p^2 + q^2) + \mu_{kpq}](t-\tau)] \sum \langle \hat{u}\hat{u}\rangle \langle \hat{u}\hat{u}\rangle (\tau)\mathrm{d}\boldsymbol{p}.\end{aligned}$$

A further simplification can be made by noting that the integrand term $\sum \langle \hat{u}\hat{u}\rangle \langle \hat{u}\hat{u}\rangle$ can be pulled out of the time integral assuming that its characteristic time is much larger than the characteristic time of the exponential term, given by $[\nu(k^2+p^2+q^2)+\mu_{kpq}]^{-1}$. Also, another simplification can be made by neglecting the time variation of the μ_{kpq}, allowing us to evaluate the time integral and by taking the long time limit. These approximations are termed Markovianization. This results in

$$(\partial_t + 2\nu k^2)E(k) = \int_{\boldsymbol{p}+\boldsymbol{q}+\boldsymbol{k}=0} \theta_{kpq} \sum \langle \hat{u}\hat{u}\rangle \langle \hat{u}\hat{u}\rangle \,\mathrm{d}\boldsymbol{p},$$

where

$$\theta_{kpq} = \frac{1}{\nu(k^2 + p^2 + q^2) + \mu_{kpq}}. \tag{1.4}$$

The above approximation, called the eddy-damped quasi-normal Markovian (EDQNM) scheme, has been successfully used to calculate the energy spectra in hydrodynamic turbulence [67, 72]. In Chapter 3, we use this method to evaluate the energy spectra and

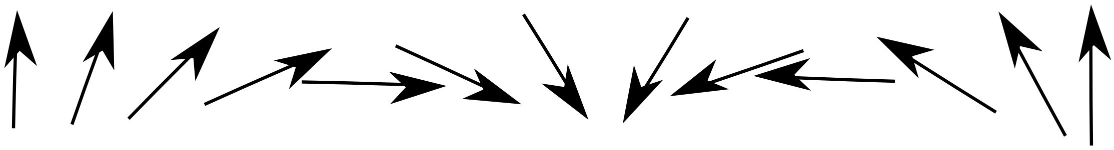

Figure 1.5: A schematic representation of a spin wave spanning the entire domain length (see also ref. [78])

velocity correlations in active turbulence.

1.3 Melting in two-dimensions

As we discussed in the previous sections, the fact that an active XY model can show global order in apparent violation of the Mermin-Wagner-Hohenberg theorem is a surprising result with important ramifications. The vast majority of results in active matter is centered around studying properties of such globally ordered 'flocking' phases in active matter. A natural follow-up question to these results is whether the active matter analogs of other phases in condensed matter systems exist too. For instance, how do the properties of crystals in active systems differ from their equilibrium counterparts? The second half of this dissertation is concerned primarily with this question. We investigate a vortex crystal phase in active matter and study its melting into an active fluid. In this section, we provide an overview of the important results on melting in two-dimensions, which are relevant to our later discussions. We mostly follow the review by Strandburg [78].

Before we delve into the properties of two-dimensional crystals, let us start with a reminder about ordering and phase transitions in the XY model. The Hamiltonian of the XY model is given by

$$H = -J \sum_{\langle ij \rangle} \boldsymbol{s}_i \cdot \boldsymbol{s}_j$$

where the spins $\boldsymbol{s}_i$ are constrained to move only in two dimensions. J is the coupling constant and the summation is over all the nearest neighbors. It was rigorously proven by Mermin and Wagner that the long-range order of spin-spin correlations in the XY model decays to zero in dimensions $d \leq 2$ [6]. An approximate way to see how the long-range order is dimension dependent, due to Peierls, is as follows [78]: Consider a long-wavelength spin-wave spanning the entire domain L of the system (see Fig. 1.5 for a schematic representation). If we assume the deviations between the neighboring spins to be small, the energy per spin can be approximated as a quadratic function of the angular deviation. The energy per spin is then proportional to $(2\pi/L)^2$, where

L is normalized with the dimension of each spin. Thus the total energy will be given by the product of the number of spins with energy per spin. Thus it is proportional to $L(2\pi/L)^2, L^2(2\pi/L)^2$ and $L^3(2\pi/L)^2$ in one, two and three dimensions respectively. The total energy being finite in one and two dimensions implies that these spin waves can destroy long-range order at any non-zero temperature. Note that this is in contrast to the two-dimensional Ising model, with discrete spins, which shows a phase transition to ordered state at low temperatures [79].

Although the spin-spin correlations decay to zero in the XY model, it does so algebraically at low temperatures, thus defining a quasi-long range order. Thus, the XY model exhibits two distinct phases: a quasi-long range ordering of spin-spin correlations and a disordered phase. A theory describing the phase transition from a quasi-long-range ordered phase to a short-range ordered phase was advanced by Kosterlitz and Thoules [66]. According to this theory, the transition occurs when the pairs of topological defects formed by the spin vortices of opposite polarity get unbound. It predicts a continuous transition from the quasi-long range ordered phase at low temperatures to the short-range ordered phase at a higher temperature.

1.3.1 Phase transitions in equilibrium crystals

The difficulty of defining a crystalline order in two dimensions follows from the Mermin-Wagner-Hohenberg theorem [7]. In three dimensions, crystals can be defined by identifying a periodic arrangement of the constituent particles. For instance, the positional correlation function of the constituent particles will show peaks even at arbitrarily large separations. However, Mermin proved in 1968, as an extension of the results on the XY model, that such long-range positional order cannot exist in two dimensions at any non-zero temperature [7]. The positional order in two-dimensional crystals, at sufficiently low temperatures, decays algebraically thus showing quasi-long range order. So how do we define crystalline order in two dimensions? Apart from the positional order, crystals are also characterized by an orientational order. An orientational order parameter captures the local 6-fold ordering (in the case of a hexagonal crystal) of the neighbors for every particle in a crystal. It can be defined as $\psi_i = \sum_j \exp(6\mathrm{i}\theta_{ij})/\mathrm{N}(i)$ for each lattice site i. Here, θ_{ij} is the angle between the line connecting the neighbors i and j and an arbitrary axis, and $\mathrm{N}(i)$ is the number of neighbors. The orientational correlation is then given by the two-point correlation of this order parameter

$$G_6(r) = \langle \psi_i^* \psi_j \delta(r - r_{ij}) \rangle \,/\, \langle \delta(r - r_{ij}) \rangle \tag{1.5}$$

where r_{ij} is the distance between i and j, and the average is over all lattice sites i and j. (See also ref. [78] and Chapter 4). Although two-dimensional crystals do not show long-range positional order, they do show long-range orientational order [81]. Thus a

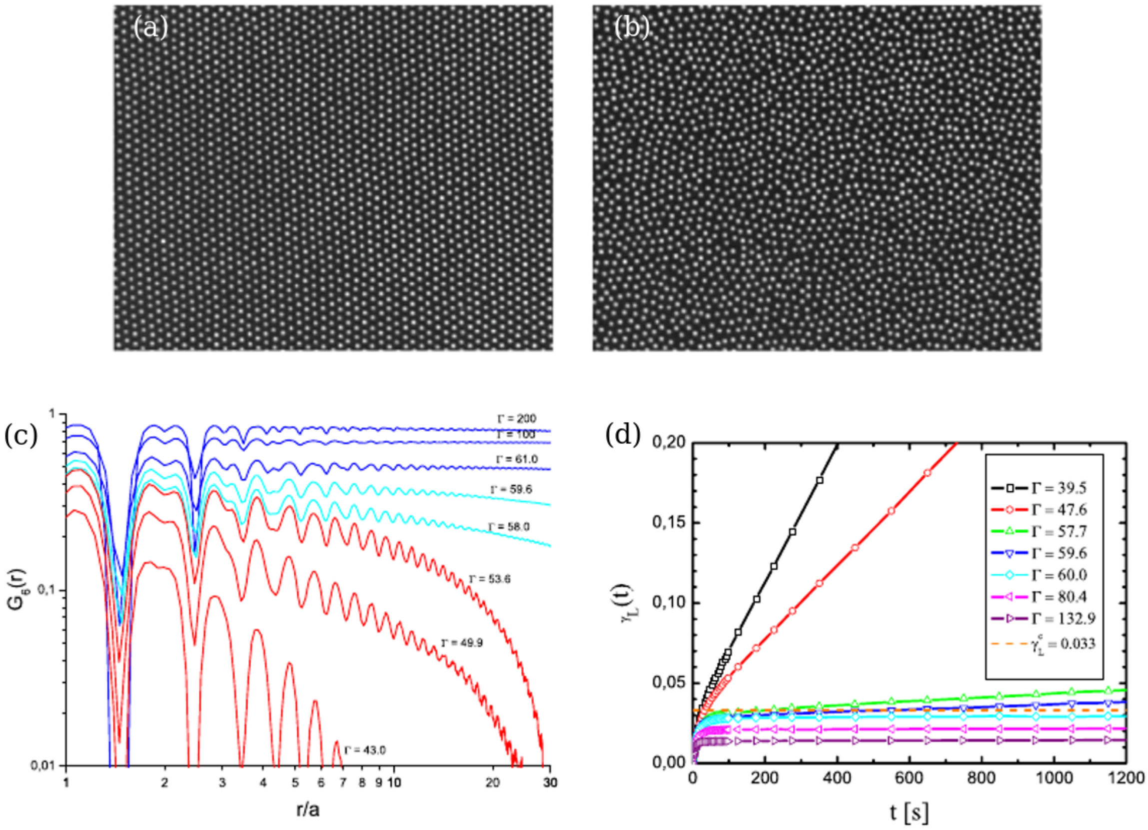

Figure 1.6: Melting process in a two-dimensional polystyrene colloidal system experiment. The polystyrene spheres are embedded with Fe_2O_3, making them super-paramagnetic (i.e. there is no spontaneous magnetization in the absence of an external magnetic field, however the magnetic susceptibility is larger than typical paramagnets). The transition is triggered by varying the magnetic field. The colloidal system in the crystal (a) and fluid (b) phases, at high and low magnetic field respectively, show considerable qualitative differences. The hexatic phase is not shown since it is difficult to visually distinguish from the fluid phase. (c) Orientational correlation function and (d) dynamic Lindemann parameter for crystal, hexatic and fluid phases. Γ is the interaction parameter that characterizes the relative strength of magnetic energy to thermal energy. Figures reproduced with permission from ref. [80].

two-dimensional crystal is characterized by quasi-long range positional order and long-range orientational order.

Another related parameter in the context of crystalline order is the so-called Lindemann parameter [82]. It is proportional to the standard deviation of the position of the constituent particles from their mean positions. In a three dimensional crystal, the vibrations remain small and the Lindeman parameter is smaller than the lattice spacing. However, in two-dimensional crystals, the standard Lindemann parameter diverges with domain size [83]. Alternatively, we can define a modified dynamic Lindemann parameter, which evaluates the relative separation of neighboring particles, instead of their absolute deviation [83, 84]. (See Eq. (4.2) in Chapter 4 for a formal definition). This dynamic Lindemann parameter remains bounded for crystals in two dimensions.

Fig. 1.6 (a) shows a two dimensional crystal formed in a colloidal system. Fig. 1.6 (c) and (d) show the orientational correlation function which characterizes the orientational order and the dynamic Lindemann parameter respectively. For the crystal state, the orientational correlation function asymptotically reaches a non-zero constant while the dynamic Lindemann parameter remains bounded.

How do crystals in two dimensions melt? There exist several competing theories on the melting process of two-dimensional crystals. The most famous of these is an extension of the Kosterlitz-Thouless theory for the XY model to crystals, called Kosterlitz-Thouless-Halperin-Nelson-Young (KTHNY) theory [66, 85, 86]. It predicts that the melting is driven by thermally activated dislocation pairs which get unbound. This unbinding proceeds through a continuous phase transition and results in a phase with quasi-long-range orientational order, but no positional order. This is the so-called hexatic phase of a two-dimensional crystal. Further increasing the temperature leads to another continuous transition where the dislocations get unbound, resulting in an isotropic fluid phase. Experiments on colloidal systems as well as numerical simulations have verified the KTHNY melting theory [78, 83, 84].

There also exist alternate theories on the melting of two-dimensional crystals [87, 88]. One of the examples is a grain-boundary induced melting theory [88]. A grain boundary in a two-dimensional crystal is a line defect caused by a collective excitation of dislocations. According to this theory, the melting proceeds through the coupling of grain boundaries and dislocation pairs, which results in a discontinuous transition which preempts the KTHNY melting.

1.3.2 Nonequilibrium crystals in active systems

Here we review some of the experimental and numerical results concerning nonequilibrium crystals. Interestingly, experiments on nonequilibrium crystalline systems have resulted in melting scenarios similar to the one predicted by the KTHNY theory. One example is the melting of ferrofluid spikes. Ferrofluids are colloidal liquids made of ferromagnetic particles which in the presence of a magnetic field may form spikes [89]. It has been shown that the melting of ferrofluid spikes, which self-organize into a hexagonal crystal, proceeds through an intermediate hexatic phase [89]. Experimental and numerical studies have also been conducted on granular systems and thin films with polymer additives [90, 91]

Within active matter, experiments have looked at patterns and structures such as clusters of active particles and vortex arrays. Active colloidal systems have been used as an experimental framework to study crystallization in active matter. Light mediated Janus particles (Fig. 1.1 (f)) cluster to form local crystalline structures [15]. These local clusters break-up and reform elsewhere resulting in “living crystals”. Experiments on chemically activated colloidal systems have also resulted in crystalline structures [92]. Among biological active matter, *T. majus* bacteria form local crystalline patches [93].

As we noted before, active vortex arrays form another candidate to study crystalline states in active matter. Experiments have revealed that microtubule suspensions may form irregular vortex lattices under suitable conditions [16]. Spermatozoa systems have been observed to form self-organized well-ordered vortex arrays [12] (Fig. 1.1 (f)). It is important to note that the measurements in this experiment showed a fluid-like arrangement of the active vortices rather than hexatic or crystal-like [12]. However, what is interesting is that spermatozoa suspensions have also been shown to exhibit a turbulent phase [20], pointing at the possibility of achieving a melting transition in this system. To the best of author’s knowledge, this is the closest experimental realization of an active vortex crystal, which we theoretically investigate in Chapter 4.

Modeling of active vortex crystals has been attempted through self-propelled particle (SPP) models as well as through field theories. Analysis of active crystals in two-dimensions, by using SPP models, has revealed that the melting proceeds through an intermediate hexatic phase, like in the KTHNY theory [94]. Apart from these, continuum models such as active extensions of phase-field crystal models have been used to investigate crystalline order in active matter [95, 96].

1.4 Continuum model for active turbulence and vortex crystals

So far we have traced the development of the field of active matter and discussed briefly some of the main results from hydrodynamic turbulence and two-dimensional crystals. In the succeeding chapters, we theoretically and numerically investigate turbulent dynamics and crystallization in active matter. Our investigations are based on a continuum theory for active matter adapted from a theory of active turbulence [13, 26].

Let us begin by noting that a possible starting point for a theoretical analysis of active matter is a dynamical evolution equation for the order parameter(s). For the dry active matter, the Toner-Tu equations [11, 23] given by Eq. (1.1) provide such a hydrodynamic theory; it is called hydrodynamic since the variables of interest evolve slowly at the long-wavelength limit. This theory successfully explains the emergence of long-range order in dry active matter. However, as we already noted, in low-Reynolds number systems where hydrodynamic interactions are important, like in bacterial suspensions, a polar-ordered phase is unstable [24]. To account for this, a simplified version of the Toner-Tu equation can be supplemented with linear instability. Such a theory was advanced to study the active turbulence phase in bacterial systems and forms our main model [13]. In this section, we introduce this main model and provide a phenomenological derivation arriving at the equations of motion. We end this section by presenting a nonequilibrium phase diagram detailing the different states of the active matter model.

1.4.1 A phenomenological derivation of the active matter model

One of the ways to arrive at a continuum model describing the active matter dynamics is to start from a generalized hydrodynamic equation of motion and then incorporate the stresses resulting from the activity. Here we present such a phenomenological derivation of the active fluids model following the discussion given in refs. [13, 26]. We start with a generalized Navier-Stokes equation given by

$$\begin{aligned}\nabla\cdot\boldsymbol{u} &= 0,\\ \partial_t\boldsymbol{u}+\boldsymbol{u}\cdot\nabla\boldsymbol{u} &= -\nabla p-(\alpha+\beta\boldsymbol{u}^2)\boldsymbol{u}+\nabla\cdot\boldsymbol{E}.\end{aligned} \tag{1.6}$$

Here $\boldsymbol{u}$ is the coarse-grained velocity field of the active fluid. The pressure term p is a Lagrange multiplier that enforces the incompressibility condition. E is a generalized stress tensor which we discuss below. The term $-(\alpha+\beta\boldsymbol{u}^2)\boldsymbol{u}$, like in the Toner-Tu equations, models the driving of the system to a local stationary value for $|\boldsymbol{u}|$. When $\alpha > 0$ the active fluid is damped to a zero velocity state. However, when $\alpha < 0$ a non-zero stationary value for the velocity field is selected. But since a global polar order in low-Reynolds number systems is unstable [24], there are other instability mechanisms at work. One possible way to incorporate these instabilities is by destabilizing the theory with a suitable choice for the active stress. To this end, the following form for the stress tensor, which combines these instabilities together with an active nematic stress term, can be used.

$$E_{ij} = -\Gamma_0(\partial_i u_j+\partial_j u_i)-\Gamma_2\Delta(\partial_i u_j+\partial_j u_i)+Sq_{ij}.$$

Here the Γ terms are the gradient expansion of the stress tensor truncated at second order. When $\Gamma_0 > 0$ and $\Gamma_2 > 0$, this stress tensor could render a band of unstable wavenumbers, modeling the effect of the instabilities. Here q_{ij} is the $\boldsymbol{Q}$-tensor and S is the magnitude of the orientation field (see section 1.1.4). Utilizing a mean field approximation for the orientation field, results in

$$q_{ij} = u_i u_j - \frac{\delta_{ij}}{d}|\boldsymbol{u}|^2.$$

Substituting this into Eq. (1.6), and after defining $\lambda_0 = 1 - S$ and $\lambda_1 = -S/d$, we arrive at the equations of motion describing the active fluid:

$$\begin{aligned} \partial_t \boldsymbol{u} + \lambda_0 \boldsymbol{u} \cdot \nabla \boldsymbol{u} &= -\nabla p + \lambda_1 \nabla \boldsymbol{u}^2 - (\Gamma_0 \Delta + \Gamma_2 \Delta^2 + \alpha + \beta \boldsymbol{u}^2)\boldsymbol{u}, \\ \nabla \cdot \boldsymbol{u} &= 0. \end{aligned} \tag{1.7}$$

Here the parameter λ_0 incorporates the effect of both passive advection as well as the active nematic stresses. Thus it can be thought of as an active advection parameter.

The set of equations given by Eq. (1.7) form the starting point for the results presented in Chapters 2, 3 and 4. To simplify the parameter space, note that the λ_1 term can be absorbed into the pressure term. To nondimensionalize the resulting equation, we define a timescale $T = 4\Gamma_2/\Gamma_0^2$ and a length scale $L = \sqrt{-2\Gamma_2/\Gamma_0}$. The parameters are mapped according to $\lambda_0 \to \lambda$, $\Gamma_0 T/L^2 \to -2$, $\Gamma_2 T/L^4 \to 1$, $\alpha T \to \alpha + 1$ and $\beta L^2/T \to \beta$. This results in the following equation

$$\partial_t \boldsymbol{u} + \lambda \boldsymbol{u} \cdot \nabla \boldsymbol{u} = -\nabla p - (1 + \Delta)^2 \boldsymbol{u} - \alpha \boldsymbol{u} - \beta \boldsymbol{u}^2 \, \boldsymbol{u}. \tag{1.8}$$

One more parameter can be scaled out from Eq. (1.8), thus the effective parameter set contains two elements, which we choose to be λ and α. We also note that the active matter equations of motion presented here can be approximately obtained from the microscopic dynamics of a dense system of self-propelled particles [97, 98].

At this point, it is instructive to take an alternate look at the active matter model. The model can be thought of as an advected Swift-Hohenberg-like equation. To see this, let us write down the equations in the vorticity formulation, obtained by taking the curl of Eq. (1.8) (we discard the mean velocity for the sake of this discussion),

$$\partial_t \omega + \lambda \boldsymbol{u} \cdot \nabla \omega = -(1 + \Delta)^2 \omega - \alpha \omega - \beta \nabla \times \boldsymbol{u}^2 \, \boldsymbol{u}. \tag{1.9}$$

Thus, the model for the pseudoscalar vorticity field is a Swift-Hohenberg-like equation advected by a velocity field $\boldsymbol{u}$ where $\nabla \times \boldsymbol{u} = \omega$ (Appendix B).

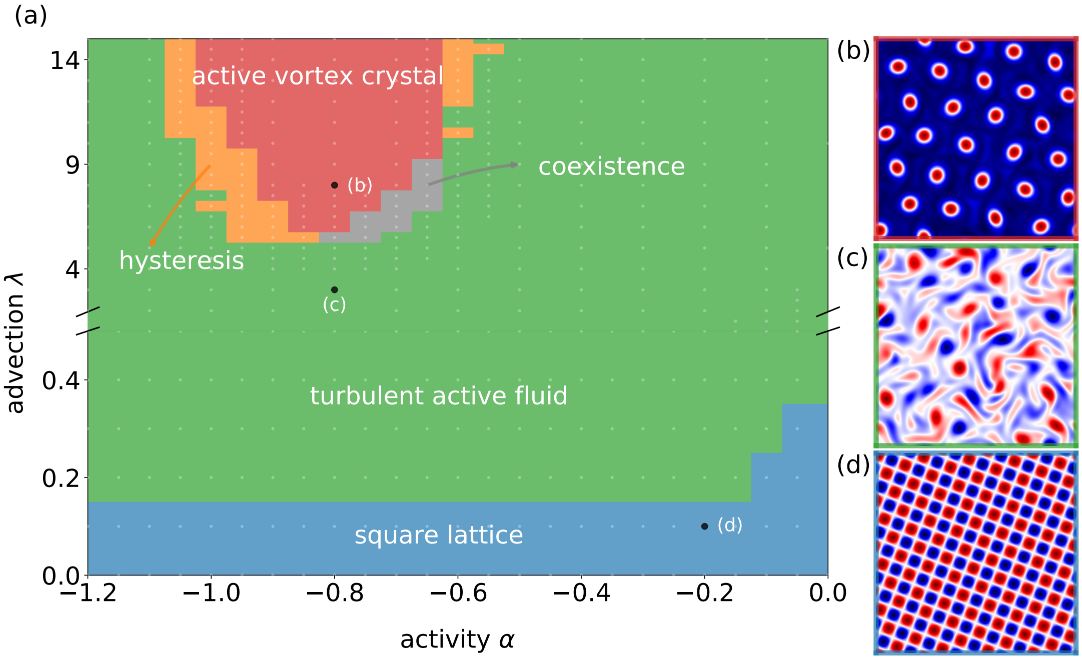

Figure 1.7: (a) Nonequilibrium phase diagram of the active fluids model. The red, green and blue regions correspond to (b) vortex crystal, (c) active turbulence and (d) square lattice phases (as exemplified by their vorticity fields) respectively. The grey and the orange regions are the marginal stability regions for the transition between active turbulence and vortex crystal. See also Chapter 4.

1.4.2 Nonequilibrium phase diagram

Having introduced the active matter model, one of the questions before us is what phases of the active matter systems does it capture. To answer this, we present in Fig.1.7 (a) the nonequilibrium phase diagram of the active matter model as a function of the two free parameters advection λ and activity α. This is obtained through a simulation of the equations of motion by using a pseudospectral algorithm (Appendix A) on a $20\pi \times 20\pi$ domain using 256×256 grid points (see Chapter 4 for more details about the simulations). As Fig. 1.7 (b) and (c) show, the active matter model does capture both the vortex crystal phase and the active turbulence. Here we provide a short description of these and other phases shown in the phase diagram. This brief account serves as a useful pointer to our discussions about the different phases of active matter in the subsequent chapters.

- **Square lattice.** When the advection parameter λ is close to zero, Eq. (1.8) results in a square lattice solution for the vorticity field (Fig. 1.7 (d)). This is shown in blue in the phase diagram. When $\lambda = 0$, the equations of motion reduce to a variant of the Swift-Hohenberg model which can be analyzed by using the tools from classical pattern formation theory. We present this analysis in Chapter 3. Interestingly, these patterns remain stable for non-zero, but small, values of advection. This can be studied by using linear stability analysis (Appendix C).

- **Active turbulence.** As the advection parameter is increased, a dynamic phase corresponding to active turbulence emerges (Fig. 1.7 (c)). The green region in the phase diagram corresponds to this active turbulence phase. What characterizes the active turbulence state is the seemingly chaotic vortex dynamics. Analysis and characterization of this active turbulence phase is the subject matter of Chapters 2 and 3.
- **Active vortex crystal.** Fig. 1.7 (b) shows a snapshot of the active vortex crystal phase. Vortex crystals are a broken symmetry phase of a regular arrangement of dynamic vortices, which emerge from a turbulent transient. This phase is observed in the red region in the phase diagram. In Chapter 4 we analyze the properties of these crystalline phases.
- **Transition region.** The grey and orange regions in the phase diagram correspond to the transition between the vortex crystal and the active fluid. In the grey region, the solutions to the active fluid model are hysteretic - the vortex crystals are stable solutions but do not spontaneously emerge from random initial conditions. In the orange region, one the other hand, we observe temporally and spatially intermittent patterns. The analysis of this transition forms a major part of Chapter 4.

1.5 Outline

In this dissertation, we explore turbulent and crystalline phases in active fluids phenomenologically. Our focus is on the following two questions:

- What are the characteristics of the turbulent phase in active fluids and how does it compare to hydrodynamic turbulence?
- Do active flows form crystalline phases and how do these nonequilibrium crystals melt?

We use numerical modeling of active flows as well as theoretical analysis to answer these questions. The outline of the rest of the dissertation is as follows.

In the next chapter, we conduct a comprehensive statistical characterization of the active turbulence phase. We study the velocity and the velocity increment statistics in this phase both in the Eulerian and the Lagrangian framework. Furthermore, deviations in the small-scale statistics from Gaussianity are also investigated. We also study particle dispersion in active turbulence and characterize vortex dynamics in active turbulence. We end this chapter by comparing the properties of active turbulence with hydrodynamic turbulence.

The statistical features of the active turbulence phase are further explored in Chapter 3. We develop a closure theory for velocity correlations and energy spectra in active turbulence by using the EDQNM closure approximation. We compare the results obtained through this scheme with the results from full simulations of the equations of motion. Furthermore, the energetics in the active matter system is also analyzed by quantifying the contributions to the energy spectrum from different mechanisms.

Chapters 4 is concerned with crystalline phases in active fluids. Here we describe the properties of the vortex crystal phase which occurs as a solution to the active fluids model. We analyze the emergence of these crystals and their melting into an active fluid. The properties of the phase transition in the small domain are compared with those from large domains. The finite-size effects in this system are explored in the context of the emergence of the vortex crystal phase. We end this dissertation with a detailed discussion of all the results.

2 Manuscript I: Vortex dynamics and Lagrangian statistics in a model for active turbulence

This manuscript originally appeared as "James, M., & Wilczek, M. (2018). Vortex dynamics and Lagrangian statistics in a model for active turbulence. The European Physical Journal E, 41(2), 21." and is licensed under the Creative Commons Attribution 4.0 International License (https://creativecommons.org/licenses/by/4.0). Supplementary videos are available at DOI: 10.1140/epje/i2018-11625-8.

MW designed the research. MJ wrote the DNS code, conducted the simulations and analyzed the data. Both authors contributed to the interpretation of the results and the writing of the manuscript.

Vortex dynamics and Lagrangian statistics in a model for active turbulence

2.1 Abstract

Cellular suspensions such as dense bacterial flows exhibit a turbulence-like phase under certain conditions. We study this phenomenon of "active turbulence" statistically by using numerical tools. Following Wensink et al. [Proc. Natl. Acad. Sci. U.S.A 109:14308 (2012)], we model active turbulence by means of a generalized Navier Stokes equation. Two-point velocity statistics of active turbulence, both in the Eulerian and the Lagrangian frame, is explored. We characterize the scale-dependent features of two-point statistics in this system. Furthermore, we extend this statistical study with measurements of vortex dynamics in this system. Our observations suggest that the large-scale statistics of active turbulence is close to Gaussian with sub-Gaussian tails.

2.2 Introduction

Active systems such as a flock of birds, a swarm of bacteria or active colloids form fascinating meso-scale structures with long-range order exceeding the sizes of individual agents by an order of magnitude or more [1, 28, 99–101]. Theories describing the formation and evolution of such meso-scale coherent structures in active systems have been a topic of active research in the past two decades [1–3, 10, 23, 42, 102, 103]. It is known that the core features of these diverse phenomena can be modeled by taking into account just a few dynamical effects such as self-propulsion and inter-particle interactions [1, 10, 102].

Arguably the most diverse of these phenomena occurs at the smallest of the biological scales where collective dynamics of microbes or intra-cellular structures results in interesting spatio-temporal patterns and non-trivial dynamical features. Among these is the phenomenon of "active turbulence" – chaotic dynamics of dense suspensions – which has been observed in bacterial as well as microtubule systems [18, 32]. In particular "bacterial turbulence" has been recently observed in quasi two-dimensional suspensions of *B. Subtilis* [13, 104]. While the phenomenon shows considerable qualitative similarity with hydrodynamic turbulence by virtue of which it gets its name, active turbulence displays an intrinsic length-scale selection absent in hydrodynamic turbulence, which is characterized by the formation of stable vortices of approximately constant sizes [13, 105]. This typical scale is larger than the scale on which the driving occurs as the result of an upscale energy transport. This inverse energy transfer is well-known from two-dimensional Navier-Stokes turbulence forced at small scales [106, 107]. The main difference is that in a passive Navier-Stokes fluid, the forcing has to be applied externally.

The chaotic nature of active turbulence calls for a statistical investigation and forms the subject matter of this study. Our objective here is to provide an extensive statistical study of this phenomenon by using numerical simulations. Our analysis is based on a recently introduced minimal continuum model for active turbulence [13], the details of which are presented in sect. 2.3. As an example, fig. 2.1(a) shows a snapshot of the vorticity field of the active turbulent system in the statistically stationary state obtained through direct numerical simulation. The corresponding supplementary movie 1 shows the evolution of this field with time. Note that the intense vortices in this system are stable and have a long lifetime.

In this work, we study both the Eulerian and the Lagrangian properties as well as the characteristics of vortex dynamics in this system. Previous works on this subject have dealt with the Eulerian properties of the active turbulence field, see *e.g.* ref. [105]. In sect. 2.4 we extend this further with two-point velocity statistics and vorticity statistics to set a reference for the subsequent investigations after introducing the active turbulence model in sect. 2.3. In sect. 2.5 we study the transport properties of the active turbulence field by investigating both the vortex dynamics and the Lagrangian features.

In the context of active turbulence, Lagrangian measurements describe the properties of tracer particles of the locally averaged velocity of the bacterial field, providing insights into transport properties and mixing of bacterial suspensions. Measurements of this kind provide a framework to better understand the experimental works on bacterial dispersion [108] and dynamics of small objects in bacterial baths [46].

2.3 The active turbulence model

Regarding the mathematical modeling of active flows, a continuum description appears suitable whenever larger-scale flow structures compared to the individual extents of the active agents are of interest. For example, such a continuum description has been established based on a coupled set of equations of two order parameter fields – the velocity field and the local orientation of the active agents [54, 109–111]. This level of description is particularly useful for characterizing the role of defects on the active dynamics [55, 112]. An even simpler, minimal model for bacterial turbulence has been introduced in refs. [13, 26]. We here further investigate this model in two dimensions, in which the locally coarse-grained bacterial velocity field is considered as the only order parameter. This assumption is based on the premise that in a dense suspension the local orientation of bacteria aligns with that of the velocity field. The equations for the coarse-grained order parameter field $\boldsymbol{u}$ take the form

$$\begin{aligned} \partial_t \boldsymbol{u} + \lambda_0 \boldsymbol{u} \cdot \nabla \boldsymbol{u} &= -\nabla p - (\Gamma_0 \Delta + \Gamma_2 \Delta^2 + \alpha + \beta \boldsymbol{u}^2)\boldsymbol{u} \\ \nabla \cdot \boldsymbol{u} &= 0 \end{aligned} \tag{2.1}$$

The pressure gradient ∇p is the Lagrange multiplier ensuring incompressibility of the velocity field. The assumption of incompressibility is valid for dense suspensions. The free parameters $\lambda_0, \Gamma_0, \Gamma_2, \alpha$ and β can be chosen to match experimental results [13]. The parameter λ_0 is related to the type of the bacteria, i.e. whether they are of pusher or puller type. For pusher bacteria like *B. Subtilis*, $\lambda_0 > 1$. As discussed below, the number of parameters can be reduced by non-dimensionalizing the equations. The linear terms in the above equation select a range of scales that are excited to model the forcing in the bacterial flow, which occurs predominantly at small scales. In Fourier space, the linear part of the equation can be written as $\gamma(k)\tilde{\boldsymbol{u}}(\boldsymbol{k}, t) := (\Gamma_0 k^2 - \Gamma_2 k^4 - \alpha)\tilde{\boldsymbol{u}}(\boldsymbol{k}, t)$. Consequently, the excited modes correspond to the ones where $\gamma(k) > 0$. The nonlinear advective term, like in the Navier-Stokes equation, is responsible for the energy transfer and thus allows for the formation of large-scale structures. The cubic term is a nonlinear saturation which together with the squared Laplacian term ensures the regularity of these equations [113]. A detailed description of these equations can be found in refs. [26, 47].

For the current investigations, we non-dimensionalize the equations following ref. [105] and then normalize our numerical results based on dynamically emerging length and time scales. In summary, the procedure is as follows. The fastest growing linear mode $k_c = \sqrt{\Gamma_0/(2\Gamma_2)}$ is determined by the maximum of $\gamma(k)$. Consistent with ref. [105] we select a length scale $l = 5\pi/k_c$. A velocity scale can be defined dimensionally as $v_0 = \sqrt{\Gamma_0^3/\Gamma_2}$, which also selects a time-scale l/v_0. Non-dimensionalizing eq. (2.1) using this length scale and time scale reduces the two parameters Γ_0 and Γ_2 to constant numbers 0.045 and 9×10^{-5} respectively, thus decreasing the number of free parameters to three. If not noted otherwise, we choose the set of parameters $\lambda_0 = 3.5$, $\alpha = -1.0$ and $\beta = 0.5$, which already has been investigated in [105]. We normalize our numerical results with respect to the dominant length scale in the system. The wavenumber $k_{\max}$

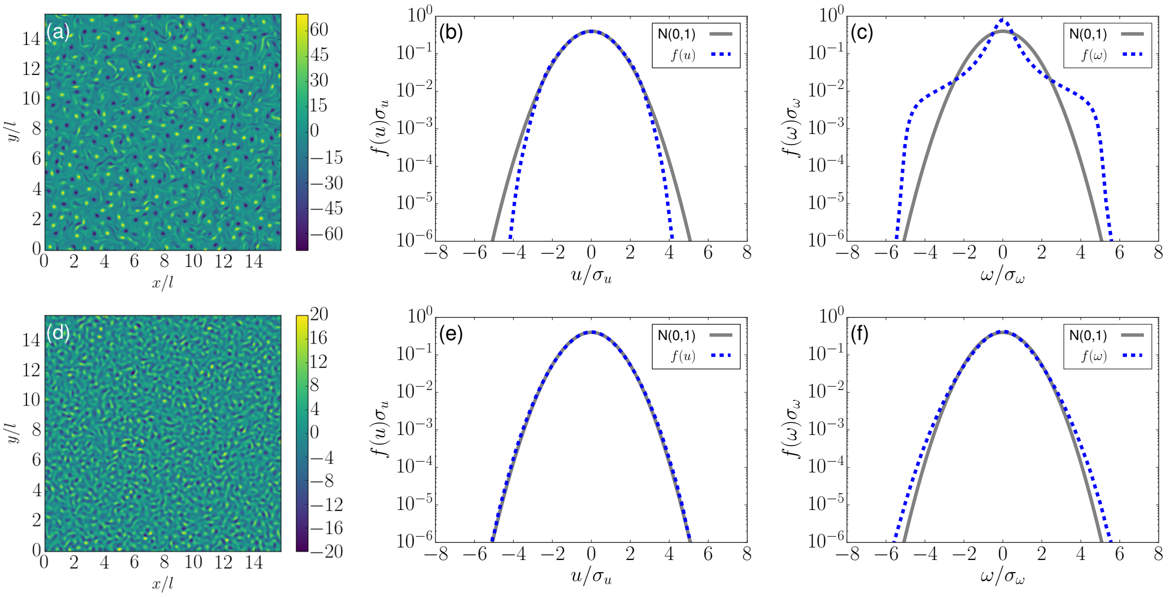

Figure 2.1: Upper row: active turbulence state with broad-band forcing ($\alpha = -1$). Panel (a) shows a snapshot of the vorticity field of active turbulence obtained through direct numerical simulation of eq. (2.1) with parameters chosen according to ref. [105]. Note that the vortices are approximately of the same size exemplifying the selection of a length scale in this system. The single-point velocity and vorticity distributions are shown in panels (b) and (c), respectively; σ_u and σ_ω are the standard deviations of the respective PDFs. The single-point velocity PDF is close to Gaussian, but has slightly sub-Gaussian tails. The vorticity PDF deviates considerably from Gaussian. Lower row: weakly excited case ($\alpha = 4$). Compared to the active turbulence case, the snapshot (d) shows less pronounced vortex structures. The single-point velocity and vorticity PDFs, (e) and (f), respectively, are very close to Gaussian.

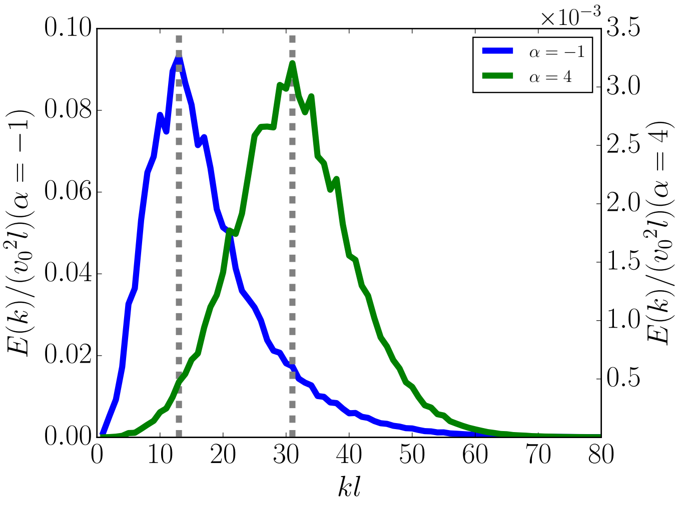

Figure 2.2: Energy spectra of the velocity field for the active turbulence case (blue) and the weakly excited case (green). The dashed vertical lines indicate the wavenumber corresponding to the dominant scale in the system. In the active turbulence case, the energy spectrum peaks at a much larger length scale (lower wavenumber) due to the formation of meso-scale vortices in the system as a result of the inverse energy transfer.

corresponding to the peak of the energy spectrum (see fig. 2.2) defines the dominant length scale in the system as $L = 2\pi/k_{\text{max}}$. This length scale can also be used to define a time scale given by $T = L/V$ where $V = \sqrt{\langle \boldsymbol{u}^2 \rangle}$. Such a procedure characterizes the significance of the dominant length scale in the system.

We numerically solve these equations in two dimensions by using a standard pseudo-spectral algorithm (with 1/2 dealiasing to account for the cubic nonlinearity) following a second-order Runge-Kutta scheme for time stepping with time step 0.0002. We choose a domain size of $5\pi \times 5\pi$ with 2048×2048 grid resolution.A large-scale flow is chosen as the initial condition. By testing different initial conditions, we ensured that the statistically stationary state is independent of the particular choices. For Lagrangian measurements, a million tracer particles are advected with the flow. The tracer particles are evolved according to the Lagrangian equations of motion $\mathrm{d}\boldsymbol{X}(\boldsymbol{x}_0, t)/\mathrm{d}t = \boldsymbol{u}(\boldsymbol{X}(\boldsymbol{x}_0, t), t)$, where $\boldsymbol{X}(\boldsymbol{x}_0, t)$ is the position of a tracer particle at time t starting from $\boldsymbol{x}_0$ at time t_0. The velocity $\boldsymbol{u}(\boldsymbol{X}(\boldsymbol{x}_0, t), t)$ at inter-grid points is interpolated by using a bicubic scheme. The system is allowed to evolve until it reaches a statistically stationary state after an approximate duration of $10T$ before measurements are taken. To identify and track vortex cores we follow an algorithm described in ref. [54], details of which are given in sect. 2.5.

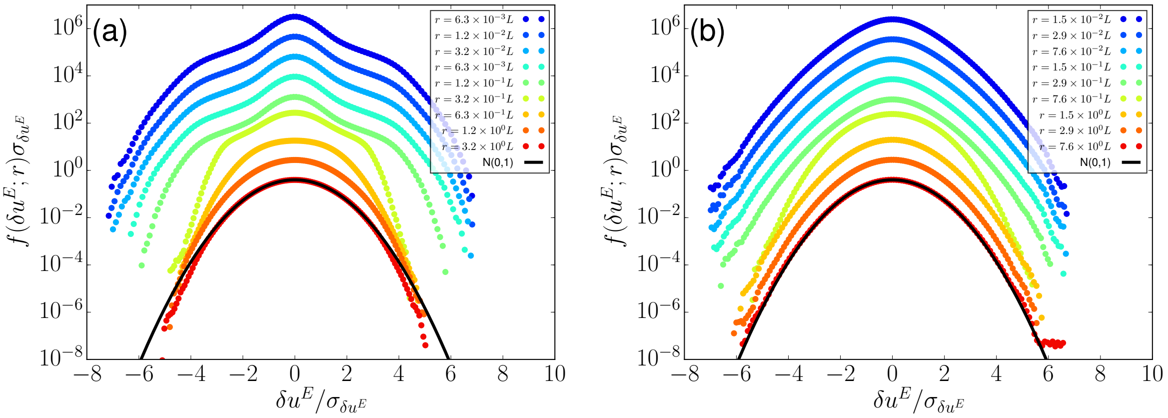

Figure 2.3: Eulerian longitudinal velocity increment PDFs for (a) the active turbulence case and (b) the weakly excited case. The small-scale increment PDF for the active turbulent case displays considerable deviations from Gaussianity. In comparison, the weakly excited case with less pronounced vortex structures shows a close-to-Gaussian behavior at all scales.

2.4 Eulerian statistics

To connect to previous work [13, 105] as well as to set a reference point for the subsequent investigation of Lagrangian properties of the flow, we start with characterizing the Eulerian statistics of active turbulence. Figure 2.1(b) shows the single-point velocity probability density function (PDF) of the active turbulence field. Since the flow is isotropic, we use one component of the velocity field to evaluate these PDFs. The distribution is close to Gaussian with sub-Gaussian tails. Sub-Gaussian tails for the single-point velocity have also been found for three-dimensional hydrodynamic turbulence [114]. The vorticity PDF, shown in fig. 2.1(c), departs strongly from Gaussianity with a comparably narrow core and wide tails, which roll off rapidly for large vorticity values. As is well known from the study of hydrodynamic turbulence, such departures from Gaussianity can be regarded as a signature of coherent vortex structures [115–117]. For example, they have also been observed in decaying two-dimensional Navier-Stokes turbulence [118].

The active turbulence model (2.1) gives precise control over the energy injection mechanism, which motivated us to further investigate the influence of active forcing on non-Gaussian features of the flow. For the active turbulence case with $\alpha = -1$, the linear terms represented through $\gamma(k)$ introduce an active broadband forcing which predominantly injects energy at the wavenumber k_c. This broadband forcing can be reduced to a narrow band of wavenumbers with a reduced energy input by increasing the damping rate. Here, we consider the case with $\alpha = 4$. The results of this numerical experiment are shown in the lower row of fig. 2.1. Figure 2.1(d) shows a snapshot of a vorticity field, which now displays less pronounced vortex structures compared to the active turbulence case. Still, the dynamics remains non-trivial as documented in the supplementary movie 2. The single-point velocity PDF shown in panel (e) is very close to Gaussian in the weakly excited case. Consistent with the observation of less pronounced vorticity structures, the vorticity PDF is now much closer to a Gaussian with slightly super-Gaussian tails.

To characterize multi-scale features of the flow, we obtain PDFs of the longitudinal velocity increments $\delta u^E = [\boldsymbol{u}(\boldsymbol{x}+\boldsymbol{r},t) - \boldsymbol{u}(\boldsymbol{x},t)] \cdot \hat{\boldsymbol{r}}$ for both cases as presented in fig. 2.3. Consistent with previously published results [13, 105] we find close-to-Gaussian PDFs from large to intermediate scales in the active turbulence case (panel (a)). Only at smaller scales on the order of L we find departures. This change from Gaussian to non-Gaussian statistics occurs rather abruptly in scale, and can be accounted to the presence of meso-scale vortices in the flow. Consistent with this picture, the weakly excited case shows a close-to-Gaussian statistics for all considered cases (panel (b)).

2.5 Vortex dynamics and Lagrangian transport properties

The results of the previous section have pointed out the significance of vortex structures, which is further investigated here, focusing on the vortex strength, dynamics and lifetimes. Some of these aspects are closely related to Lagrangian features of the flow, which are also analyzed in the following, where we restrict ourselves to the active turbulence case. In the previous section, we analyzed single-time statistical features of the active turbulence field from an Eulerian point of view. To further characterize the role of vortex structures, vortex cores are identified as the centers of the cells around which the velocity vector takes a full rotation [54]. To this end, we calculate the angle Λ which the velocity vector rotates around center point $\boldsymbol{x}$ of each cell, and vortex cores are defined as the centers of those cells where $\Lambda(\boldsymbol{x}) = \pm 2\pi$. This allows us to calculate vortex cores from the velocity field, although only with an accuracy of the grid resolution. Having identified the vortex cores, we are able to investigate their typical strength. Figure 2.4(a) shows the distribution of vorticity at vortex cores. From the distribution it is clear that there are predominantly two classes - weak and intense vortices. The intense vortices correspond to the ones clearly identifiable in fig. 2.1(a) whereas the weak ones correspond to less coherent, not necessarily axisymmetric vorticity patches. The observation of the distinct large-amplitude vortices explains the sharp roll-off of the PDF shown in fig. 2.1(c). Assuming a typical profile for vortex structures, the vorticity PDF can be thought of as a smeared-out version of the vortex-core strength PDF.

The distribution of vortex core lifetimes, shown in fig. 2.4(b), further clarifies the difference between weak and intense vortices. As can be inferred from the PDF, weak vortices typically have a much shorter lifetime than intense vortices. Also, the lifetime statistics for both weak and intense vortices decay to zero rather rapidly. We note that there are events in which an intense vortex transforms into a weak vortex and

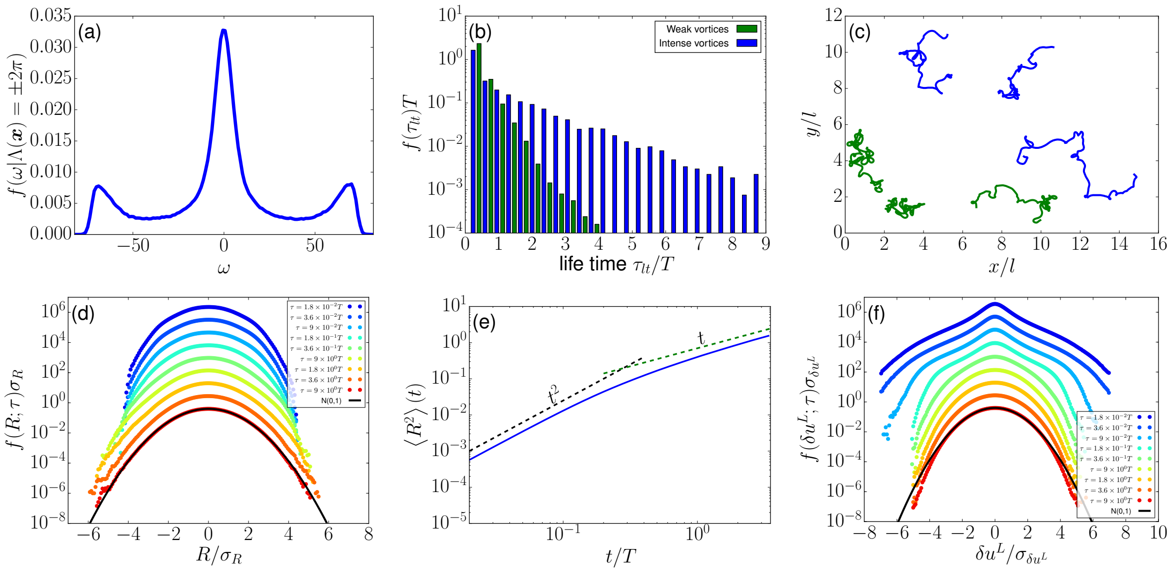

Figure 2.4: Upper row: statistics and dynamics of active matter vortices. Panel (a) shows the distribution of vorticity at vortex cores. The different peaks correspond to the vortices of the two classes - weak and intense. The distribution of vortex lifetimes for weak and intense vortices is shown in panel (b). Note that the intense vortices have on average longer lifetimes. Some sample vortex core trajectories are shown in panel (c) (in blue) along with some passive Lagrangian tracer particles (in green). Lower row: Lagrangian statistics of active turbulence. Panel (d) shows the single-particle dispersion PDF which is close to Gaussian for all time lags considered. The mean squared displacement, shown in panel (e), exhibits a cross-over from a ballistic to a diffusive regime. Lagrangian velocity increment distributions are shown in panel (f).

vice versa, which is one limiting factor of their lifetimes. Figure 2.4(c) shows some trajectories of vortices with long lifetimes along with some typical Lagrangian tracer trajectories. In comparison, the vortices appear to have smoother trajectories than the tracer particles. This is because the vortex core trajectories by design pick out very specific points in the flow field. In contrast to vortex cores, typical Lagrangian tracer particles encounter a number of vortex trapping events, which explains their rapid coiling. Similar observations have been made in two-dimensional turbulence [118, 119].

Proceeding to the characterization of Lagrangian statistics, fig. 2.4(d) shows standardized PDFs of Lagrangian single-particle dispersion, where R is one component of $\boldsymbol{X}(\boldsymbol{x}_0, t_0+\tau)-\boldsymbol{x}_0$. Owing to the approximate Gaussianity of the velocity, the PDFs are close to Gaussian for short time scales, and the Gaussianity persists up to the largest time scales, similar to what is found in hydrodynamic turbulence. The mean squared displacement, which characterizes the variance of this approximately self-similar process in scale, is shown in fig. 2.4(e). As expected, the displacement is initially ballistic, i.e. it scales as t^2, and then transitions to a diffusive long-time behavior with a scaling proportional to t. The transition occurs on the order of the time scale T which characterizes approximately the time spent by a tracer particle in a vortex.

Finally, we wish to characterize temporal velocity fluctuations along Lagrangian tracer particles. Figure 2.4(f) shows the distribution of Lagrangian velocity increments δu^L, defined as either of the components of $\boldsymbol{u}(\boldsymbol{X}(\boldsymbol{x}_0, t_0 + \tau), t_0 + \tau) - \boldsymbol{u}(\boldsymbol{x}_0, t_0)$, for different values of time lag τ. We observe that for short time scales, the statistics of the Lagrangian velocity increment shows strong deviations from Gaussianity, consistent with the observation for the Eulerian increments. In the limit of $\tau \to 0$ the velocity increment is proportional to the single-particle acceleration. Like in the Eulerian frame, the PDFs relax to a Gaussian shape rather sharply at a value of $\tau \approx T$, strengthening the hypothesis that the velocity field in active turbulence has a simple structure beyond the length scale of the individual strong vortices.

2.6 Summary and conclusions

In this work we have conducted a statistical study of a minimal continuum model for bacterial turbulence. The numerical and statistical results show that active turbulence displays close-to-Gaussian statistics both in an Eulerian and a Lagrangian frame when moderate to large scales are considered. Similar observations can be made in statistically stationary two-dimensional turbulence with large-scale friction. Deviations are found at the scale where coherent vortices occur, as can be probed with vorticity and velocity increment statistics. Employing a vortex identification and tracking algorithm, we find that active turbulence selects intense vortices of rather well-defined magnitude, which is in contrast to hydrodynamic turbulence. The life-time statistics of the vortices are investigated and display a rapid fall-off to zero. By increasing the damping rate compared to the active turbulence case, the emergence of meso-scale vortices is found to be suppressed, which goes along with statistics even closer to Gaussianity, corroborating the connection between non-Gaussian statistics and vortex structures.

The meso- to large-scale Gaussianity of active turbulence may open avenues for future analytical modeling approaches. A natural next step in the direction of this work is the development of a statistical theory of active turbulence, which is the subject of ongoing research.

3 Manuscript II: Turbulence and turbulent pattern formation in a minimal model for active fluids

This manuscript originally appeared as “James, M., Bos, W.J.T., & Wilczek, M. (2018). Turbulence and turbulent pattern formation in a minimal model for active fluids. Physical Review Fluids, 3(6), 061101.”. Supplementary videos are available at
DOI: 10.1103/PhysRevFluids.3.061101.

MW designed the research. MJ wrote the DNS code for the active fluids model, conducted the simulations and analyzed the data. WJTB conducted the closure analysis. All authors contributed to the interpretation of the results. MW wrote the manuscript with input from coauthors.

Turbulence and turbulent pattern formation in a minimal model for active fluids

3.1 Abstract

Active matter systems display a fascinating range of dynamical states, including stationary patterns and turbulent phases. While the former can be tackled with methods from the field of pattern formation, the spatio-temporal disorder of the active turbulence phase calls for a statistical description. Borrowing techniques from turbulence theory, we here establish a quantitative description of correlation functions and spectra of a minimal continuum model for active turbulence. Further exploring the parameter space, we also report on a surprising type of turbulence-driven pattern formation far beyond linear onset: the emergence of a dynamic hexagonal vortex lattice state after an extended turbulent transient, which can only be explained taking into account turbulent energy transfer across scales.

3.2 Introduction

Flows driven by active agents display a rich variety of dynamical states [1, 3, 120]. Active stresses and hydrodynamics collude to create collective motion, both regular and chaotic, in systems of motile micro-organisms [18, 121, 122] or artificial self-propelled agents [123, 124] on scales much larger than the individual. For example, sufficiently dense suspensions of motile micro-organisms, such as *B. Subtilis*, exhibit a spatio-temporally disordered phase. Owing to its reminiscence of hydrodynamic turbulence, this phenomenon has been termed active turbulence [13, 47, 105, 109, 125, 126]. Similar observations were also reported in systems dominated by nematic interactions such as ATP-driven microtubule networks [32]. Besides active turbulence, remarkably ordered phases were found in a number of systems. Self-organized vortex lattices, for example, have been discovered both in hydrodynamically interacting systems, such as spermatozoa [12], as well as in dry microtubule systems [16]. Confinement offers yet another possibility of organizing flows into regular large-scale flow [127] and vortex patterns [128].

The occurrence of these phenomena in vastly different systems has motivated the development and exploration of a range of minimal mathematical models. They can be broadly categorized into agent-based models of self-propelled particles with nematic or polar interactions [1, 10, 53, 129, 130] and continuum theories for a small number of order parameters [13, 26, 54, 111, 125]. These models have been shown to capture a variety of dynamical phases of active fluids, including active turbulence and vortex lattice states. For example, in [13] the active turbulence phase was modeled and compared with experiments. Regarding ordered phases, vortex lattices have been observed and investigated at the crossover from the hydrodynamic to the friction-dominated regimes of models for confined active fluids [57]. These systems display phases of two-signed vortices with length scales defined by the dimensions of the system. In a class of particle-based models for active matter, the emergence of vortex lattices has been related to a classical pattern formation mechanism as a result of a Turing instability [53, 129].

While many such models have been shown to capture the dynamics of active systems qualitatively and quantitatively, the complexity of disordered states like active turbulence eventually calls for a statistical description. The goal of such a non-equilibrium statistical mechanics of active matter is the computation of fundamental statistical quantities such as correlation functions without resorting to expensive numerical integration of systems with thousands or even millions of degrees of freedom.

Recent developments of statistical theories on top of minimal continuum theories for active matter have provided insights into the small-scale correlation structure of an active nematic fluid based on a mean field approach for the vorticity field [54], as well as a theory capturing large-scale features of polar bacterial flows based on analytical closure techniques [105]. A theoretical framework capturing the correlation function or equivalently the spectral properties for the full range of scales of such prototypical active systems, however, is currently lacking.

In this Rapid Communication, we set out to close this gap. Borrowing techniques from turbulence theory, we derive correlation functions and spectra of the turbulent phase of the minimal continuum theory recently established in [13] to capture the dynamics of dense bacterial suspensions. Further exploring the parameter space, we also discover a novel phase of turbulent pattern formation, i.e. an extensive turbulent transient governed by strong advection which eventually results in a highly ordered vortex lattice state. We demonstrate that turbulence characteristics crucially contribute to the emergence of this novel pattern through nonlinear advective energy transfer. This

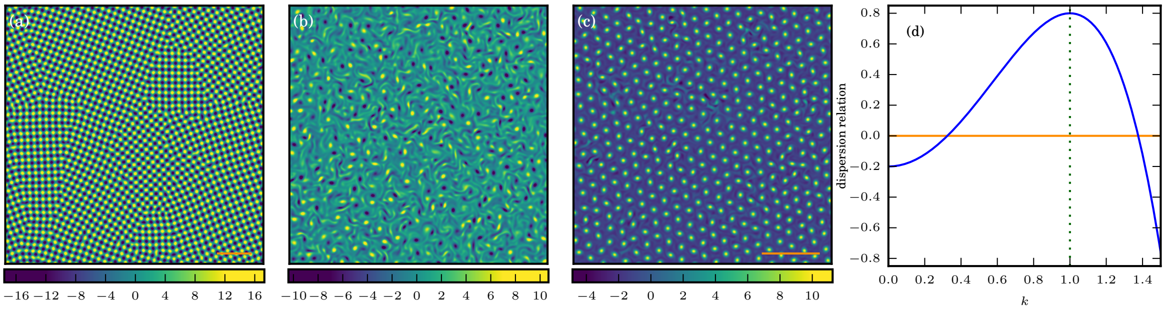

Figure 3.1: The continuum model Eq. (3.1) displays a range of dynamical phases of the vorticity field depending on the nonlinear advection: (a) classical pattern formation ($\lambda = 0$, simulation 1 in Table 3.1), (b) active turbulence ($\lambda = 3.5$, simulation 2 in Table 3.1) and (c) turbulent pattern formation ($\lambda = 7$, simulation 3 in Table 3.1). Notably, the dispersion relation shown in (d) along with the nonlinear damping is kept fixed for all examples. The dashed green line corresponds to the most unstable wave number, given by $k = k_c$, which sets the wave number of the pattern in (a). The horizontal orange lines in (a) and (c) correspond to five times the length scale of the patterns, i.e. $10\pi/k_c$ and $10\pi/k_0$, respectively, exemplifying that the wave number selection in the turbulent pattern forming phase (c) differs from the classical pattern forming phase (a).

mechanism differs profoundly from the classical route to pattern formation. To make this transparent, we first briefly recapitulate classical pattern formation in this minimal model for active fluids in absence of nonlinear advection.

3.2.1 Minimal Model for Active Fluids

The starting point is the equation for active turbulence as proposed in [13, 26] for a two-dimensional incompressible velocity field $\boldsymbol{u}(\boldsymbol{x}, t)$ describing the coarse-grained dynamics of a dense bacterial suspension. It takes the nondimensionalized form [1]

$$\partial_t \boldsymbol{u} + \lambda \boldsymbol{u} \cdot \nabla \boldsymbol{u} = -\nabla p - (1 + \Delta)^2 \boldsymbol{u} - \alpha \boldsymbol{u} - \beta \boldsymbol{u}^2\, \boldsymbol{u} \tag{3.1}$$

and represents a minimal field theory for a polar order parameter field, combining Navier-Stokes dynamics (advective nonlinearity and nonlocal pressure gradient) with elements of pattern forming systems (linear wave number selection and a saturating higher-order nonlinearity). Owing to its similarity to the Navier-Stokes equation, this minimal model is particularly suited to develop a statistical theory with methods from turbulence theory.

The dynamical phases of this continuum theory are explored in Fig. 3.1. Unless otherwise noted, we fix $\alpha = -0.8$ and $\beta = 0.01$ to focus on the role of nonlinear advection. The results are obtained numerically with a pseudo-spectral code using

---

[1] For the nondimensionalization we start from the equation presented in [13] and note that the term involving λ_1 can be absorbed into the pressure gradient term. Then we define the time scale $T = 4\Gamma_2/\Gamma_0^2$ and the length scale $L = \sqrt{-2\Gamma_2/\Gamma_0}$ to nondimensionalize the equation. To obtain Eq. (3.1), the parameters in the dimensional equation are mapped to the ones in the nondimensional equation according to $\lambda_0 \to \lambda$, $\Gamma_0 T/L^2 \to -2$, $\Gamma_2 T/L^4 \to 1$, $\alpha T \to \alpha + 1$ and $\beta L^2/T \to \beta$. We note that one additional parameter can be scaled out [131], which we refrain from here for presentation purposes.

No.	dynamical state	λ	α	β	N	D	Δt
1	square lattice	0	-0.8	0.01	2048	250	10^{-2}
2	active turbulence	3.5	-0.8	0.01	2048	250	10^{-3}
3	hexagonal lattice	7.0	-0.8	0.01	2048	250	10^{-3}
4	hexagonal lattice	7.0	-0.8	0.01	2048	125	10^{-3}
5	active turbulence	3.5	-0.3	0.01	2048	250	10^{-3}
6	benchmark case [132, 133]	3.5	-1.178	0.01125	2048	250	10^{-3}

Table 3.1: Simulation parameters. The active fluid is characterized through the parameters λ, α and β. The simulations are run on grids with N^2 grid points, discretizing a domain of lateral extent D; Δt denotes the time step.

a second-order Runge-Kutta scheme, and an integrating factor is used for treating the linear terms. More details on the simulations are provided in the supporting information. Table 3.1 lists the range of parameters explored in this manuscript.

3.2.2 Classical Pattern Formation

For $\lambda = 0$ the equation reduces to a vectorial Swift-Hohenberg type system which follows a gradient dynamics as discussed in the supporting information. In this parameter regime, we observe the emergence of stationary square lattices consistent with previous literature [26, 131]. Figure 3.1(a) shows a non-ideal square lattice with defects such as grain boundaries from our numerical simulations. As expected, the emergence of this state can be explained with tools from classical pattern formation theory in terms of amplitude equations. We analyze the corresponding amplitude equations [134] of the vorticity formulation of Eq. (3.1). The analysis detailed in the SI reveals the stability of the square lattice state with amplitude $A = \sqrt{-\alpha k_c^2/(5\beta)}$, which corresponds to a maximum value of the field of $4A$. In comparison, single-stripe patterns are linearly unstable. For the investigated parameters given in Table 3.1 the value of the theoretically predicted amplitude is 4.00, which is confirmed by our simulations to within 5 percent. This brief exposition serves to show that the classical pattern formation in absence of nonlinear advection leads to a stationary square lattice state with wave number $k_c = 1$.

3.3 Active Turbulence

As the advective term is switched on by setting $\lambda = 3.5$, the nonlinear energy transfer sets in, which by generating vortices of larger size renders the stationary square lattice pattern unstable. As a result, a self-sustained turbulence-like phase emerges (see Fig. 3.1(b)), which has been characterized, e.g. in [13, 105, 135]. Borrowing techniques from classical turbulence theory, we here establish a statistical description for the two-point correlation function and energy spectra for the full range of dynamically active scales.

To this end, we consider the velocity covariance tensor $R_{ij}(\boldsymbol{r}) = \langle u_i(\boldsymbol{x}, t)u_j(\boldsymbol{x} +$

$\boldsymbol{r}, t)\rangle \equiv \langle u_i u_j' \rangle$ which is among the most fundamental statistical objects of interest; by virtue of kinematic relations, it contains the correlation structure of the velocity field as well as of the vorticity and velocity gradient tensor fields [136]. Its evolution equation for the statistically homogeneous and isotropic turbulent phase is readily obtained as

$$\partial_t R_{ij} + \lambda \partial_k \langle u_k' u_i u_j' - u_k u_i u_j' \rangle = -2\left[(1+\Delta)^2 + \alpha\right] R_{ij} - \beta \langle u_k u_k u_i u_j' + u_k' u_k' u_i u_j' \rangle \,. \tag{3.2}$$

As a result of statistical isotropy, the pressure contribution vanishes. The quadratic and cubic nonlinearities result in unclosed terms which obstruct a direct computation of the covariance without making further assumptions. The main effect of the β-term is to saturate the velocity growth. Owing to the approximate Gaussianity of the velocity field [13, 47, 105, 135], the correlator in this term can be factorized using Wick's theorem, which yields $\langle u_k u_k u_i u_j' + u_k' u_k' u_i u_j' \rangle = 2R_{kk}(\mathbf{0}) R_{ij}(\boldsymbol{r}) + 2R_{ik}(\mathbf{0}) R_{kj}(\boldsymbol{r}) + 2R_{ik}(\boldsymbol{r}) R_{kj}(\mathbf{0})$.

An analogous attempt to factorize the triple correlators fails as this amounts to neglecting the energy transfer across scales, a hallmark feature of turbulence [137]. A more sophisticated closure needs to be established. For the subsequent treatment we choose a Fourier representation of the covariance tensor $R_{ij}(\boldsymbol{r})$ in terms of the spectral energy tensor $\Phi_{ij}(\boldsymbol{k})$. For a statistically isotropic two-dimensional flow, it takes the form $\Phi_{ij}(\boldsymbol{k}, t) = E(k,t)/(\pi k)\,[\delta_{ij} - k_i k_j / k^2]$, where $E(k,t)$ denotes the energy spectrum function. Starting from Eq. (3.2), an evolution equation for the energy spectrum function can be derived which takes the form [136–138]

$$\partial_t E(k,t) + T(k,t) = 2L(k,t) E(k,t) \,. \tag{3.3}$$

Here, $T(k,t)$ is the energy transfer term between different scales which results from the triple correlators in Eq. (3.2); $L(k,t) = -(1-k^2)^2 - \alpha - 4\beta E_0(t)$ is the *effective linear term*, which represents all linear terms as well as the Gaussian factorization of the cubic nonlinearity with $E_0(t) = \int E(k,t)\,\mathrm{d}k$. The effective linear term is responsible for the energy injection around $k_c = 1$ as well as for the damping at small and large scales. For the energy transfer term, we adopt the so-called eddy-damped quasi-normal Markovian (EDQNM) approximation and present here the main steps of the derivation for active fluids. More details are given in the SI. For a more comprehensive account of this model, which has been successfully applied to hydrodynamic turbulence, we refer the reader to [77, 139, 140]. The core idea of this closure scheme is to consider the evolution equation for the triple correlators in addition to Eq. (3.3), from which $T(k,t)$ can be obtained straightforwardly. The occurring fourth-order moments are then factorized assuming Gaussianity, similar to the treatment of the nonlinear damping term in Eq. (3.2), i.e. $\langle \hat{u}\hat{u}\hat{u}\hat{u} \rangle = \Sigma \langle \hat{u}\hat{u} \rangle \langle \hat{u}\hat{u} \rangle$ (written in a symbolic fashion). The influence of the neglected cumulants is modeled by an additional damping, which leads to an effective damping

η_{kpq} (see SI for more information). As a result we obtain an evolution equation for the triple correlators of the velocity modes $\boldsymbol{k}$, $\boldsymbol{p}$ and $\boldsymbol{q}$:

$$[\partial_t + \eta_{kpq}] \langle \hat{u}(\boldsymbol{k})\hat{u}(\boldsymbol{p})\hat{u}(\boldsymbol{q})\rangle = \lambda\Sigma\langle\hat{u}\hat{u}\rangle\langle\hat{u}\hat{u}\rangle. \tag{3.4}$$

As a next step, we apply the so-called Markovianization by assuming that the right-hand side evolves slowly, such that this equation can be integrated analytically and the steady state solution can be obtained by taking $t \to \infty$. The energy transfer function, which is a contraction of the triple velocity tensor, can then be written as

$$T(k,t) = \iint_\Delta \frac{\lambda^2}{\eta_{kpq}} \big[a(k,p,q)E(p,t)E(q,t) + b(k,p,q)E(q,t)E(k,t)\big]\,\mathrm{d}p\mathrm{d}q\,. \tag{3.5}$$

Here $1/\eta_{kpq}$ acts as a characteristic time scale which results from the turbulent damping. The geometric factors $a(k,p,q)$ and $b(k,p,q)$ are associated to contractions of the isotropic tensor $\langle \hat{u}(\boldsymbol{k})\hat{u}(\boldsymbol{p})\hat{u}(\boldsymbol{q})\rangle$; the exact expressions of the terms are given in the SI. Δ restricts the integration domain in p,q-space so that the three wave numbers k,p,q form the sides of a triangle. These triadic interactions are a direct consequence of the quadratic advective nonlinearity. While technically quite involved, the key feature is that the energy transfer term is expressed in terms of the energy spectrum only, i.e. we have obtained a closure. To illustrate the results, the left panel of Fig. 3.2 shows a comparison of the terms of Eq. (3.3) obtained from the EDQNM closure with a direct estimation from simulation data for active turbulence. Very good agreement is found for all wave numbers. Consistent with the observations in [105], the energy transfer term takes energy from the linear injection scale and transports it upscale. This inverse energy transfer is typical for two-dimensional flows [61]. Interpreting these results in the context of bacterial turbulence, the dominant energy injection occurs on a length scale comparable to the individual bacteria [13], yet their collective motion displays much larger scales. In the framework of the continuum model Eq. (3.1), this collective behavior is the result of an energy transfer to larger scales induced by nonlinear advection. The EDQNM theory captures this effect accurately. Also the effective linear term, which injects energy in a wave number band around $k_c = 1$, but extracts energy at large and small scales, is captured accurately, demonstrating the fidelity of the Gaussian factorization of nonlinear damping. The spectra resulting from the EDQNM closure are shown in the middle panel of Fig. 3.2. To demonstrate the validity of the closure theory for a broader parameter range, we additionally varied the α parameter (see Table 3.1). Furthermore, we also compare with the reference case reported in [13, 105], which in our normalized set of parameters corresponds to $\alpha = -1.178, \beta = 0.01125$. In previous literature, this reference case has been shown to capture experimental results [13]. As the value of α is decreased, the energy injection into the system becomes more intense

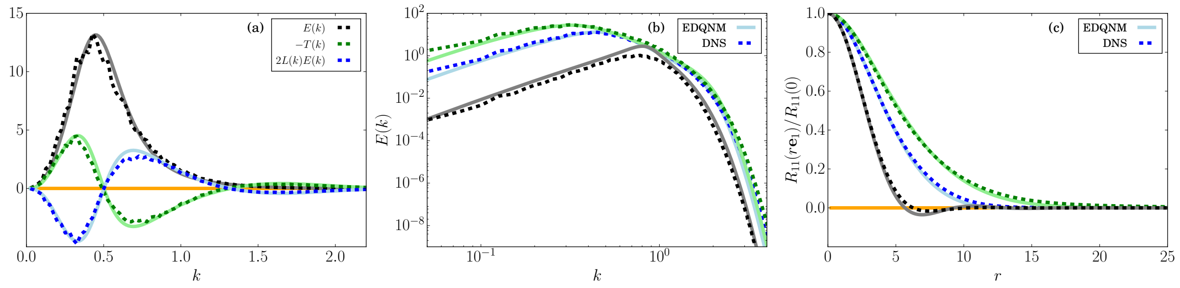

Figure 3.2: (a) Energy budget of active turbulence: direct numerical simulation (DNS) results (dashed lines, simulation 2 in Table 3.1) vs EDQNM closure theory. The black, green and blue curves correspond to the energy spectrum, the transfer term and the effective linear term, respectively. (b) Spectra from DNS of active turbulence compared to EDQNM closure theory. (c) Longitudinal velocity autocorrelation of active turbulence: DNS vs EDQNM closure theory. The blue, black and green curves in (b) and (c) correspond to the simulations 2, 5 and 6, respectively, as listed in Table 3.1.

and acts on a wider range of scales. As a result the energy spectra show an increased broadband excitation. Due to the inverse energy transfer the spectral peak gradually shifts from the most unstable wave number to smaller wave numbers, indicating the emergence of larger-scale flow structures. All of these trends are captured accurately by EDQNM without further adjustments. The EDQNM theory therefore extends the low-wave-number theory developed in [105] to the full range of scales. With the full energy spectra at hand, correlation functions can be computed in a straightforward manner. The results are shown in the right panel of Fig. 3.2. As the flow becomes increasingly turbulent, the correlation length increases. This can be understood from the previous observations in spectral space. Through the inverse energy transfer, larger-scale structures are excited leading to longer-range correlations. Again, EDQNM captures these observations accurately. These findings highlight the crucial impact of the nonlinear advection on the system and motivate the exploration of the dynamics in the parameter range of strong nonlinear advection.

3.4 Turbulent Pattern Formation

Further increasing the strength of the nonlinear advection to $\lambda = 7$ leads to a surprising new dynamical state emerging from a turbulent transient as visualized in Fig. 3.3. From random initial conditions vortices arise, triggered by small-scale instabilities. Many vortices are screened by surrounding vorticity of opposite sign, reducing their Biot-Savart interaction. Some of them, however, form dipoles, which propagate rapidly through the flow. These dipoles contribute significantly to the turbulent dynamics. In the course of time, a spontaneous symmetry breaking occurs, such that one sign of vorticity prevails. As a result, less dipoles form and the dynamics stabilizes. Repeating the numerical experiment with different random initial conditions confirms that both vorticity signs are equally probable in this spontaneous symmetry breaking. By the continued emergence

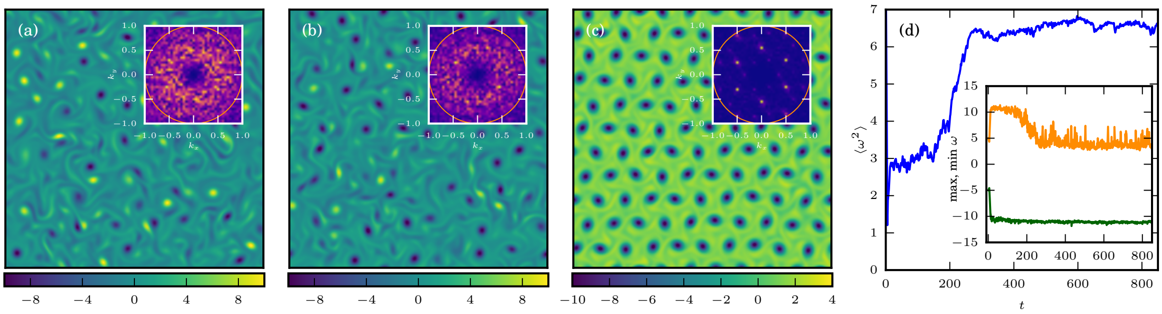

Figure 3.3: Emergence of hexagonal vortex lattice after a turbulent transient (simulation 4 in Table 3.1). (a,b,c): Vorticity field after $t = 20, 150, 850$. The insets show the two-dimensional vorticity spectra with the wave vectors corresponding to the most unstable wave number indicated by an orange circle. The inset (c) clearly shows six isolated peaks at $k_0 \approx 0.57$ which characterize the vortex lattice. For visualization purposes, these figures were obtained through a simulation on a smaller domain with half the domain length compared to Fig. 3.1. Note that the final vortex crystal state selects a sign of vorticity different from that of Fig. 3.1, exemplifying spontaneous symmetry breaking in this system. Panel (d) shows the evolution of the enstrophy, as well as the maximum and the minimum vorticity through the transient to the final quasi-stationary state.

of vortices the system eventually crystallizes into a quasi-stationary hexagonal vortex lattice state. The wave number characterizing this turbulent pattern is significantly smaller than naïvely expected based on the linear critical wave number $k_c = 1$ in the classical pattern formation case. This can be explained as follows: as the turbulent pattern emerges out of a turbulent transient, there is an inverse transfer of energy feeding larger scales. As a result, the peak energy injection scale in Eq. (3.3) (i.e. the maximum of $2L(k,t)E(k,t) - T(k,t)$) shifts to smaller wave numbers during the transient, giving rise to larger-scale flow structures. Because $\int T(k,t)\mathrm{d}k = 0$ by virtue of $T(k,t)$ being an energy transfer term, Eq. (3.3) implies the constraint $\int L(k,t)E(k,t)\mathrm{d}k = 0$ once the statistically stationary state with the vortex lattice is reached. Given the fact that the system forms a regular vortex pattern with a sharply localized spectrum around the lattice wave number, this constraint can only be satisfied if the lattice wave number k_0 is close to the zero-crossing of the effective linear term, i.e. close to the wave number corresponding to the smallest neutral mode. For the current choice of parameters, this prediction yields $k_0 \approx 0.58$ in very good agreement with the numerical observation ($k_0 \approx 0.57$). To further confirm this prediction, we scanned the entire α-range $[-0.95, -0.75]$ leading to stable vortex lattices, keeping all other parameters fixed. We observed a trend of the lattice wave number slowly increasing with α, which is captured by the prediction to within ten percent (not shown). We conclude that this turbulent pattern formation selects the *neutral* mode rather than the fastest growing linear mode. We stress that this mechanism profoundly differs from the Turing mechanism reported in [53, 129] due to the extended turbulent transient leading to the selection of the neutral mode.

It remains to explain the type of lattice. Nonlinear advection favors axisymmetric vortices. As these structures populate the domain over time, they form the densest possible packing consistent with this geometry, resulting in the hexagonal pattern. Unlike the case of classical pattern formation ($\lambda = 0$), this vortex lattice is quasi-stationary with perturbations from weaker background turbulence. The most striking feature of this phenomenon is the long turbulent transient phase preceding the formation of the pattern, which lasts much longer than the typical lifetimes of the vortices in the turbulent phase. Furthermore, unlike classical pattern formation, the dominant length scale in the system is given by the neutral mode in the effective dispersion relation.

3.5 Conclusions

The correlation functions and spectra of a minimal model for active turbulence developed in this paper establish a quantitative statistical theory of active turbulence. We adapted the EDQNM closure scheme for classical hydrodynamic turbulence to capture the linear driving and damping as well as the nonlinear energy transfer across scales along with nonlinear damping. For the range of investigated parameters, the theory has been found to accurately capture simulation results. It revealed that the spectral peak, associated with the typical size of turbulent flow structures, originates from the interplay of linear and nonlinear physics: energy is injected in a band of unstable modes which then cascades uphill before dissipated by linear and nonlinear damping terms. EDQNM therefore quantitatively captures the statistics of the collective behavior emerging in the continuum model Eq. (3.1). Having demonstrated the potential of methods from turbulence theory to capture disordered active matter states, we hope that our findings may spur further research. For instance, a generalization to active nematics might be an interesting direction for future research.

Further exploring the parameter space towards strong nonlinear advection, we find a highly ordered lattice state of dynamically self-organized vortices which emerges from an extensive turbulent transient. The inverse energy transfer of two-dimensional turbulence turns out to be a crucial ingredient in this turbulent pattern formation: the same mechanism leading to the spectral peak in the turbulent phase selects the neutral wave number in this turbulent pattern formation. While the potential importance of neutral modes has been pointed out in [141] based on kinematic considerations, our findings show that they are indeed dynamically relevant.

Regarding possible experimental realizations of the vortex lattice state reported here, we note that we observe it in a regime of strong nonlinear advection due to active stresses. Recent research has indicated that such a regime, in which the value of λ is large, can be achieved by a microstate with strong polar interaction among the active particles [98]. Furthermore, we observe the vortex lattice in a parameter range (controlled by α) of both large- and small-scale damping. Thus experiments involving active fluids with strong polar interactions and with substrate-mediated friction could potentially realize this novel “turbulent pattern formation” phenomenon.

Interestingly, the mechanism reported here shares similarity with quasicrystalline vortex lattices in drift-wave turbulence [142], although their vortex pattern appear less stable than the ones reported here. Vortex crystals have also been observed in two-dimensional Navier-Stokes turbulence driven by a combination of deterministic and stochastic forcings [143], in truncated two-dimensional turbulence [144], in simulations of quasi-geostrophic turbulence [145] as well as in two-dimensional fluid films with polymer additives [146]. Furthermore, vortex lattices have been predicted [147] and observed [148] in superconductors. These observations in profoundly different physical systems point at the ostensibly universal occurrence of highly ordered states in strongly nonlinear regimes. The investigation of this phenomenon in generic systems which combine features of pattern formation with non-Lyapunov dynamics such as nonlinear advection appears as one exciting direction for future research.

3.6 Supporting Information

3.6.1 Numerical Simulations

The numerical simulations are performed with a standard pseudospectral scheme for the vorticity formulation of Eq. (3.1):

$$\partial_t \omega + \lambda \boldsymbol{u} \cdot \boldsymbol{\nabla} \omega = -(1+\Delta)^2 \omega - \alpha \omega - \beta \, \boldsymbol{\nabla} \times \left(\boldsymbol{u}^2 \, \boldsymbol{u} \right) \, . \tag{3.6}$$

Here $\omega(\boldsymbol{x},t) = \boldsymbol{\nabla} \times \boldsymbol{u}(\boldsymbol{x},t)$ is the pseudo-scalar vorticity. In turn, the velocity is obtained from the vorticity by Biot-Savart’s law. An equation for the spatially constant velocity contribution u_0, which is not contained in the vorticity field, is integrated simultaneously. Time stepping is performed by means of a second-order Runge-Kutta scheme, in which the linear term is treated with an integrating factor. To account for the cubic nonlinearity, the pseudospectral scheme is fully dealiased with a 1/2 dealiasing. Small-scale, low-amplitude random initial conditions are chosen for all simulations. The parameters for the various simulations are summarized in Table 3.1.

3.6.2 Classical pattern formation – square lattice state

For $\lambda = 0$, Eq. (3.1) follows a gradient dynamics constrained to the sub-space of incompressible velocity fields, $\partial_t \boldsymbol{u} = -\boldsymbol{\nabla} p - \delta \mathcal{L}[\boldsymbol{u}]/\delta \boldsymbol{u}$. Here, all terms except the pressure gradient can be combined into the Lyapunov functional (see also [149, 150])

$$\mathcal{L}[\boldsymbol{u}] = \int d\boldsymbol{x} \left[(\Delta \boldsymbol{u} + \boldsymbol{u})^2/2 + \alpha \boldsymbol{u}^2/2 + \beta \left(\boldsymbol{u}^2 \right)^2/4 \right] ; \tag{3.7}$$

the pressure gradient term is a Lagrange multiplier to ensure $\boldsymbol{\nabla} \cdot \boldsymbol{u} = 0$. As a result of the potential dynamics, a stationary pattern emerges; its wave number $k_c = 1$ is straightforwardly computed by linear stability analysis.

The pattern forming state can be conveniently analyzed in the vorticity formulation Eq. (3.6). Motivated by our numerical observations, we investigate a lattice state of the form

$$\omega(\boldsymbol{x}, t) = \zeta_1(t) \exp[\mathrm{i}\boldsymbol{k}_1 \cdot \boldsymbol{x}] + \zeta_2(t) \exp[\mathrm{i}\boldsymbol{k}_2 \cdot \boldsymbol{x}] + \text{c.c.} \tag{3.8}$$

with $|\boldsymbol{k}_1| = |\boldsymbol{k}_2| = k_c = 1$, $\boldsymbol{k}_1 \cdot \boldsymbol{k}_2 / k_c^2 = \cos\varphi$ and amplitudes ζ_1 and ζ_2, which we can choose as real due to translational invariance. Combining this ansatz with the full nonlinear equations, amplitude equations can be straightforwardly derived, which in leading order take the form

$$\dot{\zeta}_1 = -\alpha\zeta_1 - \frac{\beta}{k_c^2}\left(3\zeta_1^3 + 2\left[1 + 2\cos^2\varphi\right]\zeta_2^2\zeta_1\right) \tag{3.9}$$

$$\dot{\zeta}_2 = -\alpha\zeta_2 - \frac{\beta}{k_c^2}\left(3\zeta_2^3 + 2\left[1 + 2\cos^2\varphi\right]\zeta_1^2\zeta_2\right) . \tag{3.10}$$

These equations can be further analyzed by means of a linear stability analysis. The analysis shows that the ground state $\zeta_1 = \zeta_2 = 0$ is linearly unstable for $\alpha < 0$ with growth rates $\lambda_{1,2}^{(0)} = -\alpha$. For a single-stripe pattern with $\zeta_2 = 0$ the amplitude equations yield $\zeta_1 = \sqrt{-\alpha k_c^2/(3\beta)}$ as a stationary solution. A linear stability analysis with small perturbation of the single-stripe pattern yields growth rates $\lambda_1^{(1)} = 2\alpha$ and $\lambda_2^{(1)} = \alpha\left[4\cos^2\varphi - 1\right]/3$ (see Fig. 3.4). As expected, small perturbations in the direction of the single stripe are damped for $\alpha < 0$. The emergence of a second stripe, however, is linearly unstable for a small wave number band around $\varphi = \pi/2$, which gives a first hint at the emergence of a square lattice. This can be further corroborated with a linear stability analysis of a lattice state with $\zeta_1 = \zeta_2$, for which the stationary solution $\zeta_1 = \zeta_2 = \sqrt{\frac{-\alpha k_c^2}{\beta[5+4\cos^2\varphi]}}$ is readily obtained from the amplitude equations. Linear stability analysis, assuming small perturbations in both amplitudes, yields $\lambda_1^{(2)} = 2\alpha$ and $\lambda_2^{(2)} = 2\alpha\frac{1-4\cos^2\varphi}{5+4\cos^2\varphi}$. For $\alpha < 0$ a range of lattice states is linearly stable with the maximum stability reached when $\varphi = \pi/2$ (see Fig. 3.4). This analysis renders a clear picture of the emergence of square lattice states for $\alpha < 0$: the single-stripe pattern is unstable with respect to the emergence of a two-stripe lattice with the maximum growth rate at $\varphi = \pi/2$. The resulting square lattice state with $\zeta_1 = \zeta_2 = \sqrt{-\alpha k_c^2/(5\beta)}$ then is linearly stable. Minimizing the Lyapunov functional for a square lattice with respect to the amplitude yields the same result.

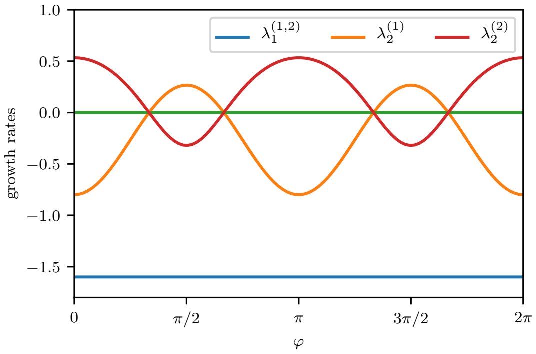

Figure 3.4: Growth rates of the linear stability analysis for $\alpha = -0.8$. The eigenvalues $\lambda_1^{(1,2)}$ correspond to the stable eigenvalues of the single- and two-stripe pattern, respectively. Starting from a single-stripe pattern, $\lambda_2^{(1)}$ indicates that a second stripe in a wave-number band around $\pi/2$ can be excited. The eigenvalue $\lambda_2^{(2)}$ shows that the square lattice state is linearly stable.

3.6.3 Active turbulence – EDQNM closure

Developing a statistical theory for the turbulent phase of active fluids requires assumptions about the hierarchy of moments. Indeed, the equation for the covariance tensor Eq. (3.2), or equivalently, for the energy spectrum Eq. (3.3), is unclosed due to the presence of the higher-order velocity correlations stemming from the nonlinear terms.

To set our theoretical development into context, we start with re-iterating the classical closure attempts in the context of the active turbulence equations. The classical closure theory is presented in much more detail in [77, 139, 140]. A Gaussian approximation is the simplest first choice to close the system, in particular in a random system like turbulence. Under this cumulant discard hypothesis, one can factorize higher-order moments in terms of corresponding second-order moments. This allows us to close the fourth-order term in Eq. (3.2) as described in the main text. However, the third-order correlations in Eq. (3.3) vanish under such a Gaussian approximation. The third-order correlations are responsible for the energy transfer between scales and hence are essential for the dynamics. A logical step towards closure is to write then the equations for the triple correlation, which in Fourier space take the form

$$\left[\partial_t + \tilde{L}(k) + \tilde{L}(p) + \tilde{L}(q)\right] \langle \hat{u}(\boldsymbol{k})\hat{u}(\boldsymbol{p})\hat{u}(\boldsymbol{q})\rangle = F[\lambda\langle \hat{u}\hat{u}\hat{u}\hat{u}\rangle, \beta\langle \hat{u}\hat{u}\hat{u}\hat{u}\hat{u}\rangle]\,. \tag{3.11}$$

In favor of a lighter notation we write these equations rather schematically, suppressing tensorial notation. Here, $\tilde{L}(k) = (1-k^2)^2 + \alpha$, and the functional F captures the contributions due to the pressure term as well as the fourth- and the fifth-order correlations which appear due to the advective and cubic nonlinearities in Eq. (3.1), respectively. To close this system on the level of the quadruple and fifth-order correlations, one can now assume a Gaussian factorization of these higher-order moments as the next simplest closure. This eliminates the fifth-order correlations and the fourth-order correlation can now be written in terms of second-order correlations resulting in

$$\left[\partial_t + \tilde{L}(k) + \tilde{L}(p) + \tilde{L}(q)\right] \langle \hat{u}(\boldsymbol{k})\hat{u}(\boldsymbol{p})\hat{u}(\boldsymbol{q})\rangle = \lambda\Sigma\langle\hat{u}\hat{u}\rangle\langle\hat{u}\hat{u}\rangle \tag{3.12}$$

so that the Eq. (3.3) for the energy spectrum $E(k)$ is now closed. This procedure is known as the quasi-normal approximation [71, 75]. This classical approximation for the energy transfer term has been shown to fail spectacularly for hydrodynamic turbulence already in the 1960s [70], leading to a realizability problem by the development of negative energies, since the omission of the cumulants leads to an overprediction of the transfer term.

To remedy this shortcoming, more sophisticated manners of closure were proposed, in particular by Kraichnan [151, 152], using renormalized perturbation theories. The simplest successful derivative of these theories is the eddy-damped quasi-normal Markovian model [76]. For an extensive account on the matter, we refer to [77, 139, 140]. Here we adopt this framework to formulate a statistical theory for active turbulence. The eddy-damped quasi-normal Markovian model generalizes the classical quasi-normal approximation by modeling the effect of the missing fourth-order cumulants as $\lambda(\langle\hat{u}\hat{u}\hat{u}\hat{u}\rangle - \Sigma\langle\hat{u}\hat{u}\rangle\langle\hat{u}\hat{u}\rangle) = -\mu_{kpq}\langle\hat{u}(\boldsymbol{k})\hat{u}(\boldsymbol{p})\hat{u}(\boldsymbol{q})\rangle$ where the damping term $\mu_{kpq} = \mu_k + \mu_p + \mu_q$ is defined through the contributions

$$\mu_k = \lambda\gamma\left(\int_0^k s^2 E(s,t)ds\right)^{1/2} . \tag{3.13}$$

Here, γ is a free parameter which quantifies the strength of the eddy damping. We can then combine the linear terms to define $\eta_k = \mu_k + |\tilde{L}(k)|$ as the net damping. The damping of the triple correlation corresponds to the Lagrangian decorrelation of the Fourier modes [153], and both the positive and the negative linear terms will lead to an effective decorrelation. Consequently the effect of $\tilde{L}(k)$ in damping should be strictly positive, and hence we take the absolute value of $\tilde{L}(k)$. With this assumption, the evolution equation for the triple correlation can be written as

$$\left[\partial_t + \eta_{kpq}\right]\langle\hat{u}(\boldsymbol{k})\hat{u}(\boldsymbol{p})\hat{u}(\boldsymbol{q})\rangle = \lambda\Sigma\langle\hat{u}\hat{u}\rangle\langle\hat{u}\hat{u}\rangle, \tag{3.14}$$

where $\eta_{kpq} = \eta_k + \eta_p + \eta_q$. If we neglect the time variation in μ_k and $\langle\hat{u}\hat{u}\rangle\langle\hat{u}\hat{u}\rangle$, the above expression can be integrated in time, resulting in the following expression for the triple correlation in terms of the energy spectrum:

$$\langle \hat{u}(\boldsymbol{k})\hat{u}(\boldsymbol{p})\hat{u}(\boldsymbol{q})\rangle(t) = \frac{1 - e^{-\eta_{kpq}t}}{\eta_{kpq}} \lambda\Sigma\langle\hat{u}\hat{u}\rangle\langle\hat{u}\hat{u}\rangle. \tag{3.15}$$

For large time scales, $e^{-\eta_{kpq}t}$ can be neglected, and $1/\eta_{kpq}$ defines a characteristic time. This timescale is associated with the Lagrangian correlation time of the fluid particles (see for instance [153] for a discussion). The second-order correlations are associated with the energy spectrum, hence Eq. (3.3) and Eq. (3.15) together result in a closed set of equations for the evolution of the energy spectrum. Owing to the isotropy of the velocity field, $T(k)$ in Eq. (3.3) can be calculated from $\langle \hat{u}_l(\boldsymbol{k})\hat{u}_m(\boldsymbol{p})\hat{u}_n(\boldsymbol{q})\rangle \equiv T_{lmn}(\boldsymbol{k}, \boldsymbol{p}, \boldsymbol{q})$ (in full tensorial notation) as

$$T(k) = \pi k P_{lmn}(\boldsymbol{k}) \int \mathrm{Im}\left[T_{lmn}(\boldsymbol{k}, \boldsymbol{p}, \boldsymbol{q})\right] d\boldsymbol{p}d\boldsymbol{q}\,, \tag{3.16}$$

where $P_{lmn}(\boldsymbol{k}) = k_n(\delta_{lm} - k_l k_m/k^2) + k_m(\delta_{ln} - k_l k_n/k^2)$ and Im stands for the imaginary part. The integration is performed over all triads $\boldsymbol{k}, \boldsymbol{p}, \boldsymbol{q}$ where $\boldsymbol{k} + \boldsymbol{p} + \boldsymbol{q} = 0$. The final expression for $T(k, t)$ can then be written as [72]

$$T(k,t) = -\frac{4}{\pi} \iint_{\Delta} \frac{\lambda^2}{\eta_{kpq}} \frac{xy - z + 2z^3}{\sqrt{1 - x^2}} \left[k^2 p E(p,t) E(q,t) - k p^2 E(q,t) E(k,t)\right] \frac{dpdq}{pq}\,. \tag{3.17}$$

Here Δ is a band in p, q-space so that the three wave numbers k, p, q form the sides of a triangle. x, y, z are the cosines of the angles opposite to the sides k, p, q in this triangle. Comparing Eq. (3.17) with Eq. (3.5), we obtain $a(k, p, q) = -\frac{4}{\pi} \frac{xy - z + 2z^3}{\sqrt{1-x^2}} \frac{k^2}{q}$ and $b(k, p, q) = \frac{4}{\pi} \frac{xy - z + 2z^3}{\sqrt{1-x^2}} \frac{kp}{q}$.

To generate the results presented in the main text, this closed set of equations for the energy spectrum function is integrated numerically. Computations are carried out on a logarithmically spaced mesh on the interval $0.025 \le k \le 25$ using 300 modes. All results are obtained, using $\gamma = 0.55$, after the spectrum reached a steady state.

4 Manuscript III: Melting of active vortex crystals

The contents of this chapter is a draft manuscript by M. James, D.A. Suchla, J. Dunkel and M. Wilczek.

MJ and DAS are joint first authors. MJ and MW designed the research. DAS wrote the DNS code. DAS and MJ conducted the simulations and analyzed the data. All authors contributed to the interpretation of the results. MJ and MW wrote the manuscript with input from coauthors.

Melting of active vortex crystals

4.1 Abstract

Two-dimensional equilibrium crystals exhibit a complex melting scenario, in which the fluid phase may be reached through an intermediate hexatic phase characterized by the loss of long-range orientational order. For nonequilibrium active matter systems, much less is known about the corresponding phase transition. Here, we study the emergence of self-organized vortex crystals in a two-dimensional active matter system by using a generic minimal continuum theory. We characterize the melting of this "active vortex crystal" into a turbulent active fluid through an extensive computational study. We report on two different melting scenarios; a discontinuous transition that proceeds through a hysteretic phase as well as a melting process with an intermediate hexatic phase. In the thermodynamic limit, we find universal transient features characterized by meta-stable superstructures of vortex crystal domains of spins with opposite polarity. Our results establish close analogies between crystalline phases in active matter and their equilibrium counterparts.

4.2 Introduction

Two-dimensional crystals have played a distinct role in understanding order in equilibrium systems. While they exhibit orientational order, it was shown that long-range positional order is suppressed at finite temperatures [6–8]. Melting of two-dimensional crystals, in particular, continues to raise considerable interest, as multiple competing theories on the type and nature of the transition have been proposed [78]. A first-order transition is predicted by the density-functional theory [87] and the grain-boundary induced melting theory [88], whereas the Kosterlitz, Thouless, Halperin, Nelson, and Young (KTHNY) theory [85] predicts a two-step continuous melting transition. According to the KTHNY theory, the melting proceeds through an intermediate hexatic phase with quasi-long-range orientational order, but short-ranged positional order, as observed in experiments on colloidal systems [84], supercurrent lattices [154] as well as in numerical simulations of repulsive disks [155]. Given the complexity and richness of two-dimensional melting in equilibrium systems, it remains a fundamental question to which extent these phenomena translate to nonequilibrium systems.

Indeed, there are indications that out-of-equilibrium crystal phases and their melting transitions share close analogies to equilibrium crystals [89–91]. For instance, the melting of an out-of-equilibrium two-dimensional system of ferrofluid spikes has been shown to proceed with an intermediate hexatic phase [89]. In active matter, crystalline-like phases have been observed in a variety of systems ranging from active colloids [15, 92, 156] to bacterial and dense cell suspensions [1, 93, 157]. The formation of these active crystals is mediated by clustering of active particles resulting in an ordered solid-like state. Their properties have been studied by using both self-propelled particle (SPP) models [94, 158–163] and field theories [95, 164]. Vortex crystals form yet another paradigmatic class of active crystals with several distinct features. Unlike particles, vortices are emergent constituents which can be created or annihilated. As vortices of both positive or negative polarity exist, the formation of a vortex crystal may involve a discrete symmetry breaking in which one vortex polarity prevails. Experimental works on spermatozoa [12] and microtubule systems [16] have reported on symmetry-broken states of both regular and irregular arrays of vortices in active systems. Spermatozoa suspensions, in particular, self-organize into a well-ordered hexagonal vortex array under suitable conditions [12]. While the properties of smaller vortex arrays have been probed by using SPP models [41, 53], a profound analysis of melting of nonequilibrium vortex crystals in active matter requires large system sizes, which only recently have become computationally accessible.

Here, we study the spontaneous emergence of active vortex crystals (AVCs) as well as their melting in a minimal continuum model. This model can be perceived as a variant of the Toner-Tu equations for active matter [11, 23], which has previously been instrumental in investigating the properties of turbulent phase in active fluids [13, 105] and allowed to uncover the emergence of a symmetry-broken vortex crystal phase [165]. By performing a detailed computational analysis at an unprecedented scale, we here characterize the emergence and melting of AVCs. We find a rich range of transition phenomena including an intermediate hexatic phase as well as hysteretic liquid-crystal phase coexistence. As we approach the thermodynamic limit, we observe a supertransient phase of coexisting AVCs of opposite polarity. In the following, by using massive computational simulations, we systematically characterize this melting of AVCs into a turbulent active fluid.

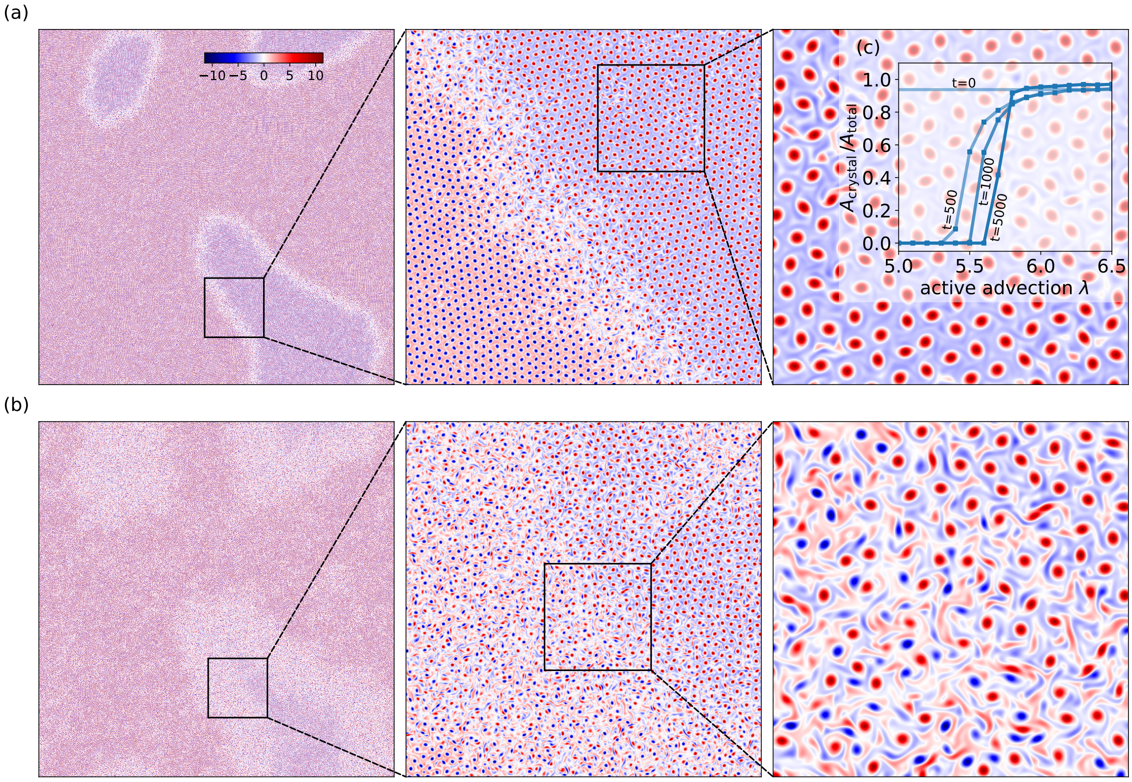

Figure 4.1: Melting of AVC superstructures: (a) A metastable superstructure of opposite-polarity crystal domains obtained through a simulation on a $1000\pi \times 1000\pi$ domain resolved with 8192×8192 grid points ($\lambda = 7$, $\alpha = -0.8$). The zoom-ins show domains of opposite polarity demarcated by a boundary layer of active fluid. (b) A snapshot of the superstructure after time $t = 800$ as it melts at a reduced value of active advection ($\lambda = 5.6$). Notice how the active fluid boundary layer between the crystal domains has spread in area. (c) Area fraction of the crystal domains as a function of active advection for different times, starting from the superstructure (a) at time $t = 0$. Note that the width of the domain boundaries in the transient superstructures is controlled by the strength of the active advection.

4.3 Results

4.3.1 Minimal continuum model

Our starting point is an incompressible version of the Toner-Tu equations [11, 23], with the active fluid velocity $\boldsymbol{u}$ as the only order parameter field [13, 26, 105]:

$$\begin{aligned} \partial_t \boldsymbol{u} + \lambda \boldsymbol{u} \cdot \nabla \boldsymbol{u} &= -\nabla p - (1+\Delta)^2 \boldsymbol{u} - (\alpha + \beta |\boldsymbol{u}|^2) \boldsymbol{u}, \\ \nabla \cdot \boldsymbol{u} &= 0. \end{aligned} \tag{4.1}$$

Here p is the pressure term, λ is an active advection parameter which incorporates the effects of active stresses [26], and α is the activity parameter which is related to the self-propulsion velocity (the parameter β can be scaled out and is kept for numerical convenience). Eq. (4.1) is self driven (due to the instability introduced by the linear Swift-Hohenberg operator) and has no external noise. The resulting model can be thought of as a minimal continuum theory for active fluids [26], which combines the self-propulsion of the active particles and their hydrodynamic and steric interactions into one phenomenological order parameter equation. The statistical properties of this theory have been favorably compared to the active turbulence phase [13]. Furthermore, it has been shown that these equations can be derived from microscopic considerations for bacterial systems [97, 98]. Here, we present results from direct numerical simulation of the equations of motion in a periodic domain by using a pseudo-spectral method for the spatial discretization and a fourth-order Runge-Kutta scheme for time stepping (Methods).

4.3.2 Large-scale active vortex crystals

As an illustration of the active vortex crystals emerging in our system, Fig. 4.1 (a) shows the vorticity field for a simulation on a $1000\pi \times 1000\pi$ domain resolved with 8192^2 grid points. At this very large system size, the system features AVC superstructures, i.e. crystal domains of opposite polarity. The domain boundaries are comprised of active turbulence regions. These highly dynamic domain boundaries also play a prominent role in the AVC melting, which can be induced, for example, by decreasing the active advection parameter. As active advection is decreased, the superstructures melt, and the turbulent boundary layers spread in area, destroying the crystal structure (Fig. 4.1 (b)). Since the AVC superstructures are formed by crystal domains demarcated by an active fluid boundary layer, a natural order parameter for our analysis is the fraction of area covered by the crystal domain $A_{\text{crystal}}/A_{\text{total}}$ (Methods).

To illustrate this transition, we evaluate the crystal area fraction as a function of active advection (at a fixed activity $\alpha = -0.8$) for different times, which is shown in

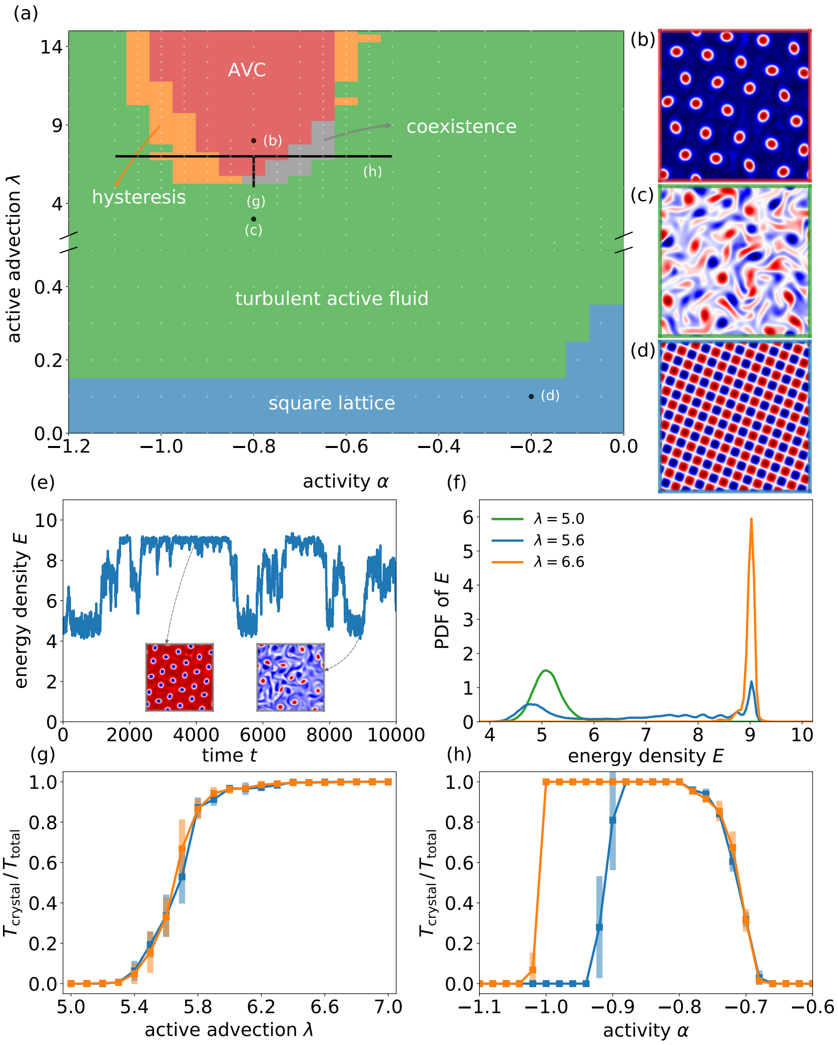

Figure 4.2: Phase diagram and melting transition ($L = 20\pi$): (a) Different phases of the active matter system as a function of activity and active advection, obtained from close to 1000 simulations (Methods). Red, green, and blue regions correspond to (b) vortex crystal, (c) active fluid and (d) square lattice, respectively. The grey and orange regions are the marginal stability regions between the active turbulence phase and the vortex crystal, corresponding to transition regions exhibiting phase coexistence and hysteresis, respectively. The white dots indicate the parameter configuration used to obtain the phase diagram. (e) A typical energy density time series for a simulation in the marginal stability region illustrates the intermittent melting and crystallization of the AVC. The insets show representative snapshots of the vorticity field. (f) Probability density functions of the energy density for values of $\lambda = 5$ (green), 5.5 (blue) and 6 (orange). (g) Melting transition of the AVC as a function of active advection ($\alpha = -0.8$) and (h) transition along the activity (λ=7) axis. The blue and orange curves correspond to increasing and decreasing values respectively of α and λ.

Fig. 4.1 (c). Below $\lambda = 5.5$, the crystal domains melt completely into a statistically isotropic active fluid. Above a critical value of $\lambda = 6.0$, almost the entire domain is covered by vortex crystals, with the area between the crystals of different polarity occupied by a layer of active fluid. There is a consistent, but slow decrease in the area of this boundary layer as advection is increased. In the following sections, we present a detailed characterization of the crystalline order and its melting.

4.3.3 Nonequilibrium phase diagram

To map out a detailed phase diagram, we have conducted ~ 1000 simulations on a domain of size $L = 20\pi$. The resulting nonequilibrium phase diagram of the active fluid model is presented in Fig. 4.2 (a). The AVC phase spontaneously emerges from random initial conditions for a narrow range of activity and active advection (indicated by the red region). Its emergence is preceded by a turbulent active fluid transient driven by vortices of both polarity [165]. This transient is terminated by a spontaneous symmetry breaking as a result of which vortices of one polarity prevail. Subsequently, more and more vortices populate the domain, leading to an eventual crystallization.

Apart from the AVC, the phase diagram demarcates two distinct phases: a turbulent active fluid (shown in green, see also Fig. 4.2 (c)) and a square lattice (shown in blue, see also Fig. 4.2 (d)), as well as transitions between them. The square lattice, which is stable when active advection is close to zero, can be explained with classical pattern formation theory [165]. Here, we focus on the transition between the turbulent active fluid and the AVC states.

In the transition region, we observe two different scenarios: phase coexistence (marked in grey) and hysteresis (marked in orange). To illustrate the transition with phase coexistence, we decrease the active advection parameter at a fixed value of the activity parameter ($\alpha = 0.8$, vertical scan). For intermediate values of the active advection, we observe an intermittent switching between active turbulence and AVCs, which can be interpreted as an temporal analogue of the spatial coexistence of opposite-polarity crystal domaines on large domains. The energy time series of a corresponding simulation is shown in Fig. 4.2 (e). In the vortex crystal state, the energy density is high due to the close packing of vortices, and the fluctuations are low. In the active fluid phase, the energy is lower and fluctuations are larger. Fig. 4.2 (f) shows the corresponding probability density functions (PDFs) for three representative cases from the vertical scan, clearly demonstrating phase coexistence for intermediate values of active advection. This is also confirmed by the time fraction of finding the system in the crystal phase, which is shown for the vertical scan in Fig. 4.2 (g).

To elucidate the hysteretic transition, we keep the active advection fixed and change the activity parameter ($\lambda = 7$, horizontal scan). In the transition region for low activit-

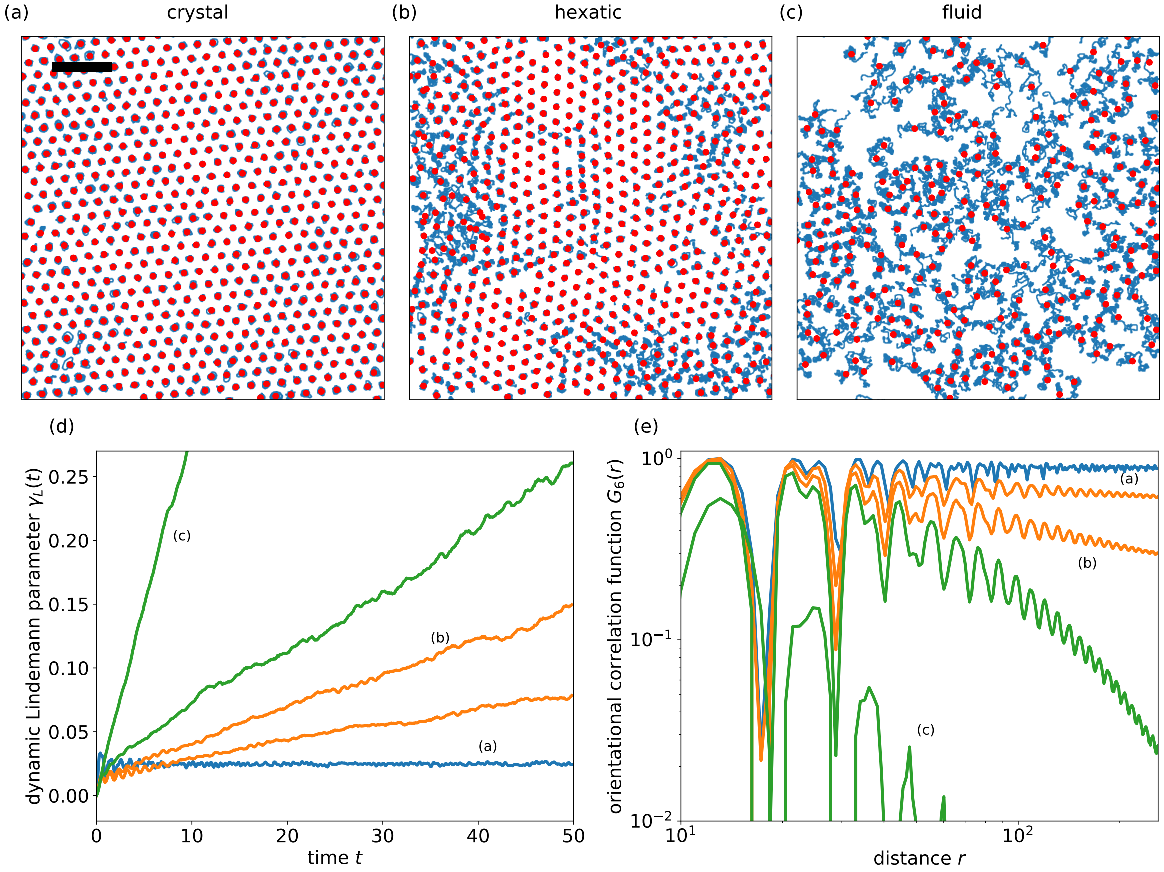

Figure 4.3: Characterization of the melting transition: Mean position of the vortex cores (red) and the corresponding trajectories (blue) in the (a) crystal ($\alpha = -0.8,\ \lambda = 15$), (b) hexatic ($\alpha = -0.725,\ \lambda = 7$) and (c) fluid ($\alpha = -0.700,\ \lambda = 7$) phases. The scale bar denotes $L = 50$. (d) Dynamic Lindemann parameter $\gamma_L(t)$ as a function of time and (e) orientational correlation function $G_6(r)$ for different parameter choices (Methods) in the crystal (blue), hexatic (orange) and fluid (green) phases. $\gamma_L(t)$ remains bounded for the crystal phase, whereas it diverges for both the hexatic and fluid phases. While $G_6(r)$ remains constant in the crystal phase, it decays algebraically as the crystal melts, demonstrating the existence of an intermediate hexatic phase. In the fluid phase, $G_6(r)$ decays faster than algebraic.

ies, a vortex crystal will not emerge from random initial conditions for these parameters, but the crystal itself is a stable solution. This is illustrated by the AVC time fraction for the horizontal scan shown in Fig. 4.2 (h), which clearly exhibits a hysteresis loop. As the activity parameter is further increased, a second transition without hysteresis is observed. As we move closer to the boundary of the active turbulence region, the vortex arrays start showing a fluid-like arrangement of vortices rather than crystal-like or hexatic. For a systematic characterization, we present results from significantly larger domains in the following sections.

4.3.4 Hexatic phase

To study the crystalline order in this system, we simulate the active fluids model in domains of size $L = 200\pi$, and track the positions of individual vortices (Methods). Deep inside the crystal regime ($\lambda = 15, \alpha = -0.8$) we observe a well-ordered structure with minimal vibrations (Figure 4.3 (a)). The oscillations remain very small in amplitude as can be seen by the position of the trajectories. As we move closer to the active turbulence region, the order starts unravelling (Fig. 4.3 (b) ($\lambda = 7, \alpha = -0.725$) and (c) ($\lambda = 7, \alpha = -0.715$)). The vibrations increase considerably and exceed the lattice spacing at several sites. As we show below, Fig. 4.3 (b) corresponds to a hexatic phase, providing crucial connection to equilibrium melting transitions following the KTHNY scenario.

To characterize the crystalline phase, one can use the dynamic Lindemann parameter, which is defined as the relative displacement of neighboring vortex cores [83, 84, 166]:

$$\gamma_L(t) = \left\langle (\Delta \boldsymbol{x}_i(t) - \Delta \boldsymbol{x}_{i+1}(t))^2 \right\rangle / 2a^2. \tag{4.2}$$

Here, $\Delta \boldsymbol{x}_i(t) = \boldsymbol{x}_i(t) - \boldsymbol{x}_i(0)$ is the temporal displacement of a vortex core position $\boldsymbol{x}_i(t)$ from its initial position $\boldsymbol{x}_i(0)$, i and $i+1$ denote neighbors, and a is the lattice spacing. For a crystal, $\gamma_L(t)$ remains bounded whereas for both hexatic and fluid phases, it diverges with time. Fig. 4.3 (d) shows the dynamic Lindemann parameter evaluated from our simulations. Indeed, it remains bounded well inside the AVC regime. As we move close to the transition region, $\gamma_L(t)$ diverges, indicating either a hexatic or a fluid phase.

To map out a possible transition to the hexatic phase, we evaluate the orientational correlation function $G_6(r)$ [78]. To this end, we calculate the orientational order $\psi_i = \sum_j \exp(6\mathrm{i}\theta_{ij})/\mathrm{N}(i)$ for each lattice site i. Here, θ_{ij} is the angle between the line connecting the neighbors i and j and an arbitrary axis, and $\mathrm{N}(i)$ is the number of neighbors. The orientational correlation is then defined as

$$G_6(r) = \langle \psi_i^* \psi_j \delta(r - r_{ij}) \rangle \,/\, \langle \delta(r - r_{ij}) \rangle \tag{4.3}$$

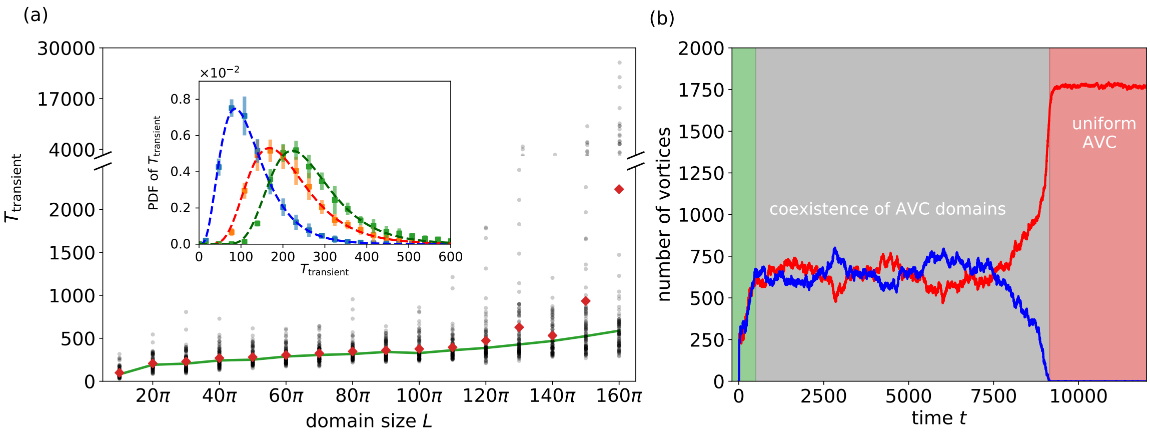

Figure 4.4: Transient durations: (a) Duration of the transients leading to the active crystal as a function of domain size L. The red dots and the green curve are the mean and median values, respectively. The change in slope at about $L = 120\pi$ mark the domain size where AVC superstructures start to become stable. (inset) Probability density function of the transient duration for $L = 10\pi$ (blue), 20π (orange) and 40π (green), obtained from 10000 simulations each, and the corresponding fit with the theoretically proposed PDF Eq. (4.4) (dashed curves). (b) The time series of the number of positive (red) and negative vortices (blue) for a simulation with large domain size ($L = 160\pi$). The green, grey, and red regions denote the initial transient, coexistence of AVC domains, and uniform AVC respectively.

where r_{ij} is the distance between vortex cores i and j, and the average is over all lattice sites i and j. Fig. 4.3 (e) shows the orientational correlation function for different regions in the phase diagram. For the crystal phase, as expected, we observe long-range orientational order (Fig. 4.3 (e)). As we move closer to the transition region, $G_6(r)$ shows quasi-long-range order characterized by an algebraic decay. This indicates that the transition to an active fluid, in this region of the phase diagram, proceeds through an intermediate hexatic phase, suggesting that this nonequilibrium melting scenario shares similarities with the KTHNY theory of melting in equilibrium systems.

4.3.5 Thermodynamic limit and supertransients

Next, we characterize the emergence of AVCs as a function of system size, eventually approaching the thermodynamic limit. To this end, we have determined the transient time until a uniform AVCs is formed for an ensemble of 100 simulations, covering domain sizes between $L = 10\pi$ and $L = 160\pi$. Fig. 4.4 (a) shows the resulting scatter plot, which demonstrates that the lifetime of the transient active fluid depends sensitively on the initial condition and increases considerably with domain size.

For small domains, this is mainly rooted in the fact that the emergence of a uniform AVC proceeds through a turbulent transient, which renders the transient time a random variable. In fact, the PDF of transition times can be well captured by

$$P(T) = \frac{\delta}{\tau}\left[1 - \mathrm{e}^{-\frac{T}{\tau}}\right]^{\delta-1} \mathrm{e}^{-\frac{T}{\tau}}, \tag{4.4}$$

where τ denotes the vortex lifetime and δ depends the domain size. This expression can be rationalized from the observation that vortex lifetimes in active turbulence have an approximately exponential distribution [135]. A good estimate for the transient time is the time after which the spontaneous symmetry breaking occurs. Its distribution can be obtained from the PDF of the time it takes for one polarity of vortices to decay, which amounts to computing the maximum survival time of a set of like-signed vortices. Assuming statistical independence of the individual decay processes yields the proposed PDF. Figure 4.4 (inset) shows the corresponding fits for the PDFs of the transient durations for different domain sizes, demonstrating an excellent agreement.

For sufficiently large domain sizes, an additional effect comes into play: crystal domains with both polarity can coexist, leading to metastable AVC superstructures with very long lifetimes. This is illustrated in Fig. 4.4 (b), which shows the number of positive and negative vortices as a function of time ($L = 160\pi$). in this example, two vortex clusters of approximately equal sizes but opposite polarity coexist for more than 8000 nondimensional time units, before a uniform AVC forms. These metastable AVC superstructures explain the extreme outliers in the transient duration which are the cause for the sharp increase of the mean duration for system sizes beyond $L = 120\pi$. This divergence of transient durations with domain size, a supertransient feature, is observed in a variety of dynamical systems such as coupled map lattices and reaction diffusion systems [167–170]. Unlike supertransient chaos, our transient state is characterized initially by a turbulent regime and then a gradually evolving superstructure. An extreme example of such a superstructure is shown in Fig. 4.1 (a) for a domain of size $L = 1000\pi$. The crystal domains are separated by a highly dynamic boundary layer of active turbulence.

4.4 Summary and Discussion

We have characterized the emergence and melting of AVCs through extensive computations of a field-theoretic description of active matter. We evaluate the melting transition both as a function of activity and active advection, mapping out the detailed non-equilibrium phase diagram. We observe a stable vortex crystal state for large active advection and intermediate values of activity, which melts for both lower and higher values of activity. Notably, we find that the exact type of this melting depends crucially on the region in phase diagram. We observe an intermediate hexatic phase, like in the equilibrium KTHNY theory, as well as hysteresis depending on the path in the phase diagram. This points to a nontrivial dependence of the transition on activity and active advection. Our system therefore exhibits a rich transition scenario from ordered to disordered states, which complements previous studies on transitions in active fluids [56, 94, 156, 171]. In the thermodynamic limit, vortex domains of opposite polarity emerge, which are separated by domain boundaries exhibiting active turbulence. In their competition to form a uniform vortex crystal of one polarity, these domains show features of metastable transient AVC superstructures.

Our results furthermore indicate that the properties of AVCs share close similarity with equilibrium crystals. One of the most surprising aspects of the melting process reported here is the coexistence of a discontinuous transition (through hysteresis) and a KTHNY-like melting scenario. In contrast to the equilibrium analogues of our system, such as point vortex lattices and their realizations in superconductors and superfluids [154, 172, 173], we observe a dynamic emergence of the vortex crystal from an active fluid through an extended turbulent transient. Vortex arrays, which share some of the properties of the AVC that we discuss here, have been observed in a range of systems including forced two-dimensional Navier-Stokes system [143], drift-wave turbulence [174] as well as quasi-geostrophic flows [145], which could motivate the analysis of melting transitions in a much larger class of systems.

The experimental exploration of the results presented here will be an exciting direction for future work. Arguably, the best candidate to study the melting of active vortex crystals is a dense suspension of spermatozoa, which show both, active turbulence [20] as well as self-organized regular vortex arrays [12]. Although the measurements in this experiment suggested a fluid-like arrangement of vortices, rather than crystal-like or hexatic, it may be possible to achieve crystalline ordering through a careful tuning of experimental conditions. If a vortex crystal phase is achieved in such a system, the activity can be tuned, for instance, by changing the motility through the ambient temperature [175] to achieve a potential melting transition. It is also worth noting that the sperm cells on a planar surface have a preferred handedness [176] precluding the observation of a spontaneously broken rotational symmetry. This could be alleviated by confinement between two walls. Broken-symmetry states of ferromagnetic and antiferromagnetic ordering of bacterial vortices have been observed in periodically patterned substrates [128, 177]. We expect that further development of experimental realization of this system will significantly enhance our knowledge of crystalline order, not just in active matter, but in out-of-equilibrium systems in general.

4.5 Methods

4.5.1 Simulation details

We perform direct numerical simulations of the vorticity field $\omega = \nabla \times \boldsymbol{u}$ in a periodic domain by using a fully dealiased pseudo-spectral algorithm. The mean velocity $\langle \boldsymbol{u} \rangle$ is integrated separately. The corresponding evolution equations follow from Eq. (4.1) and

Figure	L	λ	α	N	Δt
4.1(a)	1000π	7.0	-0.800	8192^2	0.005
4.1(b)	1000π	5.6	-0.800	8192^2	0.005
4.1(c)	1000π	$[5, 6.5]$	-0.800	8192^2	0.005
4.2(a)	20π	[0.0, 15.0]	$[-1.200,\ 0.000)$	256^2	0.005
4.2(b)	20π	8.0	-0.800	1024^2	0.001
4.2(c)	20π	3.0	-0.800	1024^2	0.001
4.2(d)	20π	0.1	-0.200	1024^2	0.001
4.2(e)	20π	5.6	-0.800	256^2	0.005
4.2(f)	20π	5.0, 5.6, 6.6	-0.800	256^2	0.005
4.2(g)	20π	[5.0, 7.0]	-0.800	256^2	0.005
4.2(h)	20π	7.0	$[-1.100,\ -0.500]$	256^2	0.005
4.3(a)	200π	15.0	-0.800	1024^2	0.005
4.3(b)	200π	7.0	-0.725	1024^2	0.005
4.3(c)	200π	7.0	-0.715	1024^2	0.005
4.3(d)	200π	7.0	-0.750,-0.725,-0.715,-0.700	1024^2	0.005
4.3(d)	200π	15.0	-0.800	1024^2	0.005
4.3(e)	200π	7.0	-0.750,-0.725,-0.715,-0.700	1024^2	0.005
4.3(e)	200π	15.0	-0.800	1024^2	0.005
4.4(a)	$[10\pi,\ 160\pi]$	7.0	-0.800	256^2, 512^2, 1024^2	0.005
4.4(a) inset	10π, 20π, 40π	7.0	-0.800	256^2	0.005
4.4(b)	160π	7.0	-0.800	1024^2	0.005
4.6	1000π	5.6	-0.800	8192^2	0.005

Table 4.1: Simulation parameters: Domain size L, active advection parameter λ, activity parameter α, number of grid points N, time step Δt. The parameter β is set to 0.01 in all simulations.

take the form:

$$\partial_t \omega + \lambda \boldsymbol{u} \cdot \nabla \omega = -\big(1 + \Delta\big)^2 \omega - \alpha\omega - \beta \nabla \times \left(\left|\boldsymbol{u}^2\right| \, \boldsymbol{u}\right) \tag{4.5}$$

$$\partial_t \langle \boldsymbol{u} \rangle = -\big(1 + \alpha\big) \langle \boldsymbol{u} \rangle - \beta \left\langle |\boldsymbol{u}|^2 \, \boldsymbol{u} \right\rangle . \tag{4.6}$$

We solve Eqs. (4.5) and (4.6) with a fourth-order Runge-Kutta method for time stepping combined with an integrating factor for the linear terms. Our code is parallelized using GPUs (graphics processing units) in order to accelerate the computations. For the results discussed in the main text, the parameter values are listed in table 4.1.

4.5.2 Phase diagram

The phase diagram (Fig. 4.2 (a)) is obtained from simulations of 477 different parameter configurations as shown in Fig. 4.5 (a). For each configuration, we use two different initial conditions: a random initial condition (as exemplified in Fig. 4.5 (b)) and a

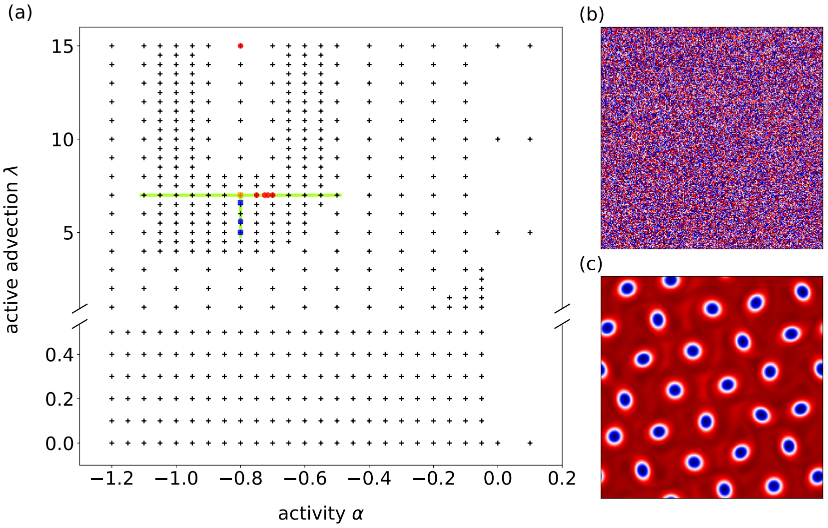

Figure 4.5: (a) The parameter configuration used to obtain the phase diagram (Fig. 4.2). Each cross represents simulations with two different initial conditions as shown in (b) and (c). The PDFs in Fig. 4.2 (f) are based on simulations with parameters marked in blue. The phase transition curves Fig. 4.2 (g) and (h) are based on simulations with parameters marked in green. The parameters used in Fig. 4.3 are indicated in red. Fig. 4.4 and 4.1 (a) are based on the parameter choice shown in yellow. Fig. 4.1 (b) and 4.2 (e) are based on the parameter choice shown in blue circle.

vortex crystal (Fig. 4.5 (c)).

The different phases shown in Fig. 4.2 (a) are defined as follows. The square lattice, active turbulence and vortex crystal phases show obvious qualitative differences as noted in the main text and are easily distinguished. The hysteresis phase in the marginal stability region is identified as such when the simulations are bistable; the simulations starting with random initial conditions result in an active turbulence phase whereas a vortex crystal initial condition remains stable. The simulations are checked for convergence until a total simulation time of T=2000 (4×10^5 time steps). The coexistence region is defined by evaluating the PDF of the energy density. If the PDF has two peaks (see, e.g., Fig. 4.2 (f)), it is defined as a temporally intermittent pattern.

4.5.3 Phase transition

The phase transition between active turbulence and vortex crystals in small domains (Fig. 4.2 (g) and (h)) is characterized as follows. For the transition curves in both increasing and decreasing directions of parameter values, we conduct simulations in the range $5.0 \leq \lambda \leq 7.0$ and $-1.1 \leq \alpha \leq -0.6$. For $\lambda = 5$ and $\alpha = -1.1$, we start our simulation from random initial conditions. For rest of the simulations, the final snapshot of the previous simulation is used as the initial condition. Once a statistically steady state is reached (after about 10^6 time steps), we collect data for 10^6 time steps and evaluate the PDF of the energy density. If the PDF has only one peak, the order parameter $T_{\text{crystal}}/T_{\text{total}}$ takes the value 0 or 1, depending on the phase. Otherwise, the

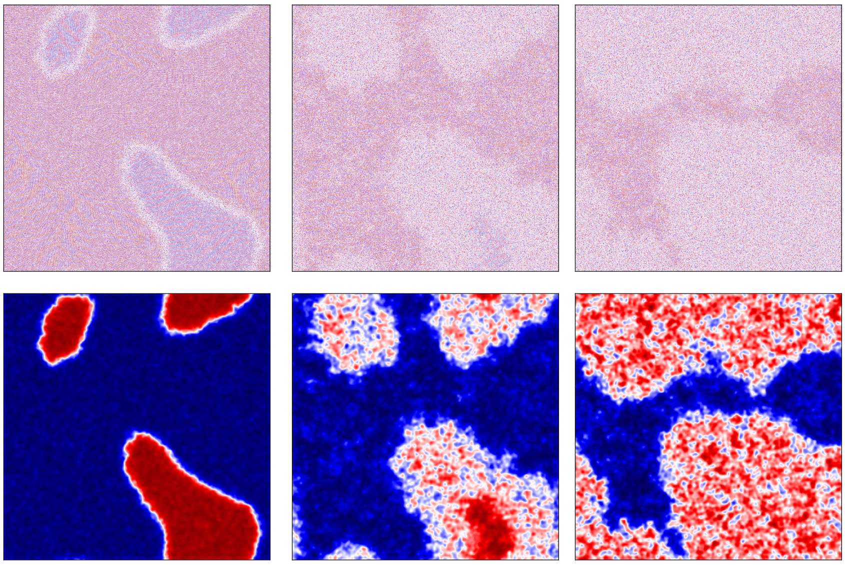

Figure 4.6: Analysis of melting of AVC superstructures: Top row shows the vorticity field for $\lambda = 5.6$ at different times (initial condition, at $t = 1000$ and at $t = 2000$). Bottom row shows the corresponding smoothed fields.

energy density at the minimum between the two peaks of the PDF, E_{min} is evaluated. The order parameter then takes the value of the probability $P > E_{\text{min}}$. This process is repeated 5 times, and the mean and the standard deviations are used to construct the transition curves and estimate the uncertainties, which are shown in Fig. 4.2 (g) and (h).

To evaluate the phase transition curve in large domains (Fig. 4.1(c)), we first identify centers of the strong vortices [54, 135]. Then an order parameter field is obtained by calculating, for each point (x, y), the difference between the number of positive and negative vortices within a circle of radius r centered at (x, y) (r is about half the mean distance between the nearest neighbors and next nearest neighbors). The resulting field is then smoothed using a Gaussian filter with standard deviation $\sigma = 12$. The original vorticity field and the smoothed field are shown in Fig. 4.6. The turbulent region is then defined as the area where the absolute value of this smoothed field is less than half the maximum value of the field. Once this turbulent region is defined, the order parameter $A_{\text{crystal}}/A_{\text{total}}$ is calculated by evaluating the fraction of the total area covered by the vortex crystal.

4.5.4 Transient durations

To evaluate transient durations (Fig. 4.4 (a) and (b)), we conduct simulations starting with random initial conditions until a converged vortex crystal state is reached for each domain size. The convergence is defined as follows. By employing a vortex identification algorithm [54, 135], we obtain a time series of the number of strong vortices of both polarity. A converged vortex crystal is obtained when the number of vortices of either sign reaches 93% of the theoretical maximum number of vortices possible in the domain. To obtain the mean and median transient durations in Fig. 4.4 (a), the simulations are repeated 100 times for each domain size and the corresponding mean and median durations are calculated. The PDFs (inset Fig. 4.4 (a)) are obtained by evaluating the transient durations for three different domain sizes from 10000 simulations each, starting from random initial conditions. The error bars correspond to the difference between the maximum and the minimum from the 5 bootstrapped PDFs obtained from 2000 simulations each. The theoretical curves are obtained by fitting the numerical data to Eq. (4.4). The corresponding values of the free parameters δ and τ are, respectively, 4.8 and 55 for $L = 10\pi$ (blue curve), 10 and 73 for $L = 20\pi$ (orange curve) and 21 and 73 for $L = 40\pi$ (green curve).

4.5.5 Dynamic Lindemann parameter and orientational correlation

The dynamic Lindemann parameter and the orientational correlations are evaluated as follows. For each parameter choice in Fig. 4.3, simulations starting from random initial conditions are run for at least 1.2×10^7 time steps until a statistically steady state is reached. To evaluate the dynamic Lindemann parameter, we then obtain 500 snapshots separated by $\Delta t = 0.1$. For each snapshot, we identify the centers of strong vortices [54, 135]. The trajectory of each vortex core is then tracked. Only vortices which survive the entire duration of the simulation after reaching the statistically steady state are included in the analysis. The dynamic Lindemann parameter is then evaluated following Eq. (4.2) in the main text.

The orientational correlation is evaluated according to Eq. (4.3) in the main text, after identifying the centers of the strong vortices in converged simulations. The results are averaged across 10 snapshots (with $\Delta t = 2000$) each from three simulations with different initial conditions.

5 Summary and Discussions

Active matter is one of the next frontiers in classical physics, where the theories of statistical mechanics can be extended to nonequilibrium systems. Extensive research in the past two decades in this new field has not only tremendously improved our knowledge about collective dynamics in biological systems but also has provided a framework to study systems out of equilibrium. In this work, we have shown that general phenomenological approaches can be used to study the properties of different phases in active matter. We have explored turbulent dynamics, novel forms of pattern formation and crystallization as well as phase transitions between them. We have employed tools from statistical physics, fluid dynamics and classical pattern formation theory, illustrating the rich interdisciplinary nature of the topic. Our results open up intriguing avenues for future work on nonequilibrium systems.

Before we conclude, a summary of our results is given below. We end this study with an outlook on possible directions for future research.

Turbulence in active fluids

One of the striking examples of the rich variety of phases exhibited by active fluids is the low Reynolds number active turbulence. This active turbulence phase is exhibited by systems ranging from bacterial suspension to microtubule-kinesin mixtures and spermatozoa suspensions. In Chapter 2, we conducted a statistical characterization of this dynamical phase. We found that the single-point velocity statistics in the active turbulence phase is close to Gaussian, similar to hydrodynamic turbulence. As we reduce activity, the velocity statistics become closer to Gaussian. The two-point velocity statistics deviate from Gaussian for length scales smaller than the coherent vortex structures in the system. This is true for statistical investigations both in the Eulerian as well as in the Lagrangian frames of reference. For smaller values of the activity, the multi-point velocity statistics also become close to Gaussian, due to the smaller sizes of the coherent vortex structures.

One characteristic which contrasts active turbulence from hydrodynamic turbulence is the sharp selection of the sizes of the vortices as well as the magnitude of the vorticity at the vortex cores. To quantify this, we investigated the vorticity distribution at the vortex cores. We found that this follows a trimodal distribution. This results from the weak vortices close to zero and the intense ones of both the signs. The PDF falls off rapidly for the intense vortices. The lifetime of the vortices decays exponentially for both intense and weak vortices. For strong vortices, the characteristic timescale of the decay is larger. We also looked at other statistical quantities like the mean square displacement of the tracers, which shows a ballistic behavior for short times and diffusive for large times. These statistical characterizations lay the groundwork for the theoretical analysis of turbulence in active fluids.

In Chapter 3, we developed a theory of velocity correlations in active turbulence. One of the difficulties of such an analysis is the nonlinear and non-local nature of the equations of motion describing the active fluid, resulting in a closure problem. The non-Gaussian statistical features further complicate this analysis since a naive Gaussian approximation will fail to capture important dynamical features of this system. We used a closure model from hydrodynamics, called the eddy-damped quasi-normal Markovian approximation, to develop a theory for the velocity correlations. This theory captures the statistics of the system very well for different values of activity. Our results on closure approximation in active turbulence points to the applicability of classical turbulence theory in explaining the properties of active matter systems.

Active vortex crystals

In the second half of this dissertation, we present the first field-theoretic description of the active vortex crystal phase. Active vortex crystals are two-dimensional nonequilibrium crystals formed by vortices of active matter. Our theoretical results on active vortex crystals are important in the context of the observation of well-ordered vortex arrays in spermatozoa suspensions. In Chapter 3 we showed that self-organized vortex crystals are a stable solution to the active matter model that we investigate. The self-organization of the vortices into a crystalline structure is preceded by a spontaneous discrete symmetry breaking which results in choosing vortices of one sign over another. We also found that the inverse energy transfer in this system is important in defining the characteristics of this vortex crystal phase. The inverse transfer of energy results in the system selecting the neutral wavenumber over the most unstable wavenumber.

We further characterized the active vortex crystal phase in Chapter 4. Like two-dimensional crystals in equilibrium, active vortex crystals display long-range orientational order. We analyzed the melting of active vortex crystals into an active fluid. By evaluating the nonequilibrium phase diagram of the active matter system, we found that its melting may proceed through two different mechanisms. In one scenario, the transition region is characterized by a hysteretic phase. Here, the vortex crystal does not spontaneously form from an active fluid, but a vortex crystal itself remains stable. In the second transition scenario, the melting proceeds through an intermediate hexatic phase. This is similar to the predictions of the KTHNY theory of the melting of two-dimensional crystals in equilibrium.

While investigating the formation of the active vortex crystals, we found an interesting dependence on the domain sizes. The transient duration before the emergence of the vortex crystals increases with the domain size. Beyond a critical domain size, the mean transient duration increases considerably. This happens due to the formation of superstructures of vortex crystal domains of opposite polarity. For very large domains, these superstructures become metastable leading to the formation of slowly evolving crystal domain structures.

5.1 Outlook

This work, like many theoretical works in the field of active matter, is based on the phenomenological modeling of active systems. One of the shortcomings of such an approach is the difficulty in making exact quantitative comparisons to experiments. Perhaps the most important development required to substantiate our results is direct comparisons with experiments. In this context, it is also worth noting that, as we discussed in the introduction, the active fluids model can be approximately derived by coarse-graining the microscopic equations of motion. Further development in this direction could allow the mapping between the theoretical parameters and experimental conditions.

There are many statistical results that we present which can be tested experimentally. For instance, one of our important numerical results regarding the statistical features of active turbulence is the deviation from Gaussian within the length scales of the coherent vortex structures. It is feasible to do such measurements in bacterial and microtubule systems and these could give us better information about the statistical nature of the active turbulence velocity field. The distribution of the lifetimes of the vortices is another interesting quantity that can be tested experimentally.

One of the central results of this dissertation, the applicability of the classical turbulence closure scheme in active fluids, proves the utility of hydrodynamics as a framework to explore the dynamics of active fluids. To quote a few examples where this could be done, boundary layer theories from fluid dynamics can be used to analyze dynamics of active flows over a substrate and particle transport in such systems can be investigated utilizing the rich knowledge of particle transport in turbulence.

Crystallization in active matter, that we discuss in Chapter 4, opens up a range of interesting questions and possibilities for future research. We have reported on spontaneous emergence of vortex crystals from turbulent dynamics in active fluids. Although true vortex crystals have not yet been observed in experiments there are results, such as in dense spermatozoa suspensions, which suggest that such realizations may indeed be possible.

Another direction for future research is the investigation of the compressible version of the active matter model studied here. A compressible model would allow for more realistic comparisons with experiments. Such an analysis would open up regimes inaccessible in the current model. For example, it is intriguing to analyze how the active matter density waves' propagation differs between the active turbulence phase and the vortex crystal phase.

To conclude, the results presented in this dissertation show that chaotic dynamics and crystallization in active fluids, as well as other features of active matter, are paradigmatic nonequillibrium phenomena that can be studied using interdisciplinary tools. Experimental and theoretical work in this direction could substantially increase our understanding of physics out of equilibrium.

A Algorithm for numerically solving the active matter model

Here we present a pseudospectral algorithm to solve the active fluids model [178]. In a pseudospectral scheme, parts of the calculations take place in the Fourier space while the rest takes place in the real space. The rationale behind this is to evaluate the differential operators in the Fourier space (since differentiations become multiplications in the Fourier space) and the nonlinear operations in the real space. Thus such an algorithm would involve, for each time step, the Fourier transform(s) of the solution as well as its inverse(s). These transforms are usually the computationally most intensive portion of the algorithm. We utilize a Fast Fourier Transfer scheme (FFTW) to evaluate the Fourier transforms.

Our goal is to numerically solve Eq. (1.8). Instead of solving the equations for the velocity field, we use the vorticity formulation of the equations of motion since vorticity is a pseudoscalar. To this end, consider the vorticity equations obtained by taking the curl of Eq. (1.8)

$$\partial_t \omega + \lambda \boldsymbol{u} \cdot \nabla \omega = -(1+\Delta)^2 \omega - \alpha \omega - \beta \nabla \times (\boldsymbol{u}^2 \, \boldsymbol{u}),$$

where $\omega = \nabla \times \boldsymbol{u}$.

Now we take the Fourier transform of the above equation. This results in

$$\partial_t \hat{\omega} = N(\widehat{\omega, \boldsymbol{u}; \lambda}, \beta) - L(k; \alpha) \hat{\omega}$$

where $\hat{f}$ denotes the Fourier transform of f, $N(\omega, \boldsymbol{u}; \lambda, \beta) = -\lambda \boldsymbol{u} \cdot \nabla \omega - \beta \nabla \times (\boldsymbol{u}^2 \, \boldsymbol{u})$ and $L(k; \alpha) = (1-k^2)^2 + \alpha$.

The pseudospectral algorithm proceeds according to the following steps:

Step 1: Start with an initial condition for the vorticity field ω and take its Fourier transform $\hat{\omega}$.

Step 2: Obtain the velocity fields in the Fourier space, $\hat{u}_x$ and $\hat{u}_y$, from the vorticity field $\hat{\omega}$ as shown below:

$$\hat{u}_x = \mathrm{i}k_y \frac{\hat{\omega}}{k^2},$$
$$\hat{u}_y = -\mathrm{i}k_x \frac{\hat{\omega}}{k^2}.$$

Step 3: Inverse Fourier Transform $\hat{\omega}$ to ω, $\hat{u}_x$ to u_x and $\hat{u}_y$ to u_y. Then calculate the nonlinear terms in the real space. To this end, evaluate $u_x\omega$, $u_y\omega$, $\boldsymbol{u}^2 u_x$ and $\boldsymbol{u}^2 u_y$.

Step 4: Fourier transform $u_x\omega$, $u_y\omega$, $\boldsymbol{u}^2 u_x$ and $\boldsymbol{u}^2 u_y$ and then evaluate $N(\widehat{\omega, \boldsymbol{u}; \lambda}, \beta)$.

Step 5: The evolution equation, given by

$$\partial_t \hat{\omega} = N(\widehat{\omega, \boldsymbol{u}; \lambda}, \beta) - L(k; \alpha)\hat{\omega},$$

can be written as

$$\partial_t (e^{L(k;\alpha)t} \hat{\omega}) = e^{L(k;\alpha)t} N(\widehat{\omega, \boldsymbol{u}; \lambda}, \beta).$$

Now the above equation can be solved, for time n with $\mathrm{d}t = \delta t$, using second order Runge-Kutta scheme [179] as given below

$$\begin{aligned}
\hat{\omega}_* &= e^{-L(k;\alpha)\delta t/2} \left[\hat{\omega}_n + \frac{\delta t}{2} N(\widehat{\omega_n, \boldsymbol{u}_n; \lambda}, \beta) \right], \\
\hat{\omega}_{**} &= e^{-L(k;\alpha)\delta t/2} \hat{\omega}_n + \delta t e^{-L(k;\alpha)\delta t/2} N(\widehat{\omega_*, \boldsymbol{u}_*; \lambda}, \beta), \\
\hat{\omega}_{n+1} &= \hat{\omega}_{**}.
\end{aligned}$$

Also, to account for aliasing, we discard half of the Fourier modes after each timestep [77, 135]. Note that by using the vorticity formulation, the information about the mean velocity is lost. Thus for each timestep, the mean velocity is integrated separately, by using the following equation, and the corresponding value is added to the numerically obtained velocity field.

$$\partial_t \langle \boldsymbol{u} \rangle = -\big(1 + \alpha\big) \langle \boldsymbol{u} \rangle - \beta \left\langle |\boldsymbol{u}|^2 \, \boldsymbol{u} \right\rangle .$$

B A generalization to the active matter model

So far we have investigated the properties of active matter systems within the confines of the model introduced by Wensink et al. [13] (Eq. (1.8)). However, as we have already discussed briefly in the introduction, this model in the vorticity formulation can be thought of as an advected Swift-Hohenberg-like equation. When the advection is close to zero, we recover the stationary patterns which can be analyzed by using classical pattern formation theory (Chapter 3). As the strength of the advection is increased, an active fluid phase or an active crystal can be observed. This raises the question of whether these observations can be repeated within the larger class of the advected Swift-Hohenberg-like equations for different nonlinearities. Here we examine this question by analyzing the properties of an advected Swift-Hohenberg model and comparing it with Eq. (1.8). We find that the active fluid phase, the active crystal phase as well as the different transitions between them can also be observed in this generalized model.

As our starting point, consider a general class of equations describing the evolution of the vorticity field ω in two dimensions, given by $\partial_t\omega + \lambda \boldsymbol{u} \cdot \nabla\omega = L(\nabla;\alpha)\omega + N(\omega, \boldsymbol{u}; \beta)$. Here L is a linear operator, N is a nonlinear functional and the incompressible advecting field $\boldsymbol{u}$ is such that $\nabla \times \boldsymbol{u} = \omega$. λ determines the strength of the advection. The linear operator may take the form $L = -(1+\Delta)^2 - \alpha$ so that a linear instability is introduced at wavenumber $k = 1$ and the range and intensity of the unstable modes are given by the value of the parameter α. For the standard active matter model (SAM) which we have analyzed in the previous chapters, the nonlinear term takes the form $N(\omega, \boldsymbol{u}; \beta) = -\beta\nabla \times \boldsymbol{u}^2\boldsymbol{u}$. To investigate the generality of our results here, we also look at an alternate form for the nonlinearity, similar to the standard Swift-Hohenberg equation, given by $N(\omega, \boldsymbol{u}; \beta) = -\beta\omega^3$ [180]. We denote this model as the advected Swift-Hohenberg (ASH) system.

As we have already described, the equation of motion for the ASH model is given by

$$\partial_t\omega + \lambda \boldsymbol{u} \cdot \nabla\omega = -(1+\Delta)^2\omega - \alpha\omega - \beta\omega^3. \tag{B.1}$$

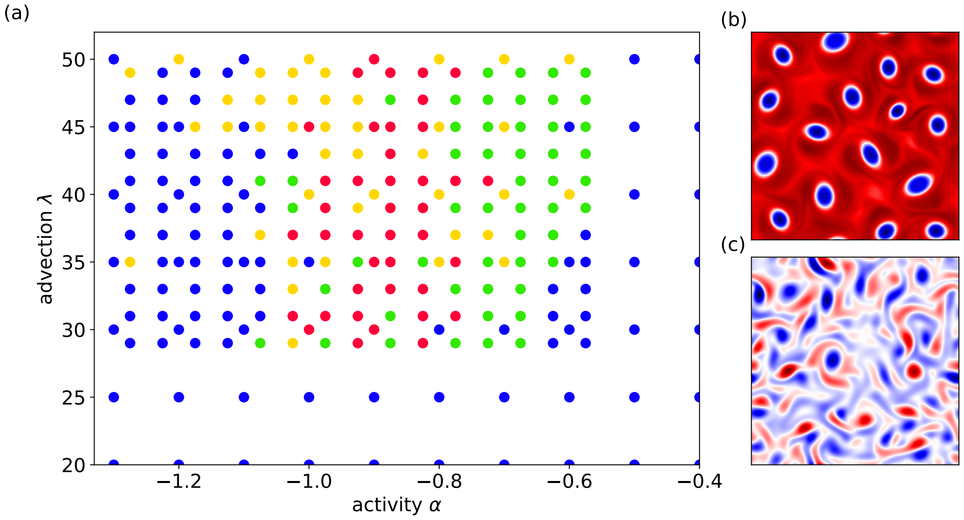

Figure B.1: Phase diagram of the ASH model on a $20\pi \times 20\pi$ domain obtained by numerically solving the ASH equation: (a) Different phases of the ASH system as a function of activity α and advection λ. Red and blue dots correspond to (b) vortex crystal and (c) active fluid phases, respectively. The green and yellow regions are the marginal stability regions between the active fluid phase and the vortex crystal. Note that, unlike the SAM model the regions corresponding to the vortex crystal phase in the ASH model is quite dispersed. The simulations were conducted on a 256×256 domain by using a second-order Runge Kutta scheme for time stepping.

Here the sole order parameter is ω, the vorticity field, and $\boldsymbol{u}$ is the corresponding velocity field.

Our goal is to compare the properties of the ASH model with that of the SAM model. To this end, we present the phase diagram of the ASH model in Fig. B.1. The ASH model also forms the different types of phases exhibited by the SAM model, including the vortex crystal phase (red dots), the active fluid phase (blue dots) as well as the two different transition phenomena exhibited in the SAM model. Like the SAM model, melting can proceed through a hysteretic phase (shown in yellow) or with intermittent patterns (green dots). It is interesting to note that the regions in the phase diagram where these different phases are observed also agree between the two models; for instance the vortex crystal is stable for intermediate activity and high advection. However, the actual values of the parameters over which we observe the corresponding phases vary considerably.

There are important differences between the vortex crystal phase in the ASH model and the SAM model. The vortices in the SAM model are more uniformly sized than the ASH model as can be observed from Fig. B.1 (b). Furthermore, the crystalline phase in the ASH model appears less stable than the SAM model. In the phase diagram, the region corresponding to the vortex crystal phase is more dispersed compared to the SAM model. Thus unlike the SAM model, the transition region between the vortex crystal and the active fluid is not very well defined.

The brief exposition above exemplifies that the vortex crystalline phase that we observe is not confined to the particular set of equations that we investigated in the previous chapters. Our observations suggest that the advected Swift-Hohenberg equations represent a novel class of pattern-forming systems with potential applications to nonequilibrium phenomena such as active matter.

C Linear stability analysis of the stationary patterns

As we noted in Chapter 3, for zero advection the active matter model results in a stationary pattern that can be analyzed by using the tools from classical pattern formation theory [165]. This is also true for the ASH model analyzed in Appendix B [134]. Surprisingly, these patterns remain stable for small but finite values of advection. Similar observations have been made, e.g., in two-dimensional Navier-Stokes systems with spatially periodic forcing [181]. To investigate the stability of these patterns in the presence of finite advection, here we present a linear stability analysis of the stationary patterns for both models.

For simplicity, we conduct our analysis by using the stream function formulation of the equations of motion for the ASH and the SAM model, where the stream function ψ is given by $\Delta\psi = -\omega$.

We start by noting that for small values of advection λ, ψ can be written as

$$\psi = \psi_0 + \tilde{\psi},$$

where ψ_0 is a base state given by the stationary solution and $\tilde{\psi}$ is the fluctuation around the base state. The stability of the models can be analyzed by linearizing the equations of motion around the base state. The linearized equations of motion for $\tilde{\psi}$ for the ASH model is given by,

$$\begin{aligned}\partial_t \Delta\tilde{\psi} = &- \left[(1+\Delta)^2 + \alpha\right]\Delta\tilde{\psi} - \lambda\left[\partial_x\psi_0\partial_y\Delta\tilde{\psi} + \partial_x\tilde{\psi}\partial_y\Delta\psi_0 - \partial_y\psi_0\partial_x\Delta\tilde{\psi} - \partial_y\tilde{\psi}\partial_x\Delta\psi_0\right] \\ &- 3\beta(\Delta\psi_0)^2\Delta\tilde{\psi}.\end{aligned}$$

We assume a periodic domain of dimension $(2N\pi \times 2N\pi)$, where N is a positive integer. The ASH model forms a stripe solution for zero advection. With a suitable choice for the coordinate system, the base state can be written as

$$\psi_0 = Ae^{\mathrm{i}x} + \mathrm{c.c}\ \left[A = \sqrt{\frac{-\alpha}{3\beta}}\right]$$

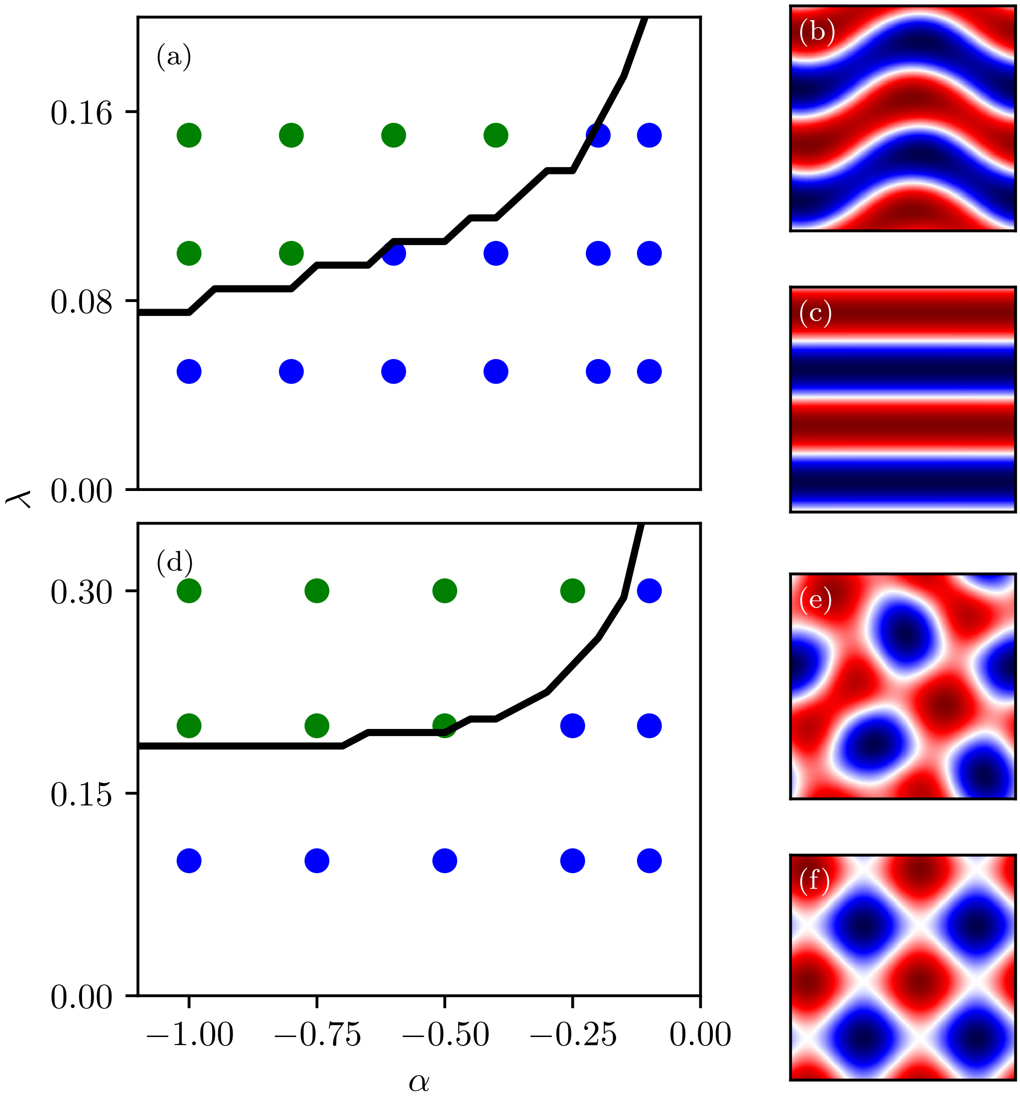

Figure C.1: Linear stability of the stationary patterns in the ASH and the SAM model: (a) Stationary patterns (blue dots, (c)) and distorted patterns (green dots, (b)) in the ASH system as a function of activity α and advection λ. The black curve is the marginal stability curve for the stationary pattern. Panel (d) shows the corresponding plot for the SAM system. It is clear that for both the models, the stationary patterns remain stable for small but finite values of advection. The marginal stability curve, obtained through a linear stability analysis, captures the transition to distorted patterns.

This solution including the value of the amplitude can be obtained by solving the corresponding amplitude equation (see refs. [134, 165] and Chapter 3). Here we have truncated the solution at the first harmonic.

The fluctuations $\tilde{\psi}$ can be expanded into Fourier modes, given by

$$\tilde{\psi} = \sum_{n,m=-M}^{M} \phi_{n\,m} e^{\mathrm{i}\frac{nx+my}{N}} + \text{c.c.}$$

Here we have truncated all perturbations above Fourier mode M, since we assume that the higher order modes do not destabilize the system. Substituting this into the linearized equations, we obtain the eigenvalue equations

$$\begin{aligned}\dot{\phi}_{n\,m} = &- \left[\left(1-k^2_{n\,m}\right)^2 + \alpha\right]\phi_{n\,m} + \frac{\lambda A}{N k^2_{n\,m}}\left[\phi_{n-N\,m} m(k^2_{n-N\,m}-1) - \phi_{n+N\,m} m(k^2_{n+N\,m}-1)\right] \\ &- \frac{3\beta A^2}{k^2_{n\,m}}\left[\phi_{n-2N\,m}k^2_{n-2N\,m} + \phi_{n+2N\,m}k^2_{n+2N\,m} + 2\phi_{n\,m}k^2_{n\,m}\right],\end{aligned}$$

where $k^2_{nm} = \frac{n^2+m^2}{N^2}$.

Since we have discarded all higher-order harmonics when considering the base state, the above eigenvalue equations will result in positive eigenvalues corresponding to the eigenvectors denoting the exact solution. However, since the amplitudes of the higher harmonics are much smaller compared to the first harmonic, we assume that including the entire solution would merely change these eigenvalues without altering others. Thus we discard the eigenvalues corresponding to the eigenvectors forming the exact solution and evaluate the next largest eigenvalue. Following this, we can analyze the stability of the lattice states. By evaluating the values of the parameters where the eigenvalue reaches zero, we can calculate the marginal stability curve for the stationary patterns. We have numerically solved this eigenvalue problem for $4\pi \times 4\pi$ domain (Fig. C.1). The DNS solutions show good agreement with the results from the stability analysis presented here. The stationary patterns are stable for finite, but small values of advection, but as the advection is increased the patterns get distorted eventually resulting in an active fluid phase.

We present below the corresponding analysis for the SAM model. The linearized equation of motion around the base state is given by

$$\begin{aligned}\partial_t \Delta\tilde{\psi} = &-\Big[(1+\Delta)^2+\alpha\Big]\Delta\tilde{\psi} - \lambda\Big[\partial_x\psi_0\partial_y\Delta\tilde{\psi} + \partial_x\tilde{\psi}\partial_y\Delta\psi_0 - \partial_y\psi_0\partial_x\Delta\tilde{\psi} - \partial_y\tilde{\psi}\partial_x\Delta\psi_0\Big] \\ &- \beta\Big[\partial_x\left[\partial_x\tilde{\psi}(3(\partial_x\psi_0)^2 + (\partial_y\psi_0)^2) + 2\partial_x\psi_0\partial_y\psi_0\partial_y\tilde{\psi}\right] \\ &+ \partial_y\left[\partial_y\tilde{\psi}(3(\partial_x\psi_0)^2 + (\partial_y\psi_0)^2) + 2\partial_x\psi_0\partial_y\psi_0\partial_y\tilde{\psi}\right]\Big].\end{aligned}$$

SAM model results in a square lattice phase for zero advection and the base state can be written as

$$\psi_0 = A(e^{\mathrm{i}x} + e^{\mathrm{i}y}) + \text{c.c} \quad \left[A = \sqrt{\frac{-\alpha}{5\beta}}\right].$$

Here, again, we have discarded all higher order harmonics.

Then the eigenvalue equations are for the SAM model takes the form

$$\begin{aligned}\dot{\phi}_{n\,m} = &-\left[\left(1-k_{n\,m}^2\right)^2 + \alpha\right]\phi_{n\,m} + \frac{\lambda A}{N k_{n\,m}^2}\Big[\phi_{n-N\,m} m(k_{n-N\,m}^2 - 1) - \phi_{n+N\,m} m(k_{n+N\,m}^2 - 1) \\ &- \phi_{n\,m-N} n(k_{n\,m-N}^2 - 1) + \phi_{n\,m+N} n(k_{n\,m+N}^2 - 1)\Big] + \frac{3\beta A^2}{N^2 k_{n\,m}^2}\Big[\phi_{n-2N\,m}(3n(n-2N) + m^2) \\ &+ \phi_{n+2N\,m}(3n(n+2N) + m^2) - 8\phi_{n\,m}(n^2+m^2) + \phi_{n\,m-2N}(n^2 + 3m(m-2N)) \\ &+ \phi_{n\,m+2N}(n^2 + 3m(m+2N)) + 2\phi_{n-N\,m-N}((m-N)n + (n-N)m) \\ &+ 2\phi_{n+N\,m+N}((m+N)n + (n+N)m) - 2\phi_{n-N\,m+N}((m+N)n + (n-N)m) \\ &- 2\phi_{n+N\,m-N}((m-N)n + (n+N)m)\Big]\end{aligned}$$

The results for the stability of the square lattice state for the SAM model and the corresponding comparison with DNS are shown in Fig. C.1. Thus both in the ASH model and the SAM model, the stationary pattern remains stable for small values of advection. Interestingly, the stability of these patterns also depends on the value of the activity. As the activity is reduced, the value of advection required to destabilize the patterns increases. In conclusion, the stability of stationary patterns in advected Swift-Hohenberg models can be captured by using a linear stability analysis w.r.t the corresponding stationary states.

List of Figures

Bibliography

[1] M. C. Marchetti, J.-F. Joanny, S. Ramaswamy, T. B. Liverpool, J. Prost, M. Rao and R. A. Simha. 'Hydrodynamics of soft active matter'. *Reviews of Modern Physics* 85.3 (2013), p. 1143.

[2] T. Vicsek and A. Zafeiris. *Phys. Rep.* 517.3 (2012), pp. 71–140.

[3] S. Ramaswamy. 'The mechanics and statistics of active matter'. *Annu. Rev. Condens. Matter Phys.* 1.1 (2010), pp. 323–345.

[4] M. E. Cates and J. Tailleur. 'Motility-induced phase separation'. *Annu. Rev. Condens. Matter Phys.* 6.1 (2015), pp. 219–244.

[5] N. Kumar, H. Soni, S. Ramaswamy and A. Sood. 'Flocking at a distance in active granular matter'. *Nature communications* 5 (2014), p. 4688.

[6] N. D. Mermin and H. Wagner. 'Absence of ferromagnetism or antiferromagnetism in one-or two-dimensional isotropic Heisenberg models'. *Physical Review Letters* 17.22 (1966), p. 1133.

[7] N. D. Mermin. 'Crystalline order in two dimensions'. *Physical Review* 176.1 (1968), p. 250.

[8] P. C. Hohenberg. 'Existence of long-range order in one and two dimensions'. *Physical Review* 158.2 (1967), p. 383.

[9] J. Toner. 'Why walking is easier than pointing: Hydrodynamics of dry active matter'. *arXiv preprint arXiv:1812.00310* (2018).

[10] T. Vicsek, A. Czirók, E. Ben-Jacob, I. Cohen and O. Shochet. 'Novel type of phase transition in a system of self-driven particles'. *Physical review letters* 75.6 (1995), p. 1226.

[11] J. Toner, Y. Tu and S. Ramaswamy. 'Hydrodynamics and phases of flocks'. *Annals of Physics* 318.1 (2005), pp. 170–244.

[12] I. H. Riedel, K. Kruse and J. Howard. 'A self-organized vortex array of hydrodynamically entrained sperm cells'. *Science* 309.5732 (2005), pp. 300–303.

[13] H. H. Wensink, J. Dunkel, S. Heidenreich, K. Drescher, R. E. Goldstein, H. Löwen and J. M. Yeomans. 'Meso-scale turbulence in living fluids'. *Proceedings of the National Academy of Sciences* 109.36 (2012), pp. 14308–14313.

[14] P. Guillamat, J. Ignés-Mullol and F. Sagués. 'Taming active turbulence with patterned soft interfaces'. *Nature communications* 8.1 (2017), p. 564.

[15] J. Palacci, S. Sacanna, A. P. Steinberg, D. J. Pine and P. M. Chaikin. 'Living crystals of light-activated colloidal surfers'. *Science* 339.6122 (2013), pp. 936–940.

[16] Y. Sumino, K. H. Nagai, Y. Shitaka, D. Tanaka, K. Yoshikawa, H. Chaté and K. Oiwa. 'Large-scale vortex lattice emerging from collectively moving microtubules'. *Nature* 483.7390 (2012), p. 448.

[17] M. C. Marchetti, J.-F. Joanny, S. Ramaswamy, T. B. Liverpool, J. Prost, M. Rao and R. A. Simha. ‘Hydrodynamics of soft active matter’. *Reviews of Modern Physics* 85.3 (2013), p. 1143.

[18] C. Dombrowski, L. Cisneros, S. Chatkaew, R. E. Goldstein and J. O. Kessler. ‘Self-concentration and large-scale coherence in bacterial dynamics’. *Physical review letters* 93.9 (2004), p. 098103.

[19] A. Doostmohammadi, J. Ignés-Mullol, J. M. Yeomans and F. Sagués. ‘Active nematics’. *Nature communications* 9.1 (2018), p. 3246.

[20] A. Creppy, O. Praud, X. Druart, P. L. Kohnke and F. Plouraboué. ‘Turbulence of swarming sperm’. *Physical Review E* 92.3 (2015), p. 032722.

[21] O. Reynolds. ‘IV. On the dynamical theory of incompressible viscous fluids and the determination of the criterion’. *Philosophical transactions of the royal society of london.(a.)* 186 (1895), pp. 123–164.

[22] T. Pedley and J. Kessler. ‘Hydrodynamic phenomena in suspensions of swimming microorganisms’. *Annual Review of Fluid Mechanics* 24.1 (1992), pp. 313–358.

[23] J. Toner and Y. Tu. ‘Flocks, herds, and schools: A quantitative theory of flocking’. *Physical review E* 58.4 (1998), p. 4828.

[24] R. A. Simha and S. Ramaswamy. ‘Hydrodynamic fluctuations and instabilities in ordered suspensions of self-propelled particles’. *Physical review letters* 89.5 (2002), p. 058101.

[25] L. Chen, J. Toner and C. F. Lee. ‘Critical phenomenon of the order–disorder transition in incompressible active fluids’. *New Journal of Physics* 17.4 (2015), p. 042002.

[26] J. Dunkel, S. Heidenreich, M. Bär and R. E. Goldstein. ‘Minimal continuum theories of structure formation in dense active fluids’. *New J. Phys.* 15.4 (2013), p. 045016.

[27] E. M. Purcell. ‘Life at low Reynolds number’. *American journal of physics* 45.1 (1977), pp. 3–11.

[28] J. Elgeti, R. G. Winkler and G. Gompper. ‘Physics of microswimmers—single particle motion and collective behavior: a review’. *Reports on progress in physics* 78.5 (2015), p. 056601.

[29] H. C. Berg. ‘Bacterial behaviour’. *Nature* 254.5499 (1975), p. 389.

[30] H. C. Berg and D. A. Brown. ‘Chemotaxis in Escherichia coli analysed by three-dimensional tracking’. *Nature* 239.5374 (1972), p. 500.

[31] R. M. Harshey. ‘Bacterial motility on a surface: many ways to a common goal’. *Annual Reviews in Microbiology* 57.1 (2003), pp. 249–273.

[32] T. Sanchez, D. T. Chen, S. J. DeCamp, M. Heymann and Z. Dogic. ‘Spontaneous motion in hierarchically assembled active matter’. *Nature* 491.7424 (2012), p. 431.

[33] A. Bricard, J.-B. Caussin, N. Desreumaux, O. Dauchot and D. Bartolo. ‘Emergence of macroscopic directed motion in populations of motile colloids’. *Nature* 503.7474 (2013), p. 95.

[34] A. Ghosh and P. Fischer. ‘Controlled propulsion of artificial magnetic nanostructured propellers’. *Nano letters* 9.6 (2009), pp. 2243–2245.

[35] K. Drescher, J. Dunkel, L. H. Cisneros, S. Ganguly and R. E. Goldstein. ‘Fluid dynamics and noise in bacterial cell–cell and cell–surface scattering’. *Proceedings of the National Academy of Sciences* 108.27 (2011), pp. 10940–10945.

[36] T. Pedley. ‘Spherical squirmers: models for swimming micro-organisms’. *IMA Journal of Applied Mathematics* 81.3 (2016), pp. 488–521.

[37] G. Grégoire and H. Chaté. 'Onset of collective and cohesive motion'. *Physical review letters* 92.2 (2004), p. 025702.

[38] H. Chaté, F. Ginelli, G. Grégoire, F. Peruani and F. Raynaud. 'Modeling collective motion: variations on the Vicsek model'. *The European Physical Journal B* 64.3-4 (2008), pp. 451–456.

[39] S. Ramaswamy, R. A. Simha and J. Toner. 'Active nematics on a substrate: Giant number fluctuations and long-time tails'. *EPL (Europhysics Letters)* 62.2 (2003), p. 196.

[40] H. Chaté, F. Ginelli and R. Montagne. 'Simple model for active nematics: quasi-long-range order and giant fluctuations'. *Physical review letters* 96.18 (2006), p. 180602.

[41] K. H. Nagai, Y. Sumino, R. Montagne, I. S. Aranson and H. Chaté. 'Collective motion of self-propelled particles with memory'. *Physical review letters* 114.16 (2015), p. 168001.

[42] A. Choudhary, D. Venkataraman and S. S. Ray. 'Effect of inertia on model flocks in a turbulent environment'. *EPL (Europhysics Letters)* 112.2 (2015), p. 24005.

[43] R. E. Breier, C. C. Lalescu, D. Waas, M. Wilczek and M. G. Mazza. 'Emergence of phytoplankton patchiness at small scales in mild turbulence'. *Proceedings of the national academy of sciences* 115.48 (2018), pp. 12112–12117.

[44] G. S. Redner, M. F. Hagan and A. Baskaran. 'Structure and dynamics of a phase-separating active colloidal fluid'. *Physical review letters* 110.5 (2013), p. 055701.

[45] J. Toner and Y. Tu. 'Long-range order in a two-dimensional dynamical XY model: how birds fly together'. *Physical review letters* 75.23 (1995), p. 4326.

[46] X.-L. Wu and A. Libchaber. 'Particle diffusion in a quasi-two-dimensional bacterial bath'. *Physical review letters* 84.13 (2000), p. 3017.

[47] J. Dunkel, S. Heidenreich, K. Drescher, H. H. Wensink, M. Bär and R. E. Goldstein. *Phys. Rev. Lett.* 110.22 (2013), p. 228102.

[48] T. Sanchez, D. Chen, S. J DeCamp, M. Heymann and Z. Dogic. 'Spontaneous motion in hierarchically assembled active matter'. *Nature* 491.7424 (2012), p. 431.

[49] Y. Hatwalne, S. Ramaswamy, M. Rao and R. A. Simha. 'Rheology of active-particle suspensions'. *Physical review letters* 92.11 (2004), p. 118101.

[50] F. Ndlec, T. Surrey, A. C. Maggs and S. Leibler. 'Self-organization of microtubules and motors'. *Nature* 389.6648 (1997), p. 305.

[51] V. Schaller, C. Weber, C. Semmrich, E. Frey and A. R. Bausch. 'Polar patterns of driven filaments'. *Nature* 467.7311 (2010), p. 73.

[52] A. Creppy, F. Plouraboué, O. Praud, X. Druart, S. Cazin, H. Yu and P. Degond. 'Symmetry-breaking phase transitions in highly concentrated semen'. *Journal of The Royal Society Interface* 13.123 (2016), p. 20160575.

[53] R. Großmann, P. Romanczuk, M. Bär and L. Schimansky-Geier. 'Vortex arrays and mesoscale turbulence of self-propelled particles'. *Physical review letters* 113.25 (2014), p. 258104.

[54] L. Giomi. 'Geometry and topology of turbulence in active nematics'. *Phys. Rev. X* 5.3 (2015), p. 031003.

[55] L. Giomi, M. J. Bowick, P. Mishra, R. Sknepnek and M. C. Marchetti. 'Defect dynamics in active nematics'. *Phil. Trans. R. Soc. A* 372.2029 (2014), p. 20130365.

[56] A. Doostmohammadi, T. N. Shendruk, K. Thijssen and J. M. Yeomans. 'Onset of meso-scale turbulence in active nematics'. *Nat. Comm.* 8 (2017), p. 15326.

[57] A. Doostmohammadi, M. F. Adamer, S. Thampi and J. M. Yeomans. 'Stabilization of active matter by flow-vortex lattices and defect ordering'. *Nat. Commun.* 7 (2016).

[58] U. Frisch and A. N. Kolmogorov. *Turbulence: the legacy of AN Kolmogorov.* Cambridge university press, 1995.

[59] M. Lesieur. *Turbulence in fluids: stochastic and numerical modelling.* Nijhoff Boston, MA, 1987.

[60] A. S. Monin and A. M. Yaglom. *Statistical fluid mechanics, volume II: mechanics of turbulence.* Vol. 2. Courier Corporation, 2013.

[61] P. Davidson. *Turbulence: an introduction for scientists and engineers.* Oxford University Press, USA, 2015.

[62] L. Bentkamp, C. C. Lalescu and M. Wilczek. 'Persistent accelerations disentangle Lagrangian turbulence'. *Nature Commun.* 10 (2019), pp. 2041–1723.

[63] C. C. Lalescu and M. Wilczek. 'How tracer particles sample the complexity of turbulence'. *New Journal of Physics* 20.1 (2018), p. 013001.

[64] G. Boffetta and R. E. Ecke. 'Two-dimensional turbulence'. *Annual Review of Fluid Mechanics* 44 (2012), pp. 427–451.

[65] H. Xia, N. Francois, H. Punzmann and M. Shats. 'Lagrangian scale of particle dispersion in turbulence'. *Nature communications* 4 (2013).

[66] J. M. Kosterlitz and D. J. Thouless. 'Ordering, metastability and phase transitions in two-dimensional systems'. *Journal of Physics C: Solid State Physics* 6.7 (1973), p. 1181.

[67] M. Lesieur. *Turbulence in fluids.* Kluwer Dordrecht, 1990.

[68] T Tatsumi. 'The theory of decay process of incompressible isotropic turbulence'. *Proceedings of the Royal Society of London. Series A. Mathematical and Physical Sciences* 239.1216 (1957), pp. 16–45.

[69] Y. Ogura. 'Energy transfer in a normally distributed and isotropic turbulent velocity field in two dimensions'. *The Physics of Fluids* 5.4 (1962), pp. 395–401.

[70] Y. Ogura. 'A consequence of the zero-fourth-cumulant approximation in the decay of isotropic turbulence'. *J. Fluid. Mech.* 16 (1963), pp. 33–40.

[71] I. Proudman and W. Reid. 'On the Decay of a Normally Distributed and Homogeneous Turbulent Velocity Field'. *Phil. Trans. R. Soc. Lond. A* 247 (1954), pp. 163–189.

[72] C. Leith. 'Atmospheric predictability and two-dimensional turbulence'. *J. Atmospheric Sci.* 28.2 (1971), pp. 145–161.

[73] W. D. McComb. 'The physics of fluid turbulence'. *Chemical physics* (1990).

[74] G. K. Batchelor. *The theory of homogeneous turbulence.* Cambridge university press, 1953.

[75] M. Millionschikov. 'On theory of homogeneous isotropic turbulence'. *Dokl. Akad. Nauk SSSR* 32 (1941), p. 615.

[76] S. Orszag. 'Analytical theories of turbulence'. *J. Fluid Mech.* 41.2 (1970), pp. 363–386.

[77] S. Orszag. *Lectures on the statistical theory of turbulence.* Flow Research Inc., 1974.

[78] K. J. Strandburg. ‘Two-dimensional melting’. *Reviews of modern physics* 60.1 (1988), p. 161.

[79] R. Peierls. ‘On Ising’s model of ferromagnetism’. In: *Mathematical Proceedings of the Cambridge Philosophical Society.* Vol. 32. 3. Cambridge University Press. 1936, pp. 477–481.

[80] P. Dillmann, G. Maret and P. Keim. ‘Comparison of 2D melting criteria in a colloidal system’. *Journal of Physics: Condensed Matter* 24.46 (2012), p. 464118.

[81] D. R. Nelson and B. Halperin. ‘Dislocation-mediated melting in two dimensions’. *Physical Review B* 19.5 (1979), p. 2457.

[82] F. A. Lindemann. ‘The calculation of molecular Eigen-frequencies’ (1984).

[83] K. Zahn, R Lenke and G. Maret. ‘Two-stage melting of paramagnetic colloidal crystals in two dimensions’. *Physical review letters* 82.13 (1999), p. 2721.

[84] K. Zahn and G. Maret. ‘Dynamic criteria for melting in two dimensions’. *Phys. Rev. Lett.* 85.17 (2000), p. 3656.

[85] B. Halperin and D. R. Nelson. ‘Theory of two-dimensional melting’. *Phys. Rev. Lett.* 41.2 (1978), p. 121.

[86] A. Young. ‘Melting and the vector Coulomb gas in two dimensions’. *Physical Review B* 19.4 (1979), p. 1855.

[87] T. Ramakrishnan and M. Yussouff. ‘First-principles order-parameter theory of freezing’. *Phys. Rev. B* 19.5 (1979), p. 2775.

[88] S. Chui. ‘Grain-boundary theory of melting in two dimensions’. *Phys. Rev. B* 28.1 (1983), p. 178.

[89] F. Boyer and E. Falcon. ‘Two-Dimensional Melting of a Crystal of Ferrofluid Spikes’. *Phys. Rev. Lett.* 103.14 (2009), p. 144501.

[90] D. I. Goldman, M. Shattuck, S. J. Moon, J. Swift and H. L. Swinney. ‘Lattice dynamics and melting of a nonequilibrium pattern’. *Phys. Rev. Lett.* 90.10 (2003), p. 104302.

[91] P. Perlekar and R. Pandit. ‘Turbulence-induced melting of a nonequilibrium vortex crystal in a forced thin fluid film’. *New J. Phys.* 12.2 (2010), p. 023033.

[92] I Theurkauff, C Cottin-Bizonne, J Palacci, C Ybert and L Bocquet. ‘Dynamic clustering in active colloidal suspensions with chemical signaling’. *Physical review letters* 108.26 (2012), p. 268303.

[93] A. P. Petroff, X.-L. Wu and A. Libchaber. ‘Fast-moving bacteria self-organize into active two-dimensional crystals of rotating cells’. *Physical review letters* 114.15 (2015), p. 158102.

[94] J. U. Klamser, S. C. Kapfer and W. Krauth. ‘Thermodynamic phases in two-dimensional active matter’. *Nat. Comm.* 9.1 (2018), p. 5045.

[95] A. M. Menzel and H. Löwen. ‘Traveling and resting crystals in active systems’. *Phys. Rev. Lett.* 110.5 (2013), p. 055702.

[96] A. M. Menzel, T. Ohta and H. Löwen. ‘Active crystals and their stability’. *Phys. Rev. E* 89.2 (2014), p. 022301.

[97] S. Heidenreich, J. Dunkel, S. H. Klapp and M. Bär. ‘Hydrodynamic length-scale selection in microswimmer suspensions’. *Phys. Rev. E* 94.2 (2016), p. 020601.

[98] H. Reinken, S. H. Klapp, M. Bär and S. Heidenreich. ‘Derivation of a hydrodynamic theory for mesoscale dynamics in microswimmer suspensions’. *Phys. Rev. E* 97.2 (2018), p. 022613.

[99] J. Yeomans. *Soft Matter Self-Assembly* 193 (2016), p. 383.

[100] A. M. Menzel. *Phys. Rep.* 554 (2015), pp. 1–45.

[101] R. Soto and R. Golestanian. *Phys. Rev. E* 91.5 (2015), p. 052304.

[102] A. Czirók, H. E. Stanley and T. Vicsek. *J. Phys. A: Mathematical and General* 30.5 (1997), p. 1375.

[103] R. Chatterjee, A. A. Joshi and P. Perlekar. *Phys. Rev. E* 94.2 (2016), p. 022406.

[104] H. Wensink and H. Löwen. *J. Phys. Condens. Matter* 24.46 (2012), p. 464130.

[105] V. Bratanov, F. Jenko and E. Frey. 'New class of turbulence in active fluids'. *Proc. Natl. Acad. Sci. U.S.A.* 112.49 (2015), pp. 15048–15053.

[106] R. H. Kraichnan and D. Montgomery. 'Two-dimensional turbulence'. *Rep. Prog. Phys.* 43.5 (1980), p. 547.

[107] G. Boffetta, A. Celani and M. Vergassola. *Phys. Rev. E* 61.1 (2000), R29.

[108] Y. Huang, W. Ou, M. Chen, Z. Lu, N. Jiang et al. *Phys. Fluids* 29.5 (2017), p. 051901.

[109] S. P. Thampi and J. M. Yeomans. *Eur. Phys. J. Special Topics* 225.4 (2016), pp. 651–662.

[110] S. P. Thampi, R. Golestanian and J. M. Yeomans. *EPL* 105.1 (2014), p. 18001.

[111] J. Urzay, A. Doostmohammadi and J. M. Yeomans. *J. Fluid Mech.* 822 (2017), pp. 762–773.

[112] J. Elgeti, M. E. Cates and D. Marenduzzo. *Soft Matter* 7.7 (2011), pp. 3177–3185.

[113] F. Zanger, H. Löwen and J. Saal. 'Analysis of a Living Fluid Continuum Model'. In: *Mathematics for Nonlinear Phenomena: Analysis and Computation.* Springer. 2017, pp. 285–303.

[114] M. Wilczek, A. Daitche and R. Friedrich. *J. Fluid Mech.* 676 (2011), pp. 191–217.

[115] M. Wilczek and R. Friedrich. *Phys. Rev. E* 80.1 (2009), p. 016316.

[116] T. Leung, N. Swaminathan and P. A. Davidson. *J. Fluid Mech.* 710 (2012), pp. 453–481.

[117] G. E. Elsinga and I. Marusic. *J. Fluid Mech.* 662 (2010), pp. 514–539.

[118] M. Wilczek, O. Kamps and R. Friedrich. *Physica D* 237.14 (2008), pp. 2090–2094.

[119] O. Kamps and R. Friedrich. *Phys. Rev. E* 78.3 (2008), p. 036321.

[120] J. M. Yeomans. 'Active matter: Playful topology'. *Nat. Mater.* 13.11 (2014), p. 1004.

[121] N. Mendelson, A. Bourque, K. Wilkening, K. Anderson and J. Watkins. 'Organized cell swimming motions in Bacillus subtilis colonies: patterns of short-lived whirls and jets'. *J. Bacteriol.* 181.2 (1999), pp. 600–609.

[122] T. Ishikawa and T. J. Pedley. 'Coherent Structures in Monolayers of Swimming Particles'. *Phys. Rev. Lett.* 100 (8 2008), p. 088103.

[123] J. R. Howse, R. A. L. Jones, A. J. Ryan, T. Gough, R. Vafabakhsh and R. Golestanian. 'Self-Motile Colloidal Particles: From Directed Propulsion to Random Walk'. *Phys. Rev. Lett.* 99 (4 2007), p. 048102.

[124] A. Bricard, J.-B. Caussin, N. Desreumaux, O. Dauchot and D. Bartolo. 'Emergence of macroscopic directed motion in populations of motile colloids.' *Nature* 503.7474 (2013), pp. 95–98.

[125] C. Wolgemuth. 'Collective swimming and the dynamics of bacterial turbulence'. *Biophys. J.* 95.4 (2008), pp. 1564–1574.

[126] M. Genkin, A. Sokolov, O. Lavrentovich and I. Aranson. 'Topological Defects in a Living Nematic Ensnare Swimming Bacteria'. *Phys. Rev. X* 7 (1 2017), p. 011029.

[127] K. Suzuki, M. Miyazaki, J. Takagi, T. Itabashi and S. Ishiwata. 'Spatial confinement of active microtubule networks induces large-scale rotational cytoplasmic flow'. *Proc. Natl. Acad. Sci. U.S.A.* 114.11 (2017), pp. 2922–2927.

[128] H. Wioland, F. G. Woodhouse, J. Dunkel and R. E. Goldstein. 'Ferromagnetic and antiferromagnetic order in bacterial vortex lattices'. *Nat. Phys.* 12.4 (2016), p. 341.

[129] R. Großmann, P. Romanczuk, M. Bär and L. Schimansky-Geier. 'Pattern formation in active particle systems due to competing alignment interactions'. *Eur. Phys. J. S. T.* 224.7 (2015), pp. 1325–1347.

[130] C. Bechinger, R. Di Leonardo, H. Löwen, C. Reichhardt, G. Volpe and G. Volpe. 'Active particles in complex and crowded environments'. *Rev. Mod. Phys.* 88 (4 2016), p. 045006.

[131] A. U. Oza and J. Dunkel. 'Antipolar ordering of topological defects in active liquid crystals'. *New J. Phys.* 18.9 (2016), p. 093006.

[132] H. H. Wensink, J. Dunkel, S. Heidenreich, K. Drescher, R. E. Goldstein, H. Löwen and J. M. Yeomans. 'Meso-scale turbulence in living fluids'. *Proc. Natl. Acad. Sci. U.S.A.* 109.36 (2012), pp. 14308–14313.

[133] V. Bratanov, F. Jenko and E. Frey. 'New class of turbulence in active fluids'. *Proc. Natl. Acad. Sci. U.S.A.* 112.49 (2015), pp. 15048–15053.

[134] M. Cross and H. Greenside. *Pattern formation and dynamics in nonequilibrium systems.* Cambridge University Press, 2009.

[135] M. James and M. Wilczek. 'Vortex dynamics and Lagrangian statistics in a model for active turbulence'. *Eur. Phys. J. E* 41.2 (2018), p. 21.

[136] G. Batchelor. *The theory of homogeneous turbulence.* Cambridge university press, 1953.

[137] A. Monin and A. Yaglom. *Statistical fluid mechanics, volume II: Mechanics of turbulence.* Vol. 2. Dover Publications, 2013.

[138] S. Pope. *Turbulent Flows.* 2000.

[139] M. Lesieur. *Turbulence in fluids.* 4th ed. Springer Science, 2008.

[140] P. Sagaut and C. Cambon. *Homogeneous Turbulence Dynamics.* Cambridge University Press, 2008.

[141] J. Słomka and J. Dunkel. 'Geometry-dependent viscosity reduction in sheared active fluids'. *Phys. Rev. Fluids* 2.4 (2017), p. 043102.

[142] N. Kukharkin, S. A. Orszag and V. Yakhot. 'Quasicrystallization of Vortices in Drift-Wave Turbulence'. *Phys. Rev. Lett.* 75 (13 1995), pp. 2486–2489.

[143] J. Jiménez and A. Guegan. 'Spontaneous generation of vortex crystals from forced two-dimensional homogeneous turbulence'. *Phys. Fluids* 19.8 (2007), p. 085103.

[144] L. Smith and V. Yakhot. 'Finite-size effects in forced two-dimensional turbulence'. *J. Fluid Mech.* 274 (1994), pp. 115–138.

[145] B. Arbic and G. Flierl. 'Effects of mean flow direction on energy, isotropy, and coherence of baroclinically unstable beta-plane geostrophic turbulence'. *J. Phys. Oceanogr.* 34.1 (2004), pp. 77–93.

[146] A. Gupta and R. Pandit. 'Melting of a nonequilibrium vortex crystal in a fluid film with polymers: Elastic versus fluid turbulence'. *Phys. Rev. E* 95.3 (2017), p. 033119.

[147] A. Abrikosov. 'The magnetic properties of superconducting alloys'. *J. Phys. Chem. Solids* 2.3 (1957), pp. 199–208.

[148] U. Essmann and H. Träuble. 'The direct observation of individual flux lines in type II superconductors'. *Phys. Lett. A* 24.10 (1967), pp. 526–527.

[149] J. Dunkel, S. Heidenreich, M. Bär and R. E. Goldstein. 'Minimal continuum theories of structure formation in dense active fluids'. *New J. Phys.* 15.4 (2013), p. 045016.

[150] A. U. Oza, S. Heidenreich and J. Dunkel. 'Generalized Swift-Hohenberg models for dense active suspensions'. *Eur. Phys. J. E* 39.10 (2016), p. 97.

[151] R. Kraichnan. 'The structure of isotropic turbulence at very high Reynolds numbers'. *J. Fluid Mech.* 5 (1959), pp. 497–543.

[152] R. Kraichnan. 'Lagrangian-History Closure Approximation for Turbulence'. *Phys. Fluids* 8 (1965), pp. 575–598.

[153] W. J. T. Bos and J.-P. Bertoglio. 'Lagrangian Markovianized Field Approximation for turbulence'. *J. Turbul.* 14 (2013), p. 99.

[154] I Guillamón, H Suderow, A Fernández-Pacheco, J Sesé, R Córdoba, J. De Teresa, M. Ibarra and S Vieira. 'Direct observation of melting in a two-dimensional superconducting vortex lattice'. *Nat. Phys.* 5.9 (2009), p. 651.

[155] S. C. Kapfer and W. Krauth. 'Two-dimensional melting: From liquid-hexatic coexistence to continuous transitions'. *Phys. Rev. Lett.* 114.3 (2015), p. 035702.

[156] S. C. Takatori, R. De Dier, J. Vermant and J. F. Brady. 'Acoustic trapping of active matter'. *Nat. Commun.* 7 (2016), p. 10694.

[157] D. Volfson, S. Cookson, J. Hasty and L. S. Tsimring. 'Biomechanical ordering of dense cell populations'. *Proc. Natl. Acad. Sci. U.S.A.* 105.40 (2008), pp. 15346–15351.

[158] R. Singh and R Adhikari. 'Universal hydrodynamic mechanisms for crystallization in active colloidal suspensions'. *Phys. Rev. Lett.* 117.22 (2016), p. 228002.

[159] B. C. van Zuiden, J. Paulose, W. T. Irvine, D. Bartolo and V. Vitelli. 'Spatiotemporal order and emergent edge currents in active spinner materials'. *Proc. Natl. Acad. Sci. U.S.A.* 113.46 (2016), pp. 12919–12924.

[160] N. H. Nguyen, D. Klotsa, M. Engel and S. C. Glotzer. 'Emergent collective phenomena in a mixture of hard shapes through active rotation'. *Phys. Rev. Lett.* 112.7 (2014), p. 075701.

[161] S. Paliwal and M. Dijkstra. 'The role of topological defects in the two-stage melting and elastic behavior of active Brownian particles'. *arXiv preprint arXiv:1907.04767* (2019).

[162] C. A. Weber, C. Bock and E. Frey. 'Defect-mediated phase transitions in active soft matter'. *Phys. Rev. Lett.* 112.16 (2014), p. 168301.

[163] B. M. Mognetti, A Šarić, S. Angioletti-Uberti, A Cacciuto, C Valeriani and D. Frenkel. 'Living clusters and crystals from low-density suspensions of active colloids'. *Phys. Rev. Lett.* 111.24 (2013), p. 245702.

[164] S. Praetorius, A. Voigt, R. Wittkowski and H. Löwen. 'Active crystals on a sphere'. *Phys. Rev. E* 97.5 (2018), p. 052615.

[165] M. James, W. J. Bos and M. Wilczek. 'Turbulence and turbulent pattern formation in a minimal model for active fluids'. *Phys. Rev. Fluids* 3.6 (2018), p. 061101.

[166] V. Bedanov, G. Gadiyak and Y. E. Lozovik. ‘On a modified Lindemann-like criterion for 2D melting’. *Physics Letters A* 109.6 (1985), pp. 289–291.

[167] K. Kaneko. ‘Supertransients, spatiotemporal intermittency and stability of fully developed spatiotemporal chaos’. *Phys. Lett. A* 149.2-3 (1990), pp. 105–112.

[168] J. P. Crutchfield and K. Kaneko. ‘Are attractors relevant to turbulence?’ *Phys. Rev. Lett.* 60.26 (1988), p. 2715.

[169] M. C. Strain and H. S. Greenside. ‘Size-dependent transition to high-dimensional chaotic dynamics in a two-dimensional excitable medium’. *Phys. Rev. Lett.* 80.11 (1998), p. 2306.

[170] Y.-C. Lai and T. Tél. *Transient chaos: complex dynamics on finite time scales.* Vol. 173. Springer Science & Business Media, 2011.

[171] M. Linkmann, G. Boffetta, M. C. Marchetti and B. Eckhardt. ‘Phase Transition to Large Scale Coherent Structures in Two-Dimensional Active Matter Turbulence’. *Phys. Rev. Lett.* 122 (21 2019), p. 214503.

[172] P. K. Newton. *The N-vortex problem: analytical techniques.* Vol. 145. Springer Science & Business Media, 2013.

[173] V. Tkachenko. ‘On vortex lattices’. *Sov. Phys. JETP* 22.6 (1966), pp. 1282–1286.

[174] N. Kukharkin, S. A. Orszag and V. Yakhot. ‘Quasicrystallization of vortices in drift-wave turbulence’. *Phys. Rev. Lett.* 75.13 (1995), p. 2486.

[175] S. M. H. Alavi and J. Cosson. ‘Sperm motility in fishes. I. Effects of temperature and pH: a review’. *Cell Biol. Int.* 29.2 (2005), pp. 101–110.

[176] D. Woolley. ‘Motility of spermatozoa at surfaces’. *Reproduction* 126.2 (2003), pp. 259–270.

[177] D. Nishiguchi, I. S. Aranson, A. Snezhko and A. Sokolov. ‘Engineering bacterial vortex lattice via direct laser lithography’. *Nat. Comm.* 9.1 (2018), p. 4486.

[178] S. A. Orszag. ‘Numerical methods for the simulation of turbulence’. *The Physics of Fluids* 12.12 (1969), pp. II–250.

[179] J. C. Butcher. *The numerical analysis of ordinary differential equations: Runge-Kutta and general linear methods.* Wiley-Interscience, 1987.

[180] J. Swift and P. C. Hohenberg. ‘Hydrodynamic fluctuations at the convective instability’. *Physical Review A* 15.1 (1977), p. 319.

[181] A. Thess. ‘Instabilities in two-dimensional spatially periodic flows. Part II: Square eddy lattice’. *Physics of Fluids A: Fluid Dynamics* 4.7 (1992), pp. 1396–1407.